PULSED ELECTRICAL DISCHARGE IN GAS BUBBLES IN WATER

By

SOPHIA GERSHMAN

A Dissertation submitted to the

Graduate School-New Brunswick

Rutgers, The State University of New Jersey

in partial fulfillment of the requirements

for the degree of

Doctor of Philosophy

Graduate Program in Physics and Astronomy

written under the direction of

Professor Theodore Madey

co-advisor Associate Provost Kurt Becker

and approved by

_____

_____

_____

_____

_____

New Brunswick, New Jersey

October, 2008

ABSTRACT OF THE DISSERTATION

PULSED ELECTRICAL DISCHARGE IN GAS BUBBLES IN WATER

By SOPHIA GERSHMAN

Dissertation Directors:

Professor Theodore Madey and Associate Provost Kurt Becker

A phenomenological picture of pulsed electrical discharge in gas bubbles in water is produced by combining electrical, spectroscopic, and imaging methods. The discharge is generated by applying one microsecond long 5 to 20 kilovolt pulses between the needle and disk electrodes submerged in water. A gas bubble is generated at the tip of the needle electrode. The study includes detailed experimental investigation of the discharge in argon bubbles and a brief look at the discharge in oxygen bubbles. Imaging, electrical characteristics, and time-resolved optical emission data point to a fast streamer propagation mechanism and formation of a plasma channel in the bubble. Spectroscopic methods based on line intensity ratios and Boltzmann plots of line intensities of argon, atomic hydrogen, and argon ions and the examination of molecular emission bands from molecular nitrogen and hydroxyl radicals provide evidence of both fast beam-like electrons and slow thermalized ones with temperatures of 0.6 – 0.8 electron-volts. The collisional nature of plasma at atmospheric pressure affects the decay rates of optical emission. Spectroscopic study of rotational-vibrational bands of hydroxyl radical and molecular nitrogen gives vibrational and rotational excitation temperatures of the discharge of about 0.9 and 0.1 electron-volt, respectively. Imaging and electrical

evidence show that discharge charge is deposited on the bubble wall and water serves as a dielectric barrier for the field strength and time scales of this experiment. Comparing the electrical and imaging information for consecutive pulses applied at a frequency of 1 Hz indicates that each discharge proceeds as an entirely new process with no memory of the previous discharge aside from long-lived chemical species, such as ozone and oxygen. Intermediate values for the discharge gap and pulse duration, low repetition rate, and unidirectional character of the applied voltage pulses make the discharge process here unique compared to the traditional corona or dielectric barrier discharges. These conditions make the experimental evidence presented in this work valuable for the advancement of modeling and the theoretical understanding of the discharge in bubbles in water.

Acknowledgements

This work has been conducted in collaboration with Stevens Institute of Technology. The project has been supported in part by the US Army TACOM/ARDEC (Picatinny Arsenal).

Invaluable assistance and support have been provided by Professor Madey and Associate Provost Dr. Becker. The infinite patience and continued support of the entire committee is gratefully acknowledged. Deep gratitude goes to Professors T. Madey, K. Becker, N. Koller, P. Coleman, R. Ransome, T. Gustafsson.

Special thanks go to the Director of Vossen Laboratory, Dr. A. Belkind for his limitless energy, unfaltering optimism, and his dedication to his students and the laboratory.

Table of contents

List of tables

List of Illustrations

1. General Introduction

Electrical discharges and plasmas span phenomena from welding arcs and stars to lightning and lighting fixtures. Artificially generated electrical discharges have a long history of use for the modification of bulk and surface properties of materials, chemical synthesis, machining, and waste treatment. Electrical discharges occur due to the dielectric breakdown of a material under the influence of outside electromagnetic fields. For example, lightning occurs due to ionization of air under the intense electric fields between clouds or between clouds and ground. All applications of electrical discharges are based on the fact that ionization processes in gases produce some concentration of free electrons, ions, free radicals, and excited atoms and molecules, all capable of engaging in chemical and physical interactions. Specific applications depend on the types, concentrations, and the energy of the active species in the discharge, and on the global properties such as power input and output, electrical current, and the pressure and temperature of the operating gas. The motivation for this work comes from using electrical discharge in gases at atmospheric pressure for the treatment of contaminated water.

Electrical discharges are particularly suitable to water treatments that require decomposition or degradation of molecular contaminants, processes that can be useful for both decontamination and sterilization. The benefit of using electrical discharges comes from in-situ production of all the active materials. The disadvantage comes from costly high power requirements, particularly if the discharge is attempted directly in the liquid state.[1-8] To reduce the power consumption and further expand the variety of active

species generated in the discharge, gas bubbles may be introduced externally into the treated water. Then the external field can be reduced and the discharge can be limited to gas bubbles. In that case, the discharge takes place in a humid gas at atmospheric pressure, or somewhat higher, inside the bubbles. The usual choice of gas is air, oxygen, inert gases, or some combination of the three varieties.

Various reactor designs use different electrode and bubble configurations. Electrodes may be mesh, wires, wire-to-plane, or needle-to-plane, and the bubbles may pass between the electrodes, making no contact with either or spending a long time attached to one or both electrodes. The discharge mechanisms and the demands on the outside circuit design depend on the electrode arrangement. In general, different contaminants require different properties of a discharge and different treatment protocols.

To date, discharges in bubbles in water have been investigated for their effectiveness in water treatment, including estimates of power consumption and the production of active species. B. Sun *et al* (1999) and M. Kurahashi (1997) studied radical production.[11, 12] Miichi *et al* (2000, 2002) investigated the production of OH radical by pulsed discharges in bubbles in water.[13, 14] The OH radical production was confirmed by emission spectroscopy. The concentration of dissolved ozone was also measured when oxygen was used as the bubbled gas. Miichi *et al* also observed discoloration of indigo solution. Yamabe *et al* (2005) of the same research group also reported using a discharge that propagates along the surface of a bubble in water for a similar de-coloration experiment with a new electrode-bubble configuration using a mixture of oxygen and helium in the bubbles.[15] Applied voltages in all studies by these groups are in the 20 – 25 kV range and a pulse rate of 100 Hz. Anpilov et al (2001, 2002) reported successful

production of UV radiation, ozone, and hydrogen peroxide in multi-electrode systems with gas bubbles supplied into the space between the electrodes.[16, 17] The focus of these and other studies (ex. Akishev, 2008) has been the generation of biologically-active species for sterilization purposes.[18] Mozgina *et al* investigated the effectiveness of the discharge in gas bubbles for degradation of explosive contaminants[1] and also for de-coloration.[19, 20] This study also included measurements of hydrogen peroxide and ozone generation (for oxygen gas) and spectroscopic determination of the presence of other radicals, such as H and O. Mozgina reported observation of two distinct types of discharge in her system that can be identified from the current and voltage oscillograms. Spark type discharge was reported to be more effective for decontamination purposes. The discharge was observed to propagate along the wall of large bubbles while the bubbles remain stationary between parallel mesh electrodes. [19, 20] Various reactor designs and electrode-bubble geometries was also studied by Mozgina and assessed for their effectiveness. The studies to date have reported on radical production, reactor design, treatment effectiveness, and measured electrical characteristics of the systems. Spectroscopic studies have focused on radical production. [19, 20, 21]

Other types of plasmas and discharges have been thoroughly characterized, their specific application or effect correlated to spatially and temporally resolved plasma parameters. During pulsed plasma thin film deposition for example, electron energy and number density are investigated in detail using Langmuir probes and emission spectroscopy.[22, 23] Dielectric Barrier Discharges, filamentary in most situations, do not allow for the use of probes, so in this field several spectroscopic techniques are usually

[1] three high explosive compounds: 2,4,6-trinitrotoluene (TNT), hexahydro-1,3,5-trinitro-1,3,5-triazine (RDX), and octahydro-1,3,5,7-tetranitro-1,3,5,7-tetrazocine (HMX)

combined for experimental determination of discharge characteristics. Modeling is used then to produce theoretical spectra and compare those to the experimental results. For example, extensive work has been done by H-E. Wagner and K. Kozolov *et al* (2001, 2005) and other groups to compare modeling and experimental results in air and N_2/O_2 mixtures both spatially and temporally. [24, 25]

There is a clear lack of detailed study of the discharge parameters for a discharge in bubbles in water. Experimental values of discharge and plasma parameters are essential for advancing of the theoretical understanding of the processes in the bubbles. Successful simulations can aid in controlling the discharge parameters for practical applications. To approach the problem of optimization of treatment conditions for highest effectiveness with any degree of intelligent deliberation, detailed information is needed on the properties of the discharge process used for treatment.

The goal of this work is to describe the processes that occur in a gas bubble submerged in water during a pulsed electrical discharge in terms of plasma parameters.

1.1 Organization of this work

This work is organized into six chapters. The next Chapter 2, Introduction, presents some of the basic concepts and the latest developments in the area of electrical discharges at atmospheric pressure. The purpose of the discussion is to introduce the terminology used in this field and delineate some of the open questions remaining at the present time. Chapter 3 describes the experimental set-up and equipment used in this investigation. The complexity of the experimental tasks has demanded some unique approaches that are outlined in this chapter. Chapter 4 presents the methodology, results, and analysis of the data on electrical discharge in Ar bubbles. The chapter is subdivided into sections corresponding to the experimental method described in each sub-section. The results of the electrical, optical, and spectroscopic investigations, and a study using a photomultiplier tube, are discussed in each sub-section. Chapter 5 presents results in a similar way but for an oxygen bubble. The last chapter (Chapter 6) discusses the overall view of the discharge processes in Ar and oxygen bubbles obtained from the combined results of all the experimental methods discussed here. A list of the most important results and findings is given at the end of this work.

References:

1. M. Sato, T. Ohgiyama, and .S. Clements, (1996) *IEEE Trans. Ind. Appl*. **32**(1), pp. 106.
2. B. Sun, M. Sato, J.S. Clements, (1997) J. Electrostatics, **39** (3), pp. 189.
3. S. Ihara, M. Miichi, S. Satoh, and C. Yamabe, (1999) IEEE Intl Pulsed Power Conf. 5451, pp. 1291.
4. H. Akiyama, (2000) IEEE Trans. Diel. Electr. Insul., **7**, pp. 646.
5. A. M. Anpilov, E. M. Barkhudarov, Yu. B. Bark, (2001) *J. Phys. D: Appl. Phys.*, **34**, pp. 993–999
6. A. Abou-Ghazala, S. Katsuki, K. H. Schoenbach, F.C. Dobbs, and K.R. Moreira, (2002) *IEEE Trans. Plasma Sci.,* **30**, pp. 1449.
7. P. Lukes, A.T. Appleton, B. Locke, (2004) *IEEE Trans. Ind. Appl.*, **40** (1), pp. 60-67
8. P. Lukes, B. Locke, (2005) *Ind. Eng. Chem. Res.*, **44**, pp. 2921-2930
9. P. Sunka, V. Babicky, M. Clupek, P. Lukes, M. Simek, J. Schmidt, M. Cernak, (1999) *Plasma Sources Sci.Technol.*, **8**, pp. 258-265
10. Y. Wen, H. Liu, W. Liu, X. Jiang, (2005), *Plasma Chem, Process.*, **5**, pp. 137–146
11. B. Sun, M. Sato, J. Clemens, (1999) *J. Phys. D: Appl. Phys*., **32**, pp. 1908–1915T.
12. M. Kurahashi, S. Katsura, A. Mizuno, (1997), *Journal of Electrostatics*, **42**, No. 1, pp. 93-105
13. T. Miichi, S. Ihara, S. Satoh, C. Yamabe, (2000) *Vacuum*, **59**, pp. 236-243
14. T. Miichi, N. Hayashi, S. Ihara, S. Satoh and C. Yamabe, *Ozone : science & engineering*, (2002), **24**, No. 6, pp. 471-477
15. C. Yamabe, F. Takeshita, T. Miichi, N. Hayashi, S. Ihara, (2005) *Plasma, Process. Polym*, **2**, pp. 246-251
16. A. Anpilov *et al* (2001) *J. Phys. D: Appl. Phys.* **34** 993-999
17. A.M. Anpilov , E.M. Barkhudarov , N. Christofi , V.A. Kop'ev , I.A. Kossyi , M.I. Taktakishvili and Y. Zadiraka, *Letters in Applied Microbiology*, **35,** Issue 1, (2002), pp. 90 – 94
18. Akishev, Y.; Grushin, M.; Karalnik, V.; Monich, A.; Petryakov, A.; Trushkin, N., (2008), Plasma Science, IEEE Transactions on, **36**, Issue 4, pp. 1142 – 1143
19. Mozgina, O.; Gershman, S.; Belkind, A.; Becker, K.; Christodoulatos, C. Plasma Science, 2006. ICOPS 2006. IEEE Conference Record - Abstracts. The 33rd IEEE International Conference on, (2006), pp. 217 – 217
20. O. Mozgina,, Pulsed Electrical Discharges in Bubbled Water for Environmental Applications, Ph.D. Thesis (2008) Stevens Institute of Technology.
21. S. Gershman, O. Mozgina, A. Belkind, K. Becker, E. Kunhardt, Contributions to Plasma Physics, **47**, Issue 1-2 , (2007), pp.19 - 25
22. Y. Kim, M. Junga, S. Oh, J. Han, (2005), Thin Solid Films, 475, 91– 96
23. Th. Welzel, Th. Dunger, St. Welzel, H. Kupfer, F. Richter, (2005), Surface & Coatings Technology, pp. 1-4
24. K. Kozlov, H-E Wagner, R. Brandenburg, P. Michel, J. (2001), Phys. D: Appl. Phys., **34**, 3164-3176
25. K. Kozlov, R. Brandenburg, H-E Wagner, A. Morozov, P. Michel, J. (2005), Phys. D: Appl. Phys., **38**, 518-529

2. Background

Electrical discharges occur when an insulating medium becomes partially or completely ionized subject to an electromagnetic field. Discharges produce plasmas in some regions in the discharge or at some time during the process.

2.1. Plasma definition and characteristics

Definition of Plasma:

Plasmas are quasi-neutral systems of free electrons and ions that exhibit collective behavior. Collective behavior manifests itself in the reaction of a plasma to deviations from neutrality and applied external electromagnetic fields, and in its ability to sustain many different forms of waves and oscillations.[1, 2, 3]

Plasma Density:

Plasmas are produced by an ionization process that creates a certain number of free electrons and a number of positive ions. Provided quasi-neutrality holds, the number density of electrons n_e is approximately equal to the ion density n_i, $n_e \approx n_i$ and n_e is called the plasma density.

The usual units for plasma density are cm^{-3}. Atmospheric pressure plasmas can vary in density from 10^9 to 10^{19} cm^{-3}, corresponding to the degree of ionization from 10^{-10} to 1. [3]

Electron Energy Distribution Function:

Electron motion and energy are influenced by the applied electromagnetic fields and by their interactions (both long-range and short) with the heavy particles in the plasma. The energy individual electrons gain from the applied fields gets redistributed to other electrons and heavy particles by collisions. If energy reaches thermal equilibrium at least within the population of electrons, then the electron energy distribution can be described by Maxwell-Boltzmann distribution function:[1, 3]

$$f(\mathcal{E}) = \frac{2}{k_B \cdot T_e} \cdot \left(\frac{\mathcal{E}}{\pi \cdot k_B \cdot T_e} \right)^{\frac{1}{2}} \cdot \exp\left(-\frac{\mathcal{E}}{k_B \cdot T_e} \right) \tag{2.1.}$$

where $\mathcal{E}$ is the electron energy, k_B is the Boltzmann constant, and the electron temperature T_e is understood in its usual way through the mean electron energy

$$\langle \mathcal{E} \rangle = \int_0^\infty \mathcal{E} \cdot f(\mathcal{E}) \, \mathrm{d}\mathcal{E} \tag{2.2}$$

as

$$\langle \mathcal{E} \rangle = \frac{3}{2} \cdot k_B \cdot T_e \tag{2.3}$$

Since T_e is the mean electron energy (given by Maxwell distribution), it is convenient to express it in energy units directly (usually in eV) and replace

$$k_B \cdot T_e \rightarrow T_e \tag{2.4}$$

In this work, for all practical estimates, eV are used as the energy units and cm as the length units.

Debye Length

The collective behavior of plasma is exhibited by screening of a small charge imbalance $\Delta n = n_e - n$, or, alternately, if a potential V_o is introduced, it gets screened as

$$V = V_o \cdot \exp\left(-\frac{r}{\lambda_D}\right) \tag{2.5}$$

where r is the distance from the point potential V_o, and λ_D is Debye length. Debye length defines the characteristic plasma screening scale beyond which quasi-neutrality can be guaranteed (see figure 1.2.1).[2]

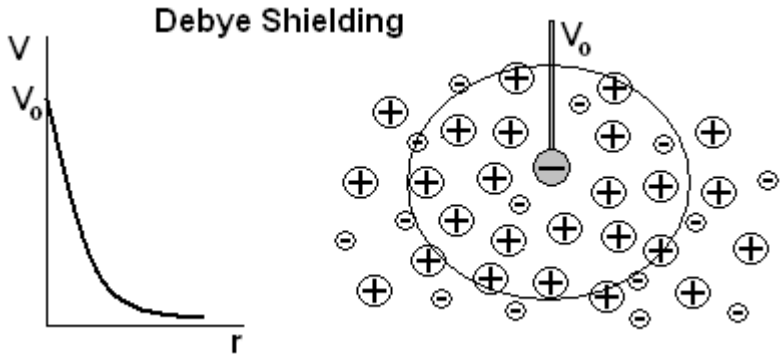

Figure 2.1 Debye shielding of an external potential Vo: charge imbalance is created within a sphere of a radius ~ λ_D (shown as a thin line around the point potential) and is then gradually restored within bulk plasma.

Debye length depends on plasma temperature and density as

$$\lambda_D = \left(\frac{\varepsilon_o \cdot k_B \cdot T_e}{n_e \cdot e^2}\right)^{\frac{1}{2}} \tag{2.6}$$

where ε_o is dielectric permittivity of free space, e is the elementary charge, k_B is the Boltzmann constant, and T_e and n_e are the electron temperature and density. If the temperature is expressed in eV and the density in cm^{-3}, it is convenient to use[2, 3]

$$\lambda_D = 742 \cdot \left(\frac{T_e}{n_e} \right)^{\frac{1}{2}} \tag{2.7}$$

that gives Debye length in cm.

Plasma parameter:

Figure 2.1 shows schematically that there are enough charged particles within the Debye sphere to accomplish shielding. For a given plasma density, the total number of particles within a sphere of a radius equal to the Debye length is given by[2]

$$N_D = n_e \cdot \frac{4}{3} \cdot \pi \cdot \lambda_D^3 = 1.71 \times 10^9 \cdot \frac{T_e^{\frac{3}{2}}}{n_e^{\frac{1}{2}}} \tag{2.8}$$

where expression (2.7) is substituted for the Debye length and T_e and n_e are the electron temperature and density in eV and cm^{-3}, respectively.

Plasma Frequency

Due to coulomb interactions, plasma is rich in wave phenomena. Resonant oscillations depend on plasma density as[2]

$$\omega_p = \left(\frac{n_e \cdot e^2}{\varepsilon_o \cdot m_e} \right)^{\frac{1}{2}} = 9000 \cdot n_e^{\frac{1}{2}} \tag{2.9}$$

where ω_p is the plasma frequency and the electron density n_e is in cm^{-3} in the last expression.

Plasma Redefined:

An ionized gas qualifies as a plasma if three conditions are satisfied:

1. $\lambda_D << L$ (2.10)

where L is the actual size of the system. This conditions means that when charge imbalances or external potentials are introduced these are shielded out in a distance that is short compared to the size of the container. This leaves the bulk of the plasma free of large fields.

2. $N_D >> 1$ (2.11)

The number of particles in the charge cloud must be large enough, so that the statistical approach to shielding is applicable. The Debye length and the electron and ion temperatures are inherently statistical concepts.

3. $\omega_p \tau > 1$ (2.12)

where τ is the time between collisions with neutral atoms of molecules. If collisions with neutrals happen at a rate greater than plasma frequency, then the plasma behaves as a regular gas and not as a plasma.[2]

If these conditions are satisfied, then collective behaviors such as shielding, formation of sheaths, interactions with external fields, and support of various types of electromagnetic waves can take place and the ionized gas is considered to be plasma. In a discharge, there may be areas of non-zero charge density, regions or times when charged particle beams are generated or are passing through, and there also may be regions that satisfy the plasma criteria.

Plasmas are usually categorized as “hot” where conditions for local thermal equilibrium are satisfied, that is, all species are thermalized to the same temperature and non-equilibrium where the electron energy is usually much higher than that of the heavy particles. Complete thermal equilibrium is difficult to achieve and most plasmas deviate from it to some degree. At pressures below one atmosphere, non-equilibrium plasmas

include glow discharge (found in fluorescent light bulbs) and ionosphere, and solar corona and fusion plasmas are hot. At normal atmospheric pressure or above equilibrium, plasmas include lightning and thermal arcs, and corona, and dielectric barrier discharges are considered "cold". Some plasmas may be characterized by two different temperatures, electron temperature (T_e) and the gas temperature (T_g). Collisions facilitate the approach of thermal equilibrium so at higher pressures plasmas are more likely to be close to thermal equilibrium.[1, 3, 4, 5] Various examples of laboratory, industrial, and naturally occurring plasmas are given in Fig. 2.2. Atmospheric pressure plasmas are the focus of the remainder of this work.

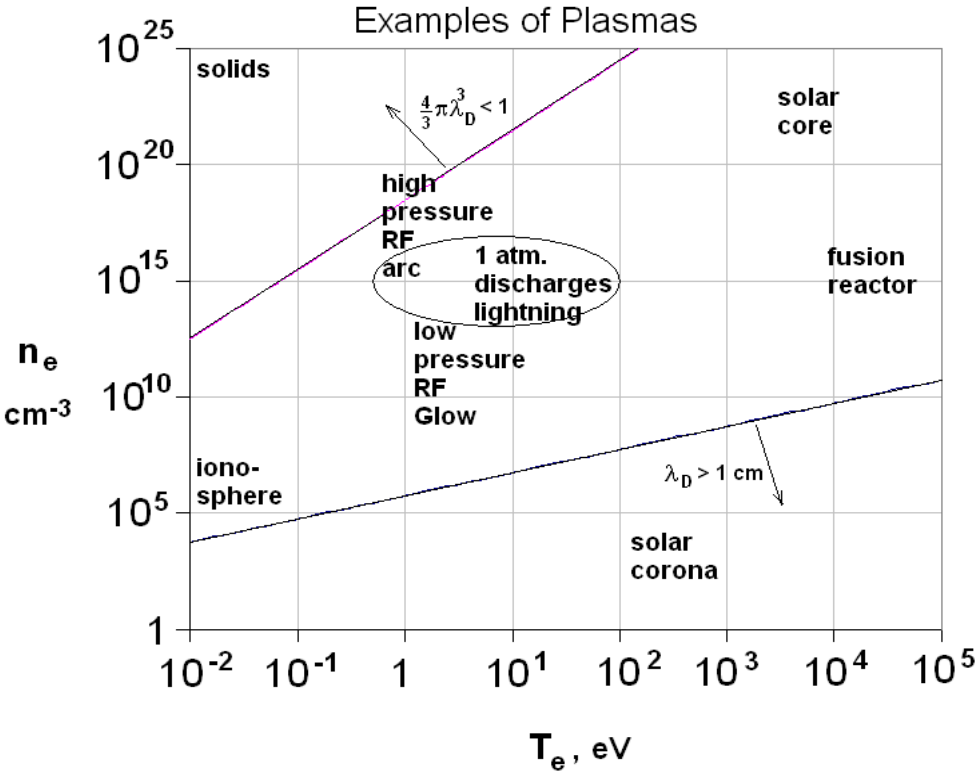

Figure 2.2 This diagram gives approximate ranges for the electron temperature (Te) and density (ne) for some examples of laboratory, industrial, and naturally occurring plasmas. The classical plasma boundaries are outlined in terms of the plasma parameter (See definition above) and Debye length ($\lambda_{D)}$ according to plasma conditions given above. [1, 3, 4]

2.2. Discharges at atmospheric pressure

Discharges at atmospheric pressure are found in Figure 2.2 in the region between a glow discharge and an atmospheric arc discharge.[4] Glow discharge has a low gas temperature (~300 K≈ 0.025 eV), a high electron temperature (~11000 K ≈1eV), and a low degree of ionization (% of gas molecules or atoms that are ionized). Thermal arcs are close to thermal equilibrium, so electron and gas temperatures are within 1% of each other (Te ≈Tg ~10000 K). Most discharges at atmospheric pressure fall between these two extremes. Applications of atmospheric pressure discharges to waste treatment or material modification are based on the use of high energy electrons and chemically active species (excited atoms and molecules and free radicals) in plasma. An increase in the gas temperature then constitutes an unwelcome side effect, since it wastes input energy used to generate the plasma and produces additional complications such as the need for cooling. Most plasmas of practical interest therefore are non-equilibrium plasmas. The principles of initiation of discharges at atmospheric pressure are described below, followed by a discussion of two examples of atmospheric pressure plasmas, corona and dielectric barrier discharges. [1, 4, 6]

2.2.1 Discharge formation:

Under static conditions, a discharge proceeds through the stages shown in Fig. 2.2.1, starting with background ionization and continuing to an arc.[9] The breakdown voltage (Figure 2.2.1) for a given gas depends on the product of pressure (p) and electrode separation (d). In addition, the specific gas composition and the frequency of

the applied voltage also influence the breakdown voltage. The standard approach to describing

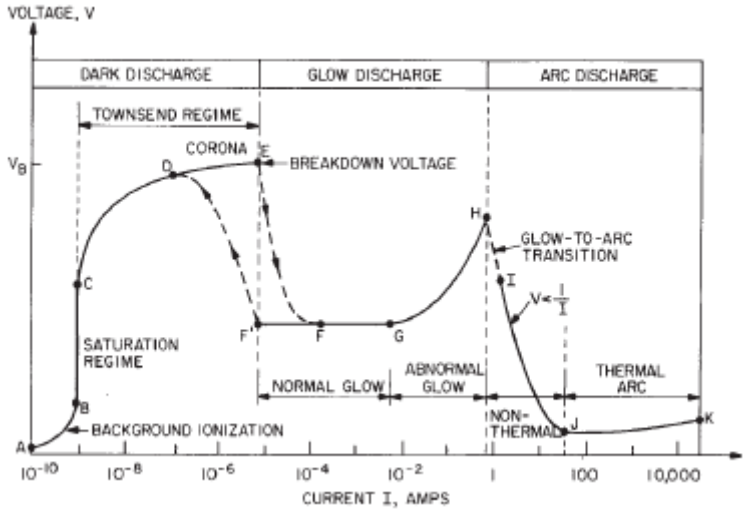

Figure 2.2.1 The figure shows variation in voltage with current when DC voltage is applied between two electrodes immersed in a gas, and the outside circuit is adjusted appropriately.[7, 9]

discharge initiation through multiple electron avalanches eventually reaching self-sustainment apply to discharges at high pressure also. Current amplification by ionization processes can be written as[3, 6]

$$I = \frac{I_o \cdot e^{\alpha \cdot d}}{1 - \gamma \cdot \left(e^{\alpha \cdot d} - 1\right)} \qquad 2.13$$

and the breakdown condition as

$$\gamma \cdot \left(e^{\alpha \cdot d} - 1\right) = 1 \qquad 2.14$$

Here, α and γ are the first and second Townsend coefficient, describing the number of new electrons produced when an electron travels a unit length along the direction of the outside field. In a low pressure glow discharge, the secondary electrons come from the

cathode. Ion bombardment of the cathode provides the electrons needed to initiate new avalanches and sustain discharge development. In general, the secondary electrons can come from volume processes. The secondary emission coefficient includes contributions of new electrons by ions, photons, fast atoms, and metastable atoms and molecules. [3, 6]

In the presence of electronegative gases, the attachment processes become important. If the attachment coefficient is η, then the effective ionization coefficient becomes $(\alpha - \eta)$ and the condition for a self-sustained discharge becomes:

$$\frac{\gamma \cdot \alpha}{\alpha - \eta} \cdot \left[e^{(\alpha - \eta) \cdot d} - 1 \right] = 1 \qquad 2.15$$

The main feature of the Townsend mechanism is a low plasma density. The density of charge carriers is low enough so that the external field responsible for avalanche development is not altered by the new charge. High electric fields combined with a large number of collisions can produce enough electrons in an avalanche to significantly affect the external field. For the Townsend mechanism to hold, the number of electrons in an avalanche cannot exceed a critical value

$$N_o \cdot e^{\alpha \cdot d} \lesssim N_{cr} \qquad 2.16$$

or with attachment,

$$N_o \cdot e^{(\alpha - \eta) \cdot d} \lesssim N_{cr} \qquad 2.17$$

where (N_{o}) is the initial number of electrons and (N_{cr}) is about 10^8. The first coefficient depends on the applied field, so at high pressure this condition can be met with a high enough field. The applied field may be enhanced by non-uniformities, or the voltage applied to the electrodes may be much higher than the minimum breakdown voltage (high overvoltage). Under these conditions breakdown development is much faster than

multiple avalanches fed by electrons from the cathode would allow. The discharge then develops by the streamer mechanism that forms a thin conductive channel.[3, 6] More on the streamer breakdown mechanism can be found in the discussion section 4.5 of this work.

The diagram in Fig. 2.2.1 is plotted for a low pressure dc discharge. The general tendencies hold for high pressures as well, but various different paths may be achieved by changing the frequency or the duration of the applied voltage. High (kHz range and above) frequencies of applied voltage pulses leads to residual ionization remaining in the plasma (plasma channel in case of a streamer breakdown) which affects discharge formation in the following cycles. A short duration of voltage pulses can prevent current build up and avoid transition to arc and/or keep the discharge in a non-thermal state.[3, 6, 8] Discharge behavior under low frequency pulsed voltage is investigated experimentally in this work.

Previous studies of discharges at atmospheric pressure include detailed studies of corona and dielectric barrier discharges and, recently, formation of the atmospheric pressure glow discharge.

2.2.2 Corona discharges at atmospheric pressure

At a high enough electric field, a corona discharge can be observed around wires and sharp edges. The nature of a corona discharge is tied to the non-uniform character of the electric field. To produce a corona discharge at least one of the electrodes must be sharpened to a radius much smaller than the inter-electrode distance.[3, 5, 6]

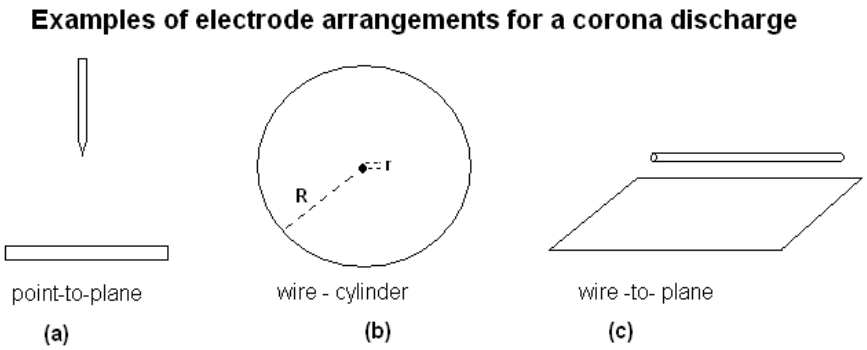

Figure 2.2.2 Examples of electrode arrangements for a corona discharge.

A needle-to-plane electrode geometry is one such arrangement, when the distance between a needle and a plane is much greater than the thickness of the needle. The maximum value of the electric field then depends on the applied voltage and the radius of the sharp electrode. For example, the maximum field between a sphere of a radius (r) and a remote plane is $E_{max} = V/r$. That means that coronas require lower initiation voltage than uniform gaps for the same inter-electrode distance.[3]

The ionization is limited to the high field region around the sharp electrode. If a sharp electrode is negative, the corona develops by an electron avalanche process. Condition 2.15 has to be satisfied to ensure sustainment of the discharge. The secondary emission coefficient (γ) includes electrode surface and gas bulk processes (electron emission from ion bombardment of the cathode, from excited atoms and molecules, and from photons). Outside of the immediate area around the sharp electrode, the field is weak and charged particles are too slow for ionization to continue. In case of a negative corona, the inter-electrode space has an excess space charge made up of electrons and negative ions (in the presence of electronegative gases). This space charge limits the corona discharge, since it prevents injection of additional negative particles into this

region. Higher applied voltages are needed to increase the corona current. In case of very high fields, a corona can transition to a streamer and form a spark. To transition to a streamer, the number of electrons in an avalanche has to exceed a critical value (2.17).[5, 3, 6, 10]

The usual continuous corona has currents 10 – 100 μA. Currents of ~10 A or greater are possible without transition to a spark using short, nanosecond voltage pulses (~100 – 200 ns). The time needs to be short enough to prevent transition to thermal equilibrium. Pulsed corona discharges have been attracting more interest since these regimes are capable of higher power with the plasma remaining non-equilibrium.[10]

Current applications of corona discharges include electrostatic precipitators (historically the first large scale industrial application), surface modification, and pollution control. A corona discharge is a space limited, non-equilibrium discharge at atmospheric pressure.

2.2.3 Dielectric barrier discharges

Another way to prevent the discharge transition to spark at high voltage is to use a dielectric material on one or both electrodes. The discharge that occurs then is called *a dielectric barrier discharge* (DBD). Various possible electrode-dielectric configurations are shown in Fig. 2.2.3.

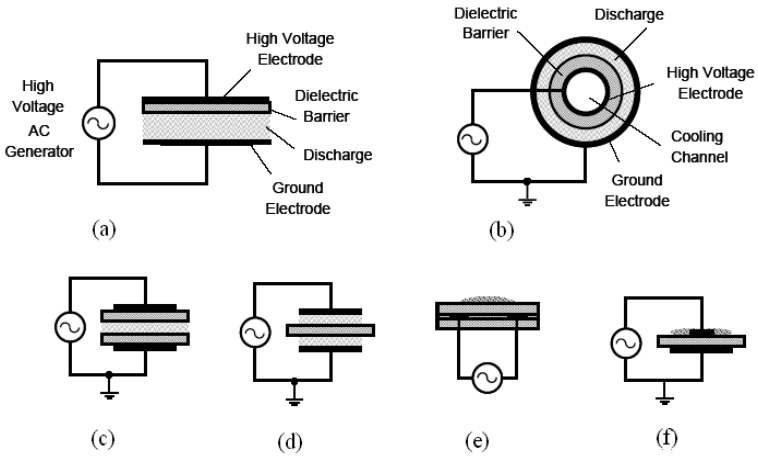

Figure 2.2.3 Different types of electrode configurations for dielectric barrier discharge[11]

DBDs operate at applied voltages of 100 V to ~10 kV with frequencies of 0.5 – 500 kHz. These discharges are used for ozone production and in CO_2 lasers. The discharge gap is usually from 0.1 mm to centimeters. DBD proceed usually through a large number of filaments. The discharge oscillograms show characteristic sharp current peaks (see Fig. 2.2.4). Each individual filament usually develops as a streamer and forms a conductive discharge channel of 50 – 100 mm radius. The plasma produced in a DBD remains highly non-equilibrium with the average electron energy in the 1 – 10 eV range and the gas temperature close to 300 K. Additional parameters of these discharges are found in Section 4.5.

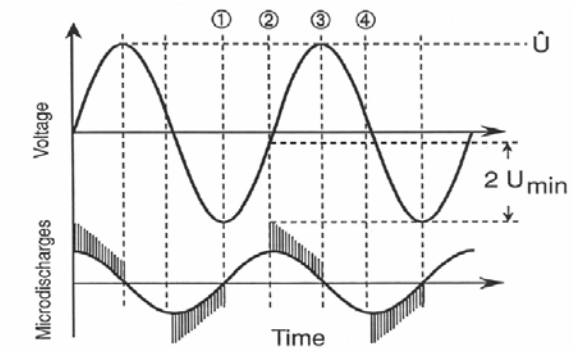

Figure 2.2.4. Sharp current peaks characteristic for a barrier discharge.[6, 11]

2.2.4 Current Advancements

The advancement in the basic understanding of discharges at atmospheric pressure, such as coronas and DBDs for example, comes from the progress in temporal and spatial modeling as well as from the new techniques used in experimental investigations. The discharge process occurs on several different time and space scales. Filamentary discharges or branching streamers are modeled in two dimensions and these models give highly resolved information on spatial development. The time step in these models and is too large to gain insight into the temporal development. The long time scale is useful for some longer chemical processes and for calculating gross yields of the desired chemical product. If a short sub-nanosecond or nanosecond time scale is used, then the discharge is often treated in one dimension. One-dimensional approaches are useful for situations with a high degree of symmetry.[11-25]

R. Barni et al modified a low-pressure chemical kinetics model to describe atmospheric pressure air plasmas in the streamer regime.[12] Reference data for input parameters such as the electron temperature and density and reaction rates is used in their model. The model is used to simulate chemical kinetics induced in a single isolated streamer and predicts the evolution of the gas-phase chemical composition. The plasma temperature and density are varied to see their effect on the final composition. The time scale of this model is rather rough, but it does show significant cooling of the electrons following the initial fast streamer formation/ionization stages. It also shows significant accumulation of stable secondary products and therefore, a significant effect on the pulse repetition rate (in the 1 kHz – 1 MHz range) on the final chemical composition.[12] The

discharge in other gases or mixes of gases has been studied from the point of view of chemical kinetics.[14-17] For example, simulation and experimental measurements of hydrogen, oxygen, and hydrogen peroxide production in a humid Ar DBD[14] and simulations of NO_x formation simulated in humid air have been conducted on a long time scale.[15]

K. Kozlov, H-E. Wagner and their colleagues at Moscow State University and University of Greifswald have conducted extensive theoretical and experimental investigations into the physical behavior and the properties of dielectric barrier discharges in air and N_2/O_2 mixtures at atmospheric pressure.[18-22] These groups have made significant contributions to the detailed understanding of DBDs because they combine computer modeling with experimental work.[18-22] K. Kozlov *et al* points out both the need and the difficulty of obtaining experimental information about the individual filaments (or microdischarges) constituting a DBD.[18] High temporal (sub-nanosecond) and spacial (down to 0.1 – 0.001 mm) resolution is required. The authors use their own experimental data for qualitative characterization of the structure and processes within a single discharge channel. It is interesting to point out the interpretation of time and space resolved optical and current data.[18] Observations of a wave of intensity from N_2^+ B(0-0) band with a threshold ~19 eV correspond to the propagation of the ionization wave (or steamer propagation). The luminous regions near the cathode and anode are different with higher electric field strength and lower electron density near the cathode than the anode region. The changes in electric current are interpreted to correspond to the change in electric field. In addition, the contributions of ions in the channel increases during the decay phase as the electrons leave the channel. The time

scale for various physical and chemical processes in a single streamer is shown in Fig. 2.2.5 (from Wagner et al, [19]). Specific properties of a microdischarge are also given in Table 2.2.1. The multiscale nature of streamers is also addressed by Ebert et al.[23] This work discusses changing approaches to modeling and experimentation depending on the scale of the effect considered, such as ionization front on a subnanoscale time scale and streamer branching occurring on a much longer time and distance scales.[23] Computer models are also written to simulate resulting optical emission. Plasma parameters are again manipulated to fit the experimentally observed spectra.[24, 25] The models and experiments show that the streamer channel has non-thermal plasma conditions throughout, with non-zero charge density limited to the cathode and anode regions.

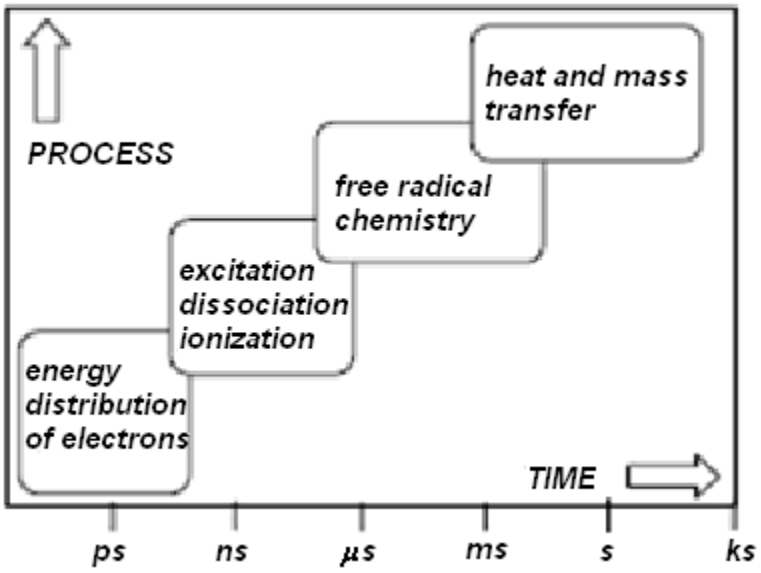

Figure 2.2.5. Time scale of relevant processes for a filamentary barrier discharge.[19]

Table 2.2.1 Properties of a microdischarge channel.[9]

Characteristic properties of a microdischarge channel in air at atmospheric pressure	
Duration: a few nanoseconds	Total transferred charge: 10^{-10}–10^{-9} C
Radius of filament: about 0.1 mm	Density of electrons: 10^{14}–10^{15} cm^{-3}
Peak current: 0.1 A	Mean energy of electrons: 1–10 eV
Current density: 10^{6}–10^{7} A/m^2	Gas temperature of microdischarge: near room

2.2.5 A note about water

De-ionized water has an electric conductivity of 0.05501 μS cm^{-1} at 25°C, relative dielectric constant of 87.9 at 0°C and 78.4 at 25°C and the dielectric relaxation time of 9.55 x 10^{-12} s at 20°C.[26-28] Water is used as an insulator in high voltage pulsed-power systems, for example, those used on the accelerators at Sandia National Laboratory.[29] The studies of streamer formation in water in a point-to-plane geometry show that for pulses ~1 μs in duration the water breakdown field is ~ 10 MV/cm, about five times higher than the breakdown field at static conditions.

References:

1. M. Lieberman, A. Lichtenberg, (1994), *Principles of Plasma Discharges and Materials Processing*, John Wiley and Sons, New York
2. F. Chen, (1984), *Introduction to Plasma Physics and Controlled Fusion*, Volume 1, Plenum Press, New York
3. Fridman, L. Kennedy, (2004), Plasma Physics and Engineering, Taylor & Francis, New York
4. Tendero, C. Tixier, P. Tristant, J. Desmaison, P. Leprince, (2006), Spectrochimica Acta Part B, **61,** 2 – 30
5. Yu. P. Raizer, (1991), Gas Discharge Physics, Springer-Verlag, Berlin
6. K. Becker, U. Kogelschatz, K. Schoenbach, R. Barker, (2005), Non-Equilibrium Air Plasmas at Atmospheric Pressure, IOP Publishing, Philadelphia

7. J. Roth, J. Rahel, X. Dai1 and D. Sherman, (2005), J. Phys. D: Appl. Phys. **38**, 555–567
8. R. Hippler, S. Pfau, M. Schmidt, K. Schoenbach, (2001), Low Temperature Plasma Physics, Wiley-VCH, Berlin
9. Eliasson, U. Kogelschatz, (1991), Trans. Plasma Sci., **19**(2), 309
10. A Fridman, A Chirokov and A Gutsol, (2005), J. Phys. D: Appl. Phys. **38** R1–R24
11. U. Kogelschatz, (2003), Plasma Chemistry and Plasma Processing, Vol. 23, No. 1, R1-R24
12. R. Barni, P. Esena,, C. Riccardi, (2005), J. Appl. Phys., **97**, 073301
13. J. Skalny, A. Stoica, J. Orszagh, R. Vladoiu, N. Mason, (2008) J. Phys. D: Appl. Phys. **41** 175211
14. M.J. Kirkpatrick, B. Dodet, E. Odic, (2007), International Journal of Plasma Environmental Science & Technology Vol.1, No.1
15. K. Iskenderova, A. Chirokov, A. Gutsol, A. Fridman, K.D. Sieber, J. Grace, K. Robinson, (2001), Proc. 15th Int. Symp. on Plasma Chemistry, v II, 443-448
16. G. Naidis, (2005), J. Phys. D: Appl. Phys. **38** 3889–3893
17. O. Goossens, E. Dekempeneera, D. Vangeneugdena, R. Van de Leesta, C. Leys, (2001), Surface and Coatings Technology, **142-144**, Pages 474-481
18. K. Kozlov, H-E. Wagner, R. Brandenburg, and P. Michel, (2001), J. Phys. D: Appl. Phys. **34** 3164-3176
19. H-E. Wagner, R. Brandenburg, K. Kozlov, A. Sonnenfeld, P. Michel, J. Behnke, (2002), Vacuum, **71**, 417-436
20. R. Brandenburg, H-E. Wagner, A. Morozov, K. Kozlov, (2005), J. Phys. D: Appl. Phys. **38,** 1649-1657
21. K. Kozlov, R. Brandenburg, H-E. Wagner, A. Morozov, P. Michel, (2005), J. Phys. D: Appl. Phys. **38,** 518-529
22. H-E Wagner, Yu. Yurgelenas, and R Brandenburg, (2005), Plasma Phys. Control. Fusion **47** B641–B654
23. U. Ebert, et al, (2006), Plasma Science Technology, submitted for publication
24. Lu, M. Laroussi, (2006), J. Phys. D: Appl. Phys. **39**, 1127–1131
25. Farouk T., Farouk, B., Staack , D., Gutsol, A., and Fridman, A., (2006), Plasma Sources Science and Technology, **15**, 676-688
26. T. S. Light, S. Licht, A. C. Bevilacqua and K. R. Morash, (2005), *Electrochem. Solid-State Lett.* **8** E16-E19
27. J. N. Murrell, A. D. Jenkins, *Properties of Liquids and solutions,* 2nd Ed. (John Wiley & Sons, Chichester, England, 1994)
28. Eisenberg and W. Kauzmann, *The structure and properties of water* (Oxford University Press, London, 1969)
29. W. A. Stygar, *et al*, (2006), Phys. Rev. ST Accel. Beams **9,** 070401

3. Experimental set-up and methodology

3.1. General information

The purpose of the study is to observe and determine the properties of an electrical discharge in a gas bubble submerged in water. As discussed previously, the discharge in bubbles in water has possible application for water treatment. To provide useful information for the development of this water treatment methodology, this study tries to match some of the experimental conditions and general needs of the treatment systems. Bubbles used in water treatment experiments are usually from 1 – 30 mm in diameter, touching one or both electrodes submerged in water, and subjected to high voltage pulses. [1, 2] For treatment purposes, the power used should be kept low, if possible. These conditions motivate the choice of the experimental parameters chosen here.

The bubbles studied are 2 – 10 mm in diameter with most experiments conducted with 8 mm bubbles. 1 μs long, 6 – 20 kV voltage pulses are applied to Ar or O_2 bubbles and (in a small number of cases) air. The voltage pulses are applied between needle and disk electrodes submerged in water, and the bubble is positioned around the needle electrode. The bubbles do not touch the disk electrode. Electrical and optical measurements are carried out concurrently, and each new experimental condition starts with a new bubble and de-ionized water. The water conductivity remains in the range of 1.2 – 1.5 μScm, pH stays between 4.9 and 5.0, and the temperature remains 20 – 21 ^{0}C throughout all of the experiments.

3.2. Experimental chamber

The experimental chamber is designed to hold the water, bubble, and electrodes and to allow optical and electrical measurements. The chamber itself was made out of a solid block of polypropylene. This material is chosen for its high chemical stability and dielectric properties. The Blumlein line pulse shaping network used for applying the required voltage is highly sensitive to the circuit impedance (See Section 3.3). It is important therefore, not to change the matching impedance by introducing a load to the circuit. Preliminary experiments showed that the shape of the voltage signal does not change when the load is connected with or without the discharge in the bubble. The experimental chamber as constructed does not affect the electrical system of this experiment.

The chamber was made from a 4”x 4”x 4” polypropylene block. The water filled cavity is formed at the intersection of two horizontal and one vertical bore. The two horizontal bores are drilled 1” in diameter and are fitted with quartz windows for observation and imaging taking. The window flanges are provided with a black covers when needed. The vertical 1.5” diameter hole is drilled from the bottom and meets the two horizontal cylindrical holes to form the cavity containing water.

A horizontal disk electrode is at the bottom of the chamber and it is fitted with a micrometer adjustment as shown in Fig. 3.2.1. The micrometer is used to change and to measure the distance between the needle and disk electrodes. The distance is adjusted so that the minimum discharge voltage in an Ar bubble does not go below about 7.5 kV. This voltage minimum is needed for proper operation of the Thyratron switch used in the electrical system (Section 3.3). The needle electrode is attached to gas line and it is

located in the opening on the top of the chamber. The opening is threaded and allows accurate vertical adjustment of the needle.

The chamber has two pressure release valves. The valves are usually open to maintain ambient pressure in the chamber. In case a bubble escapes, the extra gas can also escape through the valves.

To be able to study each single discharge process in a bubble, the bubble must remain at rest, the size must be controlled at least approximately, and the bubble needs to be accurately positioned within the chamber and, in particular, relative to the needle electrode. Meeting these conditions while maintaining the bubble submerged presents a major experimental challenge. The chamber described here and all the associated systems are designed to meet this challenge.

The gas system is designed to deliver an accurate amount of gas slowly, each time a new bubble is needed. A MKS 247 gas mass flow controller feeds the gas into the gas line at a slow rate (~0.5 cm^3/min). A three-way valve (Fig. 3.2.1) is used to direct the gas flow to an SGE micro-syringe (100 μL volume, μL divisions), then to stop the flow and open the line to the needle. The syringe is used to slowly release a desired amount of gas into the water and form a bubble. The bubble is formed around the opening in the top of the chamber, where the needle is positioned while the needle is flush with the opening. The threaded opening is used then to advance the needle 0.5 – 1 mm into the bubble. The 0.5 mm length is used in the experiments discussed in this work. A digital camera is used to record the size of the bubble. The bubble is photographed at the beginning and at the end of an experiment to make sure there are no changes in size and/or location of the bubble (Fig. 3.2.2).

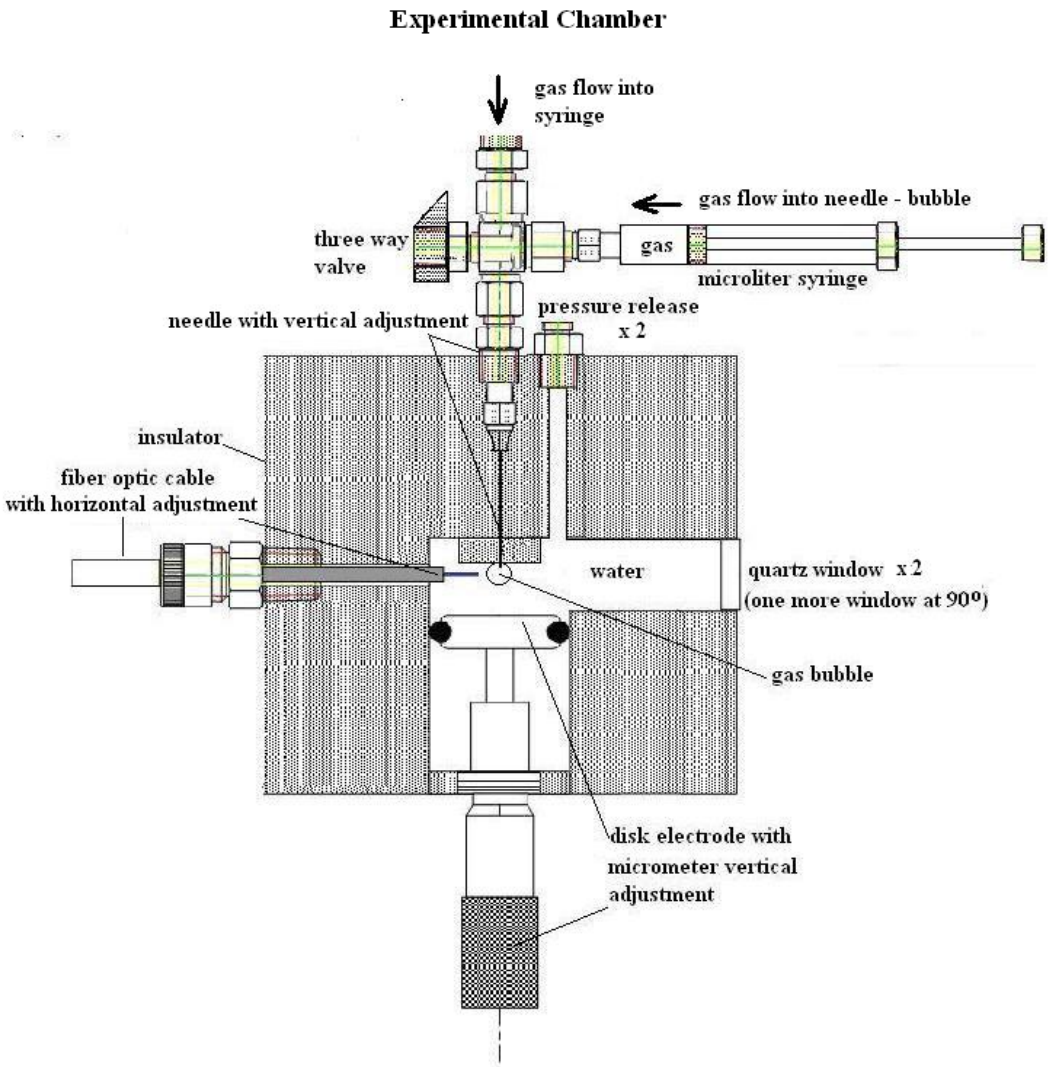

Figure 3.2.1 Experimental chamber for electrical discharge in a gas bubble in water. The figure shows the needle and disk electrode arrangement, viewing ports, the gas supply system, and the fiber optic cable arrangement. The bubble is positioned at the top of the chamber around the tip of the needle.

The chamber has an adjustable feedthrough for the fiber optic cable (1mm single core by RoMAC). One of the major advantages of this chamber is in the precision alignment of the fiber optic cable, the needle. Adjusting the position of the fiber horizontally is important to accommodate for various size bubbles. The experimental

chamber is positioned on an optical table and carefully leveled to maintain the position of the bubble and optical alignment of the instruments.

This system makes it possible to generate a single bubble relatively consistently. The bubbles have consistent dimensions and are well centered in the chamber. This experimental arrangement allows the study of a single stationary bubble with just the tip of the needle extending into the bubble.

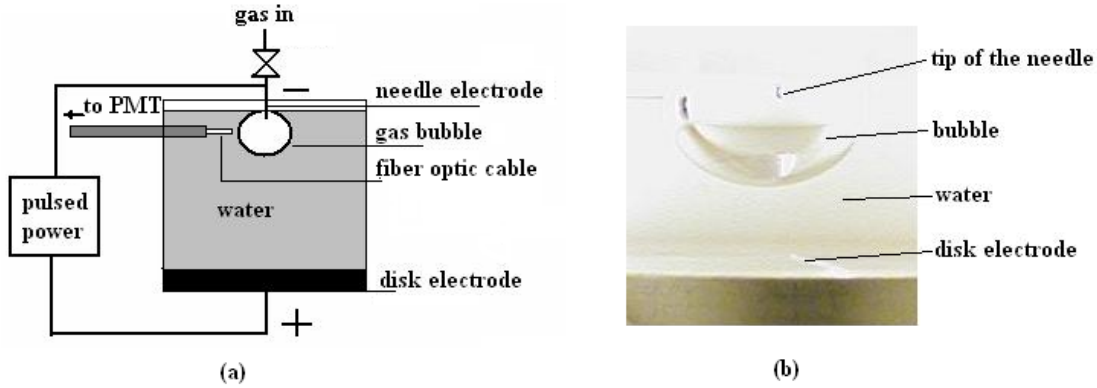

Figure 3.2.2 (a) Schematic diagram of the bubble – water arrangement showing the bubble around the needle electrode with the disk electrode immersed in water. Gas is fed through the needle and a stationary bubble forms surrounding the tip of the needle. **(b)** A sample photo of the bubble and the electrodes

3.3 Electrical System

The properties of the discharge, the parameters of the plasma produced by the discharge, and the chemical reactions activated by the discharge process, all depend critically on the type of applied power. A pulsed power regime has been adopted for this study, because it allows the generation of energetic electrons and high charge densities without overheating the system. A short pulse should be used to avoid the transfer of energy to heating the operating gas and other circuit components. Molecular vibrations are at the core of the dissociation process, so it should be beneficial to transfer some of the electrical energy supplied by the circuit to the vibrational energy of the molecules. The duration of the pulse has to balance between overheating and not engaging molecular processes at all. Based on the time scale of various processes in the discharge, a 1 μs pulse duration time should serve the purpose of creating a chemically active environment by including the processes of excitation, ionization, and dissociation (See Fig. 2.2.5).

A Blumlein line pulse shaping network was constructed for this experiment at Old Dominion University by the pulsed power group under the direction of Dr. Schoenbach. A Blumlein line is usually constructed using two coaxial cables and the length of the cables determines the duration of the voltage pulse.[3, 4] Due to a slightly longer pulse length required for this experiment, the pulse shaping network is built using two chains of capacitors and inductors. The pulse shaping network is designed to provide relatively rectangular pulses about 1 μs in duration and 0 – 30 kV in magnitude. Sample oscillograms of the potential at each output electrode and the actual voltage pulse between the electrodes (the difference in potential) are shown in Fig. 3.3.1. The shape of the signal and particularly, additional oscillations past the pulse length, are avoided by

adjusting the matching resistance at the output of the Blumlein line. In this circuit a 35 Ω resistance is used. This resistance provides a good match during the operation of the discharge chamber, since the resistance between the load electrodes never falls below the dc resistance of de-ionized water ~ 1 MΩ.

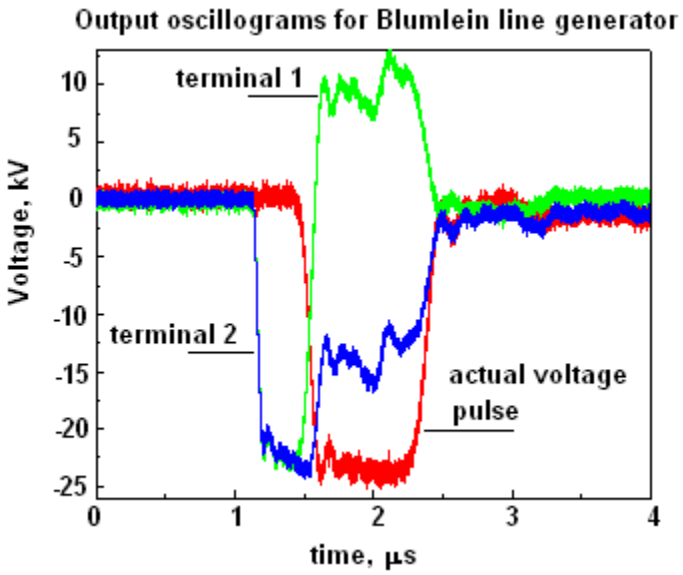

Figure 3.3.1 The output oscillograms for the Blumlein line pulse-shaping network used in this experiment. The actual pulse delivered to the system is the difference between the potentials at each output terminal.

A DC Glassman EK0R10 0 – 60 kV, 10 mA power supply charges the pulse generator. The charging resistor is 20 MΩ and the charging current never exceeds 3 mA. The input power delivered by the DC power supply to the experimental system has remained in the range of 1 to 40 W in all experiments described in this work. An EG-G Hydrogen Thyratron (HY 3003) switch delivers the voltage pulse (See the circuit diagram in Fig. 3.3.2) by completing the ground connection and starting the pulse propagation in the Blumlein line. The voltage is generated across the load (experimental chamber) approximately a half period (0.5 μs) later. The Thyratron switch is activated using the

EG-G (TM 247) Thyratron Driver and can be triggered manually or pulsed at a rate of 0 Hz to 1 kHz. Manual triggering is used here in single pulse experiments or when it is important to record the exact number of pulses. For multiple discharges and multiple accumulations a 1 Hz pulse rate is used.

The voltage across the load is measured using Tektronix P6015A 75 MHz HV probes; a Pearson high band pass current probe (model# 6600) is used to measure the current. A Tektronix TDS 3034 digital oscilloscope (300 MHz band pass and 2.5 GS/s sampling rate) records all current, voltage, and photomultiplier signals.

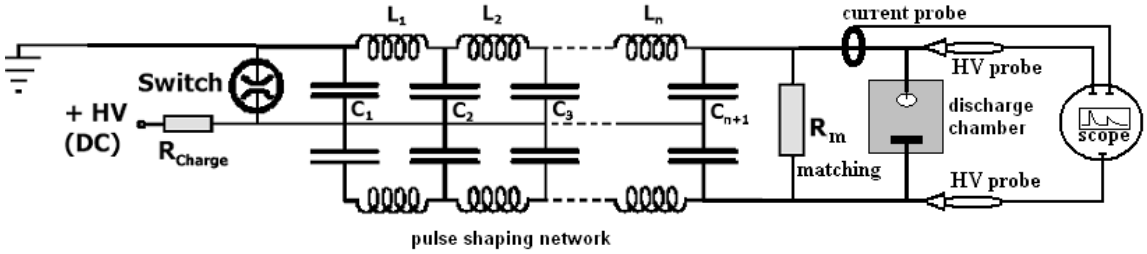

Figure 3.3.2 The diagram shows the main components of the electrical system including the DC power supply, the Thyratron switch, Blumlein line pulse shaping network with a 35 Ω (R_m) matching resistor, the water chamber and the voltage and current probes.

The voltage signal applied to the needle-disk electrodes has a <100 ns rise time and is therefore radiates in the 100 MHz range. The electromagnetic interference (EMI) provided by the applied voltage pulse, is caused by the combination of the fast rise time (~0.5 kV/ns) and high voltage. Three types of interference need to be addressed in the real operating circuit. Currents are induced in stray inductances or any accidental loops. Ground loops also transmit the induced currents to other equipment. This interferes with the operation of the computers, oscilloscopes, photomultiplier tubes, digital counters and controllers. In addition to identifiable loops, ground loops and short circuits are created at

high frequencies by stray capacitances between various circuit elements due to close proximity or the large size of the connectors and cables. Radiated, inductive, and capacitive interferences must be addressed to insure robust operation and proper measurements.

To interrupt the radiated electric field, a copper shielded box is constructed. The box is a 4'x 4'x8' plywood box covered inside with a commercial shielding material and on the outside with 22 gauge copper sheeting. A 1" gap between the inner and outer shielding prevents interference from the skin effect at lower frequencies. All equipment is placed inside the box and everything including all wiring, connections, and equipment is placed a minimum of 3" from all walls. The circuit is physically arranged with short connections, and loops are eliminated whenever possible. All capacitances are reduced whenever possible by reducing the size of all connections and increasing the distances between them. All connections to the line power inside the shielding box are made through a low capacitance isolation transformer. The shielding box is equipped with shielded connector boxes and all coaxial cables are semi-rigid double shielded with solid copper shielding. One physical ground is provided for the entire circuit by properly grounding the entire box.

Throughout all experiments, the diagnostic equipment remaining outside the box has suffered no ill effects from either the applied voltage pulse or the discharge itself. All shielding equipment has been constructed in the lab for this experiment. Figure 3.3.3 shows two oscillograms of the photomultiplier (PMT) signals recorded in preliminary experiments before the shielding and circuit modification was in place, and those after all EMI reduction measures have been put into place. The improvement of the signal is

significant. The challenge of EMI inherent in any work with pulsed power has been adequately addressed in this experimental set-up.

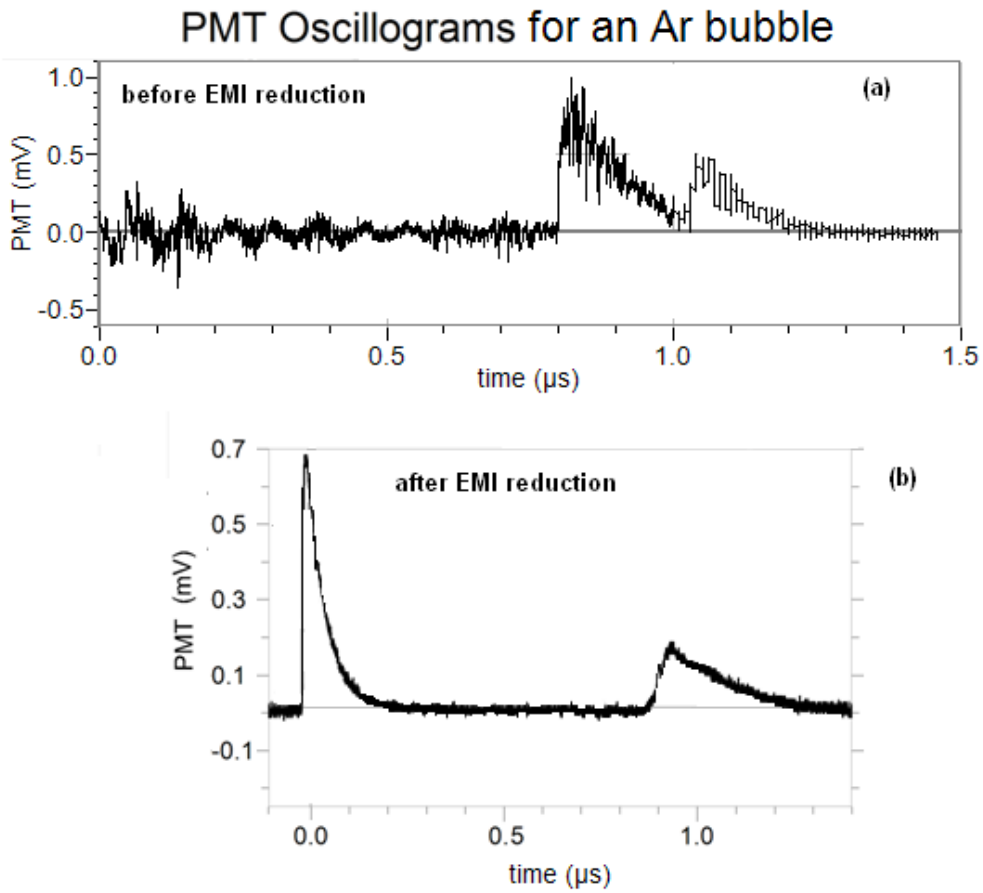

Figure 3.3.3. Sample oscillograms are presented here to illustrate noise reduction. The chosen oscillograms show the PMT signal since it is particularly sensitive to EMI. The timing of the peaks or any other features specific to the individual experiments are irrelevant here.

The electrical system used for this investigation makes it possible to apply 1 μs in duration and 0 – 30 kV voltage pulses between the needle and the disk electrodes in the water bubble system and to measure with adequate time resolution, the voltage, current, and PMT oscillograms of the electrical discharge in the bubble.

3.4 Optical System

Three different investigations have been conducted in this work using the optical emission from the discharge. The electrical arrangement remains the same in all three investigations. The current and voltage oscillograms are recorded along with the other measurements to provide information about the discharge. The set-up and modifications for each investigation are described below.

3.4.1 Photomultiplier Tube (PMT) set-up

A Hamamatsu cooled PMT (H7422) is used together with several band pass filters to investigate the evolution of an optical emission from the discharge in a gas bubble in water. The light emitted by a discharge in a bubble is picked up and transmitted by a fiber optic cable. The cable is designed for this experiment and constructed by RoMAC Inc. The fiber optic cable is 1000 μm in diameter quartz single core fiber (See Figure 3.4.1 for more information). The cable is centered on the discharge immediately below the tip of the needle. The cable is inserted into the chamber using a movable feedthrough so that the fiber can be adjusted horizontally without any water leakage. In all experiments, the fiber is positioned about 0.5 mm from the bubble. The bubble does not touch the fiber at any time during the discharge. The cable is designed with 1.4” of the bare fiber protruding at the end closest to the bubble. The purpose of the bare end is to avoid introducing another conductor and changing the electric field configuration and the impedance of the chamber. The fiber passes through a special feedthrough in the shielding box and connects to the PMT.

A set of lenses is used between the fiber optic connection and the PMT to optimize the use of the cathode area. The PMT has a 0.78 ns rise time and a < 2 ns pass time, providing temporal resolution of about 2 ns. Oriel 10 nm wide band pass filter are used with center wavelengths of 310 nm, 750 nm, 760 nm, 777 nm, 810 nm, and 840 nm. All current, voltage, and PMT data are recorded by a digital Tektronix TDS3034 4-channel oscilloscope. The experimental chamber, the power supply, and the pulse-shaping network are enclosed in a shielding box (as described previously) to prevent any interference with the testing equipment.

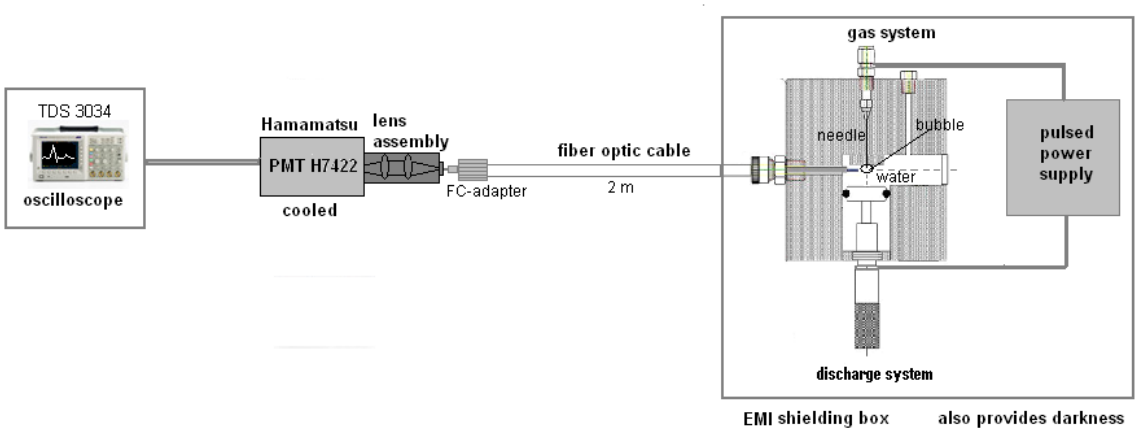

Figure 3.4.1. The figure shows a schematic diagram of the set-up for optical emission measurements using a PMT.

3.4.2 Emission Spectroscopy

Spectroscopic study uses a SPEX monochromator (by Jobin-Yvon Horiba) with a PI-MAX Intensified gated CCD camera (by PI Acton). The light is transferred from the bubble to the monochromator entrance slit by the fiber optic cable described previously. The monochromator is adjusted so that a 40 nm spectral window is projected onto the camera. The spectral resolution is 0.15 nm. The spectrum is recorded using the ICCD,

and the monochromator can then advance to the next desired spectral region. Each spectrum is produced using 50 – 100 accumulations with pulsed power applied at 1 Hz. Figure 3.4.2 shows the diagram of the set up used for spectroscopy.

This investigation is designed to study light emission from a pulsed 1μs long discharge process. Since the light source is not continuous, gating is required. The PI-MAX ICCD is capable of taking images or spectra with exposure times down to the ns range. Exposure times used in this investigation are 5, 10, 20, 100, 200, 400, 800, and 1200 ns. The camera is gated electronically, allowing for fast on/off times. The repetition rate of the exposures is limited by the readout and clean cycles that add up to approximately 800 μs. It is therefore not possible to take any more than one image within the time of one discharge event. An additional difficulty comes from a relatively high background level of PI-MAX, since is cooled only to -20 ^{o}C. A low intensity signal can be drowned by the background noise in this device.

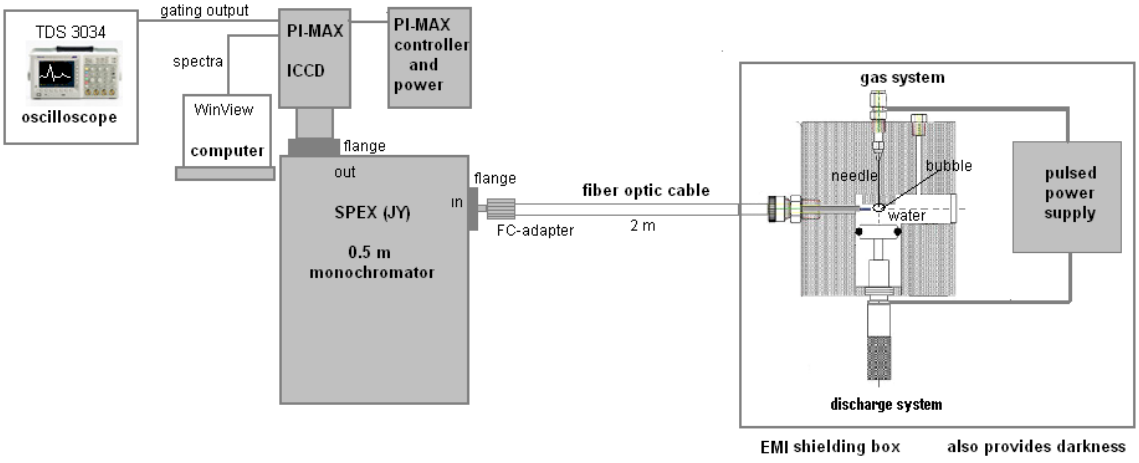

Figure 3.4.2. The figure shows the set-up used to record optical emission spectra from the discharge.

Once an exposure time is chosen, the time balance is calculated to determine the delay time for gating the camera. All delay times in this experiment are calculated from the time the Thyratron switch is activated. The Thyratron driver sends a signal to the PI-MAX driver the same time as it activates the Thyratron switch. The oscilloscope is used to determine the time delays between the signals, since all cables are adjusted to the same length. PI-MAX has a feedback feature that puts out a low voltage signal to the scope when the camera is on. A sample of the camera gating signal recorded in a preliminary experiment is shown in Figure 3.4.3. This feature greatly simplifies the timing decisions for this experiment.

Two types of timing sequences are used for recording spectra and images, repeated and sequential. These terms refer to a chosen delay for the start of the recording time, the "shutter open" moment. In a repeated mode, the delay remains the same and any number of accumulations is possible with the same gate width and the same delay. This type of recording protocol is used for all spectra. For example, the gating shown in Fig. 3.4.3 is used to take 50 – 100 accumulations of spectra during the first 100 ns of the discharge, the time of the first current peak. The accumulations correspond to individual discharge processes pulsed at 1 Hz. The delay and the gating may be changed then and a new run conducted taking the spectra during a different moment or with a different exposure time. More information about the procedure and the resulting spectra is found in Section 4.2. Both sequential and repeated modes are used for recording images of the discharge.

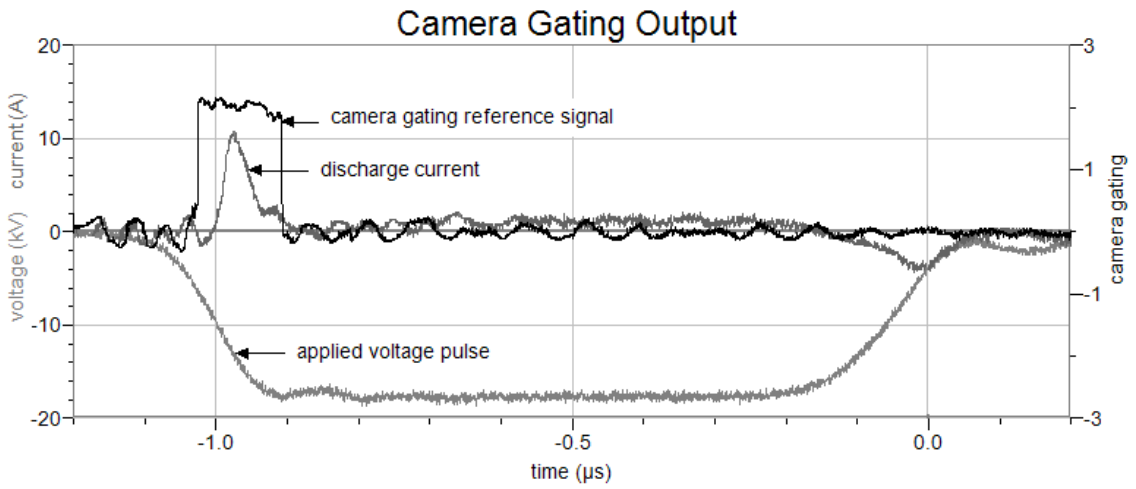

Figure 3.4.3. This figure shows the oscillograms of the applied voltage, the discharge current, and the camera output signal. The camera signal marks the time when the camera is "open" and records the images or spectra.

3.4.3 Imaging

A PI-MAX ICCD is used for imaging the discharge. The camera is fitted with an objective lens and positioned on the optical table next to the experiment chamber. A coupling device and a positioning stage are used to center the camera on the bubble. The images are taken directly through a quartz window on the chamber (Figure 3.4.4). Gating is used to take images with different exposure times and at different times during the discharge. Images are bright enough that multiple accumulations are not used.

The repetitive mode in this case produces images of the same period during each discharge for each individual discharge event. This is used in the study to compare individual images to test repeatability of the discharge process. The sequential gating mode is used to study the time progression of the discharge. The sequential mode is set up by choosing the time delay to increase by a certain time. For example, the images

discussed in Section 4.3 are taken with a 10 ns step. An image is taken, then the delay is increased by 10 ns and a new image is taken continuing for a set number of times. Here each new image still corresponds to a new discharge process but the time during the pulse advances by 10 ns. This produces a sequence of images that correspond to different times during the discharge process.

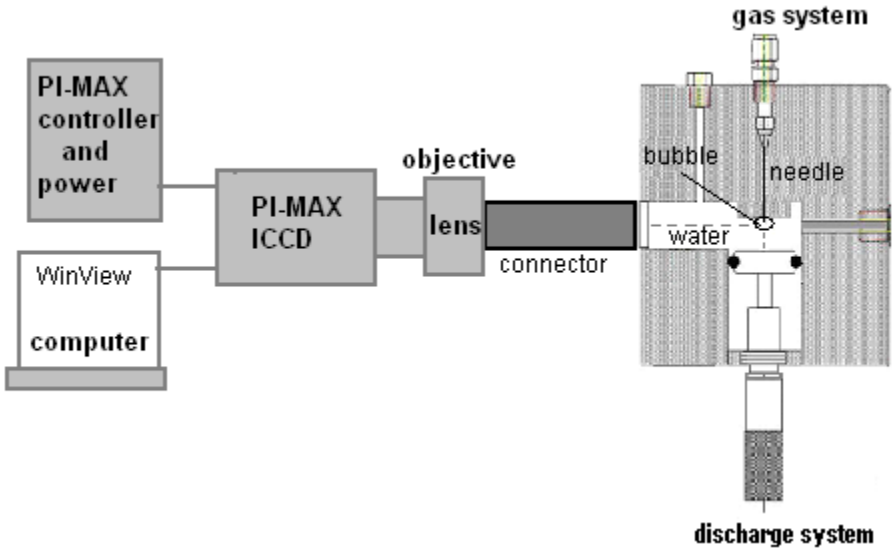

Figure 3.4.4. The figure shows the set-up used for imaging the discharge.

The use of the objective lens and the physical set up results in a spatial resolution of 0.125 mm per pixel. An average bubble discharge is imaged onto a region of about 80 x 80 pixels.

The optical set-up used in these experiments allows for high temporal resolution (~2 ns) in several 10 nm wide spectral regions using a Hamamatsu PMT with a set of band pass filters. Time resolved spectroscopy is also possible on a scale of about 100 ns with spectra recorded by the PI-MAX ICCD. The SPEX monochromator provides 0.15 nm spectral resolution and 40 nm wide spectral regions. Finally, the PI-MAX is also used

for imaging with a temporal resolution down to 5 ns and spatial resolution of 0.125 mm per pixel.

References:

1. Mozgina, O.; Gershman, S.; Belkind, A.; Becker, K.; Christodoulatos, C. Plasma Science, 2006. ICOPS 2006. IEEE Conference Record - Abstracts. The 33rd IEEE International Conference on, (2006), pp. 217 – 217
2. O. Mozgina, Pulsed Electrical Discharges in Bubbled Water for Environmental Applications, Ph.D. Thesis (2008) Stevens Institute of Technology.
3. Deepak K Gupta and P I John, (2001), S¯adhan¯a, Vol. 26, Part 5, October 2001, pp. 475–484.
4. I. Somerville, S. MacGregor, O. Farish (1990), *Meas. Sci. Technol.* 1: 865–868

4. The Investigation of the Discharge in Ar bubbles

4.1 Time-resolved Electrical Characteristics

The nature of an electrical discharge is uniquely expressed in its current-voltage characteristic.[1] Electrical discharges are classified based on the magnitude and temporal evolution of the current and voltage.[1, 2, 3] Due to the importance of the electrical information about the discharge, current and voltage oscillograms accompany all experiments in this study. The ability of these experiments to contribute new insight to the formation of electrical discharges in water is rooted in several advantages afforded by the experimental set-up and procedure used here. Single voltage pulses are applied allowing the data to be collected after each pulse and utilizing the full capability of the 5 GS/s sampling rate of the oscilloscope. The averaging feature of the oscilloscope is used to get a more general look at the impact of multiple pulses. The (essentially) rectangular shape of the voltage pulse is another advantage, since the displacement current is minimal. One drawback of using a pulse of this form is the need to deal with sizable electromagnetic interference (EI). This was done successfully by using a well-grounded Faraday cage described previously.

Experimental results are presented in the following order. First, typical oscillograms are presented and their general features are described. The first section also contains a description of the methods used to analyze the data. Next, a detailed analysis of the signal recorded during the first application of a voltage pulse to a freshly blown bubble. The dependence of the electrical characteristics on the applied voltage is

discussed here. The third section is devoted to the changes observed in repeated application of pulses to the same bubble (at a rate of 1 Hz). The remainder of the results for other conditions, such as the size of the bubble and the portion of the gap spanned by the bubble, are left for the last section.

4.1.1. Voltage and Current Oscillograms

All situations reported here involve a single bubble situated around the tip of a needle electrode protruding from an insulator and surrounded by water that also covers the submerged disk electrode. The typical current and optical emission pulses observed for voltages above a certain threshold are shown in Figure 4.1.1. The minimum voltage needed to generate the observed signal depends on the distance between the electrodes, the gas used in the bubble, and the conductivity and pH of the water. The Blumlein line pulse generator produces a voltage pulse that builds for about 150 ns, remains constant for close to 800 ns (except for a small oscillation in the signal inherent to this pulse shaping network) and then falls for about another 200 ns. The oscilloscope traces (Figures 4.1.1 and 4.1.2) show individual or a series of current and light emission pulses. There is no observable distortion of the voltage trace during these events. Two sets of peaks are generally observed, a set of peaks at various times during the application of the voltage pulse and another peak in both current and optical signal during the shut-off phase of the pulse. The amplitude, the number of peaks, and the time delay for the onset of the discharge depend on the applied voltage and on the size of the bubble. The optical emission signal (Fig. 4.1.1) was recorded using the 309 ± 5 nm filter (OH emission) and

shows optical pulses that are slightly broader than the corresponding current pulses. The light emission from these discharges has been studied intensively and will be discussed further in this work.

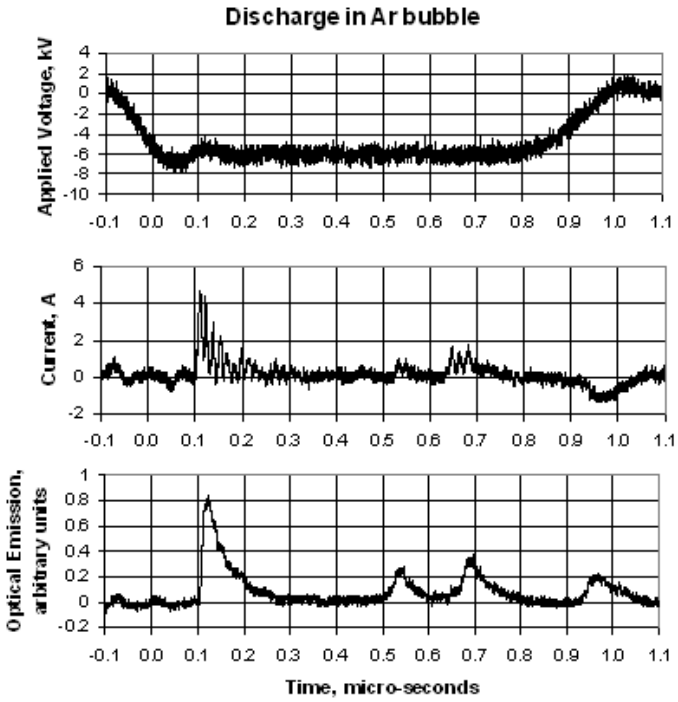

Figure 4.1.1. The figure shows voltage, current, and optical emission oscilloscope traces for a discharge in an Ar bubble. The current shown here was recorded prior to the construction of the Faraday cage.

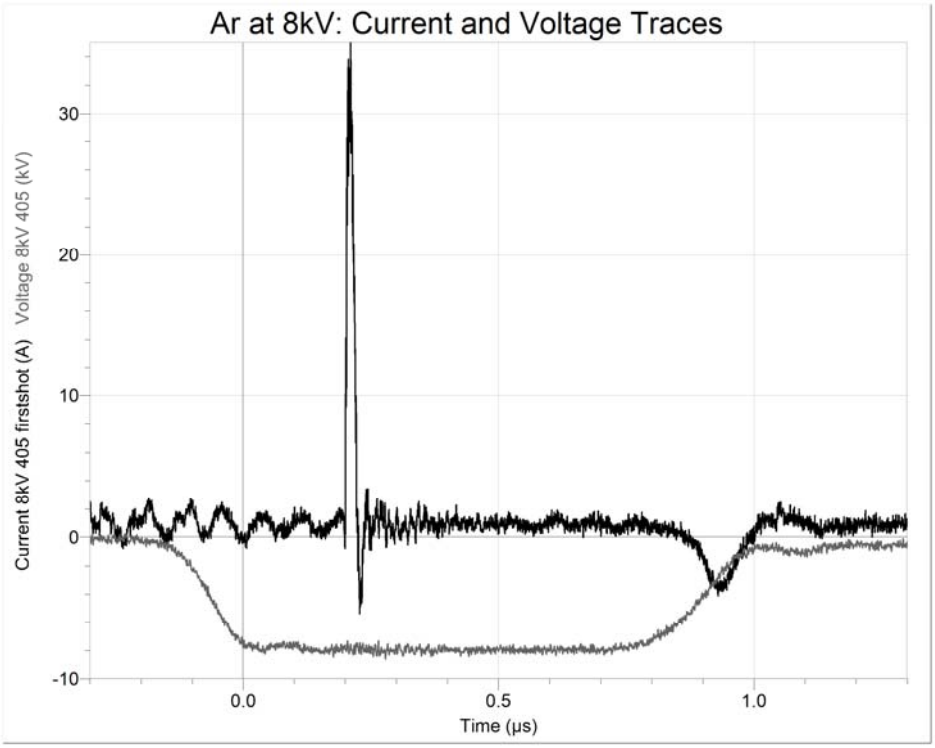

Figure 4.1.2. The current and voltage oscillograms for a discharge in Ar at 8 kV. The delay in the appearance of the current pulse is clearly visible here.

The fields present in the system and the currents measured are typical for a discharge in a high-pressure gas. The fields needed to ignite the discharge in water are of the order of 2 MV/cm (depending on the conductivity of the water). The highest fields in this system do not occur in the water, but in the gas in the immediate vicinity of the tip of the needle. Taking into account only the radius of the needle (0.3 mm for the 30 gauge hypodermic needle with a polished tip), the maximum values of the field are of the order of 10^4 – 10^5 V/cm. These values of the field exceed the breakdown field in Ar (2.7 kV/cm/atm), O_2 (30 kV/cm/atm), and air (32 kV/cm/atm), but are an order of magnitude (or more) below the breakdown field in water. The discharge process is observed within the gas bubble, and the study of the current trace is the first step in this investigation.

Work with short voltage pulses, under a microsecond in duration, is important for supplying information about the development of electrical discharges, but it also presents experimental challenges. Fig. 4.1.1 and 4.1.21 show the signals recorded before and after the construction of a Faraday cage and other circuit remediation measures. Before circuit redesign EI causes the signal to noise ratio approaching one, particularly in the case of the current and PMT signals. To reduce the EI, the geometry of the circuit is changed to eliminate unnecessary circuit loops and reduce stray capacitance. The quality of the physical ground was improved and a well-grounded Faraday enclosure was constructed encasing the pulse shaping network and the reactor. Double-shielded coaxial cables were used for all probes, and an isolation transformer was installed to prevent EI from being transmitted to the outlet ground. Although some current oscillations remained after these measures, the observed signal was much cleaner.

Application of a variable voltage pulse produces a current in the circuit that usually includes the displacement current due to the polarization charge on the electrodes and an additional component attributed to the discharge process. In this experiment, if the applied voltage is below the starting value for the discharge, no current is recorded at all, although it could be buried in the noise level. To insure an accurate interpretation of the recorded current signal, the displacement current is evaluated below.

The water chamber with a single gas bubble (See Fig.3.2.1 in the experimental section) on a needle may be approximated by a series combination of two capacitors, the bubble C_b and the water C_w. The bubble capacitance is estimated as that of a gas filled spherical capacitor with the inner electrode (0.3 mm tip of the needle) much smaller than the 2 – 8 mm diameter of the bubble. Under these assumptions, the capacitance of the

bubble is of the order of about 0.1 pF, at least two orders of magnitude lower than the capacitance of the water gap. The voltage measured across the system (V_{appl}) is the sum of the voltages across the water and bubble,

$$V(t)_{appl} = V_{water} + V_{bubble} \tag{4.1.1}$$

For a given applied potential, most of the voltage drop is across the bubble since

$$C_{bubble} << C_{water}. \tag{4.1.2}$$

It was shown[2, 4] that in similar arrangements

$$i(t)_{disch} = \left(1 + \frac{C_{gas}}{C_{dielectric}}\right) \cdot \left(i(t)_{meas} - C_{equivalent} \cdot \frac{dV(t)_{appl}}{dt}\right) \tag{4.1.3}$$

where $i_{discharge}$ is the current due to the discharge in the bubble, i_{meas} is the current measured by the coil, V_{appl} is the applied voltage, and $C_{equivalent}$ is the equivalent capacitance of the combined gas-dielectric circuit. For the discharge in the bubble, C_{gas}= C_{bubble} and $C_{dielectric}$= C_{water}, and so the above expression becomes

$$i(t)_{disch} = \frac{C_{bubble}}{C_{equiv}} \cdot i(t)_{meas} - C_{bubble} \cdot \frac{dV(t)_{appl}}{dt} \tag{4.1.4}$$

Figure 4.1.3 compares the measured current, the calculated displacement component of the current, and the displacement current. Due to the low values of the capacitance, the displacement component of the current is much lower than the measured current. Since $C_w >> C_b$, the equivalent capacitance C is approximately equal to C_b and the ratio C_b/C is close to 1. It can be seen from the expression above that the measured current closely matches the discharge current.

4.1.2. **First Current Pulse Analysis**

4.1.2.1. Main features of the current trace in one pulse

A voltage pulse applied to a new Ar bubble produces no observable current for voltages below a certain minimum value. The minimum value depends on the size of the bubble and on the distance between the negative needle electrode and the positive disk electrode. The size of the bubble (8 +/- 1mm in diameter) and the distance between the electrodes (15 mm) remain constant for all results reported below. For these parameter values, the minimum voltage to start the discharge in an Ar bubble is 7.5+/-0.4 kV. To obtain a discharge consistently every time a pulse is applied, 8 kV is the lowest voltage used in the experiments reported below.

A sharp current pulse appears with a random delay (Figure 4.1.4. a) relative to the time the voltage reaches the applied 8 kV. Delays of up to 700 ns have been observed. As the applied voltage increases, the current appears sooner (relative to the part where the voltage reaches a plateau) and the magnitude of the peak increases. Experiments are repeated multiple times for each voltage and the results of the current trace analyses are given in Tables 4.1.1 and 4.1.2.

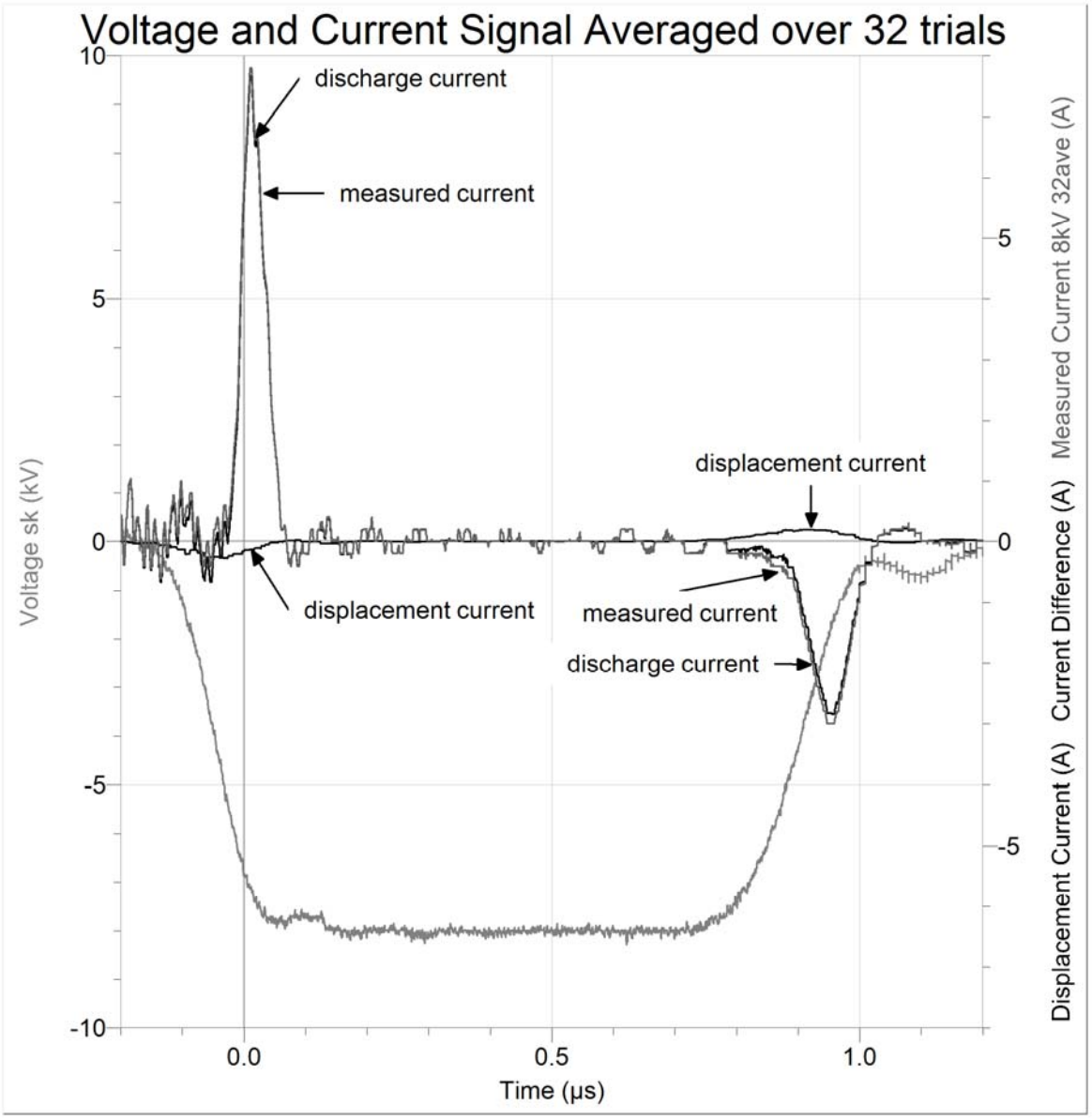

Figure 4.1.3. The graph shows the calculated displacement current, the total measured current, and the difference between the two, the discharge current. It can be seen that the measured current is very close to the discharge current.

(a)

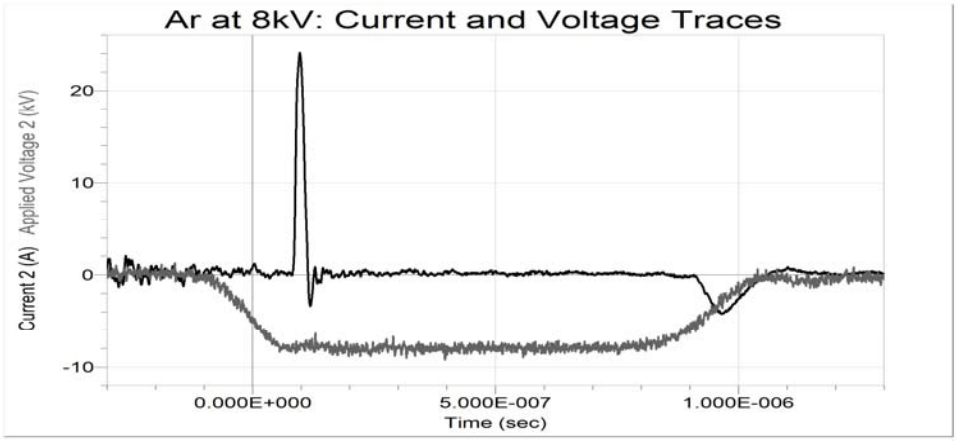
Ar at 8kV: Current and Voltage Traces
Current 2 (A) Applied Voltage 2 (kV)
20
10
0
-10
0.000E+000
5.000E-007
1.000E-006
Time (sec)

(b)

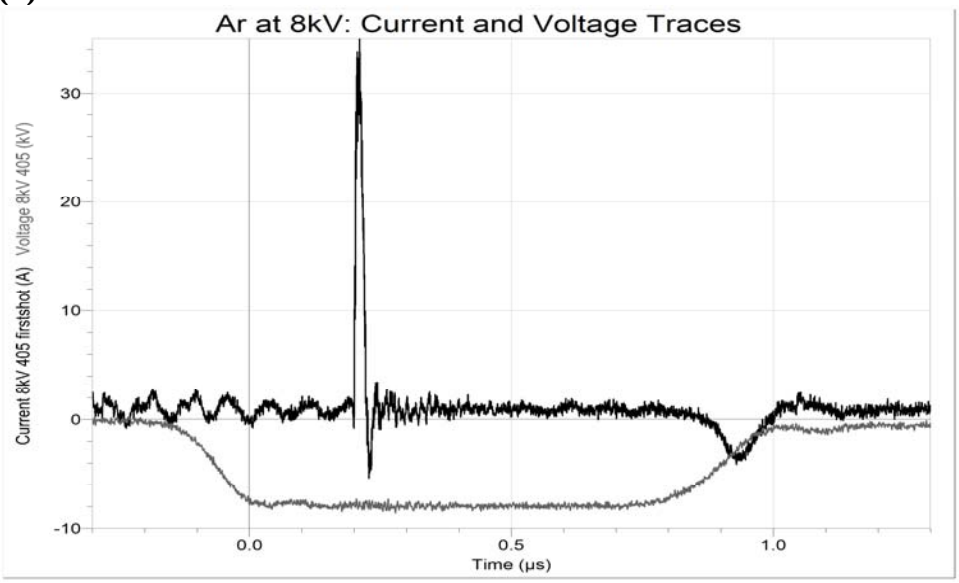
Ar at 8kV: Current and Voltage Traces
Current 8kV 405 firstshot (A) Voltage 8kV 405 (kV)
30
20
10
0
-10
0.0
0.5
1.0
Time (µs)

(c)

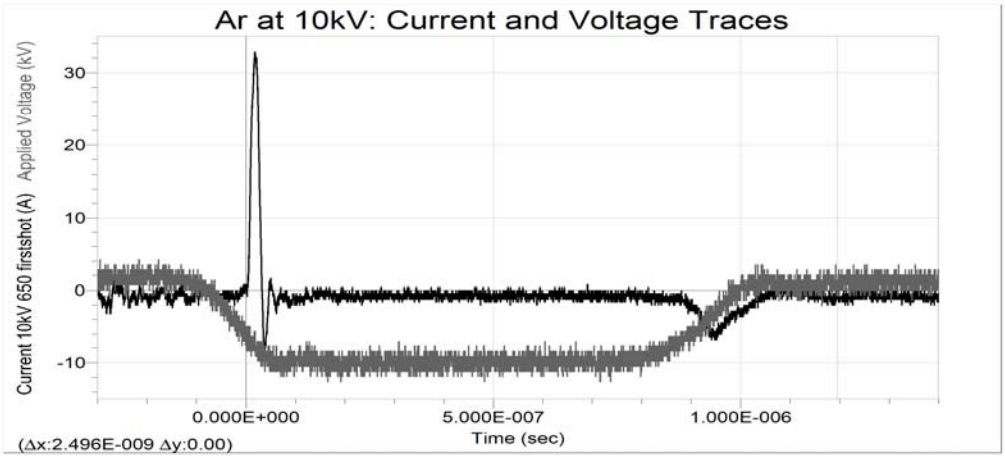
Ar at 10kV: Current and Voltage Traces
Current 10kV 650 firstshot (A) Applied Voltage (kV)
30
20
10
0
-10
0.000E+000
5.000E-007
1.000E-006
Time (sec)
(Δx:2.496E-009 Δy:0.00)

(d)

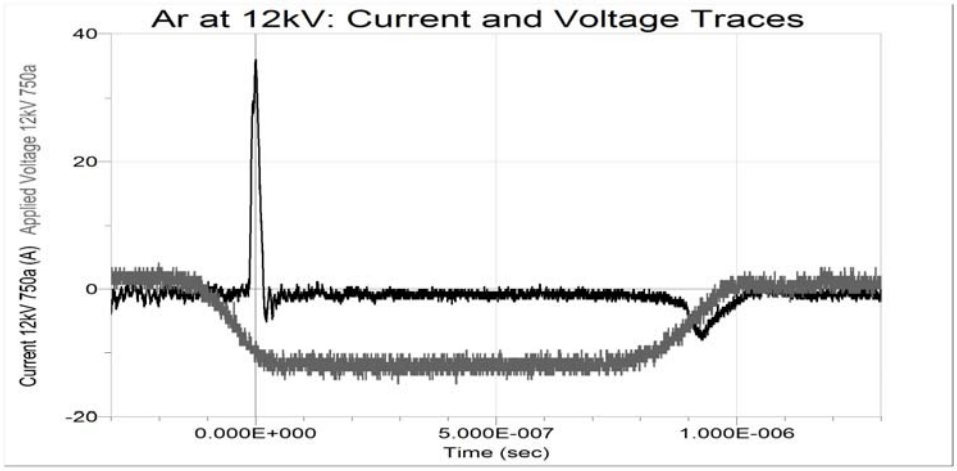

(e)

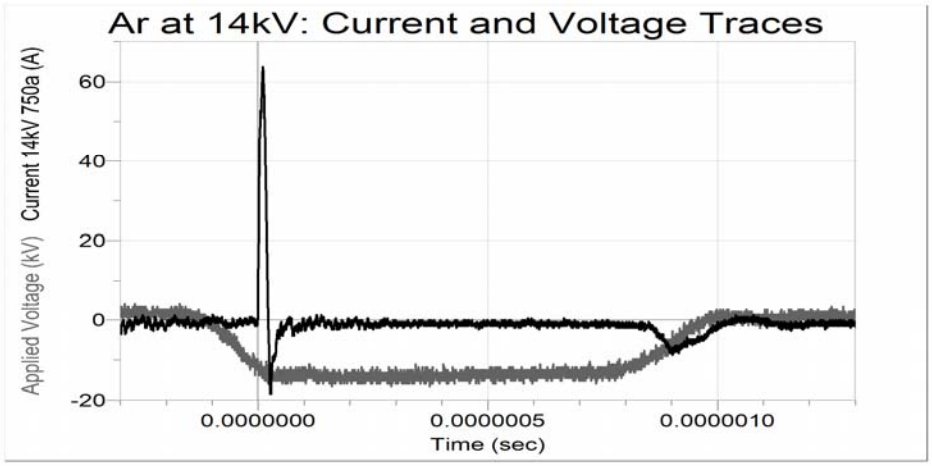

(f)

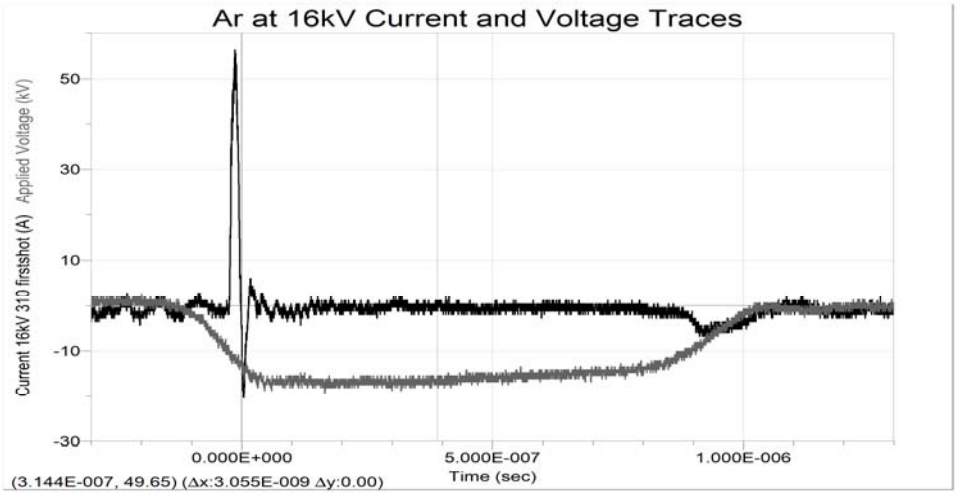

Figure 4.1.4. Current and voltage oscilloscope traces for various applied voltages

Table 4.1.1 Data analysis of the current trace for the first voltage pulse applied to a new Ar bubble.

Data Analysis for a first voltage pulse applied to a new Ar bubble											
Repeated Trials	Applied Voltage, kV	Width of first current peak, ns	Max Current for first peak, A	Max Current for last peak, A	Rate of current rise, first peak: dI/dt, A/s	Rate of current fall, first peak: dI/dt, A/s	Charge transferred (integral of first peak), C	Charge transferred (integral of last peak), C	Mean Current between peaks, A	Noise level (current with voltage off), A	Current Mean over one pulse, A
	8	18.40	24.20	-4.40	2.745E+09	-1.7E+09	4.2713E-07	3.3949E-07	0.1464	0.1636	0.2264
	8	18.00	38.00	-8.40	3.075E+09	-2.99E+09	6.447E-07	6.44E-07	0.3416	0.2541	0.2698
	8	20.40	23.20	-4.96	2.081E+09	-1.66E+09	4.643E-07	3.6267E-07	0.04664	0.0618	0.1214
AVERAGE	8	18.93	28.47	-5.92	2.634E+09	-2.12E+09	5.1204E-07	4.4872E-07			
ST DEV		1.29	8.27	2.17	506135321	756180589	1.1638E-07	1.6951E-07			
	10	15.00	35.80	-4.60	3.393E+09	-2.27E+09	4.659E-07	3.853E-07	0.9231	0.8731	0.9746
	10	18.20	32.80	-6.80	2.503E+09	-2.78E+09	5.648E-07	6.0155E-07	0.7187	0.7546	0.648
	10	14.40	48.40	-5.60	4.505E+09	-4.95E+09	6.403E-07	5.587E-07	0.8387	0.8191	0.923
	10	17.00	36.80	-6.80	3.069E+09	-3E+09	5.769E-07	5.8331E-07	-0.7605	-0.7757	-0.6931
AVERAGE	10	16.15	38.45	-5.95	3.367E+09	-3.25E+09	5.6198E-07	5.3222E-07			
ST DEV		1.76	6.85	1.06	842638592	1.175E+09	7.2102E-08	9.9505E-08			
	12	17.00	36.00	-8.00	2.639E+09	-2.15E+09	5.981E-07	6.051E-07	-0.8246	-0.8253	-0.738
	12	18.40	41.20	-7.20	3.032E+09	-3.06E+09	7.072E-07	7.0688E-07	-0.6693	-0.8174	-0.6532
	12	14.80	60.40	-7.20	5.584E+09	-5.57E+09	8.5856E-07	9.385E-07	0.08603	-0.8698	-0.3141
	12	14.60	68.80	-8.00	6.854E+09	-6.85E+09	9.5139E-07	9.922E-07	0.07033	-0.7219	-0.2538
	12	16.40	46.00	-7.60	4.226E+09	-4.36E+09	7.565E-07	8.998E-07	-3.406	-1.727	-1.524
AVERAGE	12	16.24	50.48	-7.60	4.467E+09	-4.4E+09	7.7435E-07	8.285E-07			
ST DEV		1.58	13.69	0.40	1.761E+09	1.887E+09	1.3631E-07	1.6483E-07			
	14	15.00	63.60	-8.80	6.628E+09	-6.09E+09	8.976E-07	8.537E-07	-0.9955	-1.043	-0.8493
	14	21.40	31.60	-7.20	2.016E+09	-2.15E+09	6.58E-07	6.418E-07	-0.93	-1.109	-0.9368
	14	17.00	46.80	-6.80	3.344E+09	-3.96E+09	7.838E-07	8.2062E-07	-0.5609	-0.7611	-0.6062
AVERAGE	14	17.80	47.33	-7.60	3.996E+09	-4.07E+09	7.798E-07	7.7204E-07			
ST DEV		3.27	16.01	1.06	2.374E+09	1.973E+09	1.1985E-07	1.14E-07			
	16	16.00	56.40	-6.80	4.93E+09	-5.41E+09	7.9572E-07	8.0592E-07	-0.5077	-0.9333	-0.4942
	16	16.00	91.00	-15.00	8.988E+09	-8.79E+09	1.2313E-06	1.4409E-06	-1.932	-1.921	-1.807
	16	15.60	60.00	-8.00	6.111E+09	-5.45E+09	8.7273E-07	9.325E-07	-0.9377	-0.958	-0.8715
	16	20.00	47.60	-7.60	3.998E+09	-3.15E+09	8.835E-07	8.3994E-07	-0.507	-0.7596	-0.5217
AVERAGE	16	16.90	63.75	-9.35	6.007E+09	-5.7E+09	9.4582E-07	1.0048E-06			
ST DEV		2.08	18.90	3.80	2.167E+09	2.323E+09	1.9431E-07	2.956E-07			

Table 4.1.2 Statistical analysis of the current pulse

Statistical Mean Current in each Pulse					
Repeated Trials	Applied Voltage, kV	Noise level (current with voltage off), A	Current Mean over one pulse, A	Mean Current as percent of last peak current, %	Noise as percent of last peak current, %
	8	0.16	0.23	5.15	3.72
	8	0.25	0.27	3.21	3.03
	8	0.06	0.12	2.45	1.25
AVERAGE	8	0.16	0.21	**3.60**	**2.66**
ST DEV		0.10	0.08	1.39	1.28
	10	0.87	0.97	21.19	18.98
	10	0.75	0.65	9.53	11.10
	10	0.82	0.92	16.48	14.63
	10	-0.78	-0.69	10.19	11.41
AVERAGE	10	0.42	0.46	**14.35**	**14.03**
ST DEV		0.80	0.78	5.53	3.67
	12	-0.83	-0.74	9.23	10.32
	12	-0.82	-0.65	9.07	11.35
	12	-0.87	-0.31	4.36	12.08
	12	-0.72	-0.25	3.17	9.02
	12	-1.73	-1.52	20.05	22.72
AVERAGE	12	-0.99	-0.70	**9.18**	**13.10**
ST DEV		0.41	0.51	6.66	5.50
	14	-1.04	-0.85	9.65	11.85
	14	-1.11	-0.94	13.01	15.40
	14	-0.76	-0.61	8.91	11.19
AVERAGE	14	-0.97	-0.80	**10.53**	**12.82**
ST DEV		0.18	0.17	2.18	2.26
	16	-0.93	-0.49	7.27	13.73
	16	-1.92	-1.81	12.05	12.81
	16	-0.96	-0.87	10.89	11.98
	16	-0.76	-0.52	6.86	9.99
AVERAGE	16	-1.14	-0.92	**9.27**	**12.13**
ST DEV		0.53	0.61	2.59	1.59

The current traces always include two main current peaks, a sharp peak in one direction and a peak in the opposite direction that occurs once the voltage has dropped below a certain value. The first current peak is also often accompanied by an "overshoot" into the opposite direction that appears as a quickly diminishing oscillation of the current. The first current peak rises quickly with an average rise time in the range of 5 – 10 ns and falls slightly slower taking about 10 – 15 ns. The measured current is not accompanied by any detectable change in the voltage trace (measured over the bubble – water combination). The current rise time is faster than the time needed for an electron to travel across the bubble from the needle to the opposite side given the typical electron mobility of 4.34 (cm/s)/(V/m) in Ar at atmospheric pressure.

The current is at or below the noise level for the remainder of the pulse between the two peaks. In Table 4.1.1 the mean current over the time period between the pulses is compared to the noise level in the signal. The noise level is evaluated by calculating the average signal present when the voltage difference between the electrodes is zero. The noise is usually at about 13% of the maximum current in the second peak and the mean current between the peaks is at about 12% of the same.

A significant feature of the current signature is the essentially zero value obtained when the current is averaged over the duration of the entire voltage pulse. Table 4.1.2 shows that the statistical mean of the current over the duration of the pulse is again at or below the noise level. This means that there is no net total charge transfer between the electrodes. The time integral of the first current peak gives the amount of charge transferred by this peak, and likewise the time integral of the last peak gives the amount of charge transferred in the opposite direction. The data in Table 4.1.3 show that these

two values are closely matched in some trials but not in all. A closer match is achieved if some corrections are made taking into account, for example the sharp peak in the opposite direction following the first high current peak (Figure 4.1.4f). The statistical mean over the entire duration of the pulse takes detailed account of all current variations and provides a more reliable assessment of the charge transfer balance. The data indicate therefore, zero charge transfer over the time of the pulse.

4.1.2.2. Changes in the electrical characteristics with varying applied voltage

The first noticeable change in the current trace with increasing voltage is the increase in maximum current. More careful examination reveals seemingly random variations in the maximum value of the current. Since the size of the bubble remains constant only within a millimeter in diameter, this may be a variable affecting the current. The discussion of this or other possibilities is reserved for the discussion (Section 4.5). A plot of the maximum current as a function of voltage (Fig. 4.1.5) an increase in the maximum current with increasing voltage. The correlation coefficient of the linear fit shown in Fig. 4.1.5 is 0.66. The correlation coefficient is affected by the spread in the peak current values. Figure 4.16 shows the transferred charge (the integral of the current peak) as a function of the applied voltage. The correlation coefficient for the linear fit for this relationsip is 0.77 (Fig. 4.1.6). The plot of the charge transferred in each direction does provide a clear visual presentation of the charge balance during discharge (discussed above) as the points corresponding to the values of the transferred charge almost overlap with each other.

Table 4.1.3. The summary of the current trace analysis for the first voltage pulse applied to a new Ar bubble.

Summary data for a first voltage pulse applied to a new Ar bubble										
Applied Voltage, kV	Width of first current peak, ns	Max Current for first peak, A	Max Current for last peak, A	Rate of current rise, first peak: dI/dt, x10^9 A/s	Rate of current fall, first peak: dI/dt, x10^9 A/s	Charge transferred (integral of first peak), x10^-7 C	Charge transferred (integral of last peak), x10^-7 C	Mean Current between peaks as a percent of last peak, %	Mean Current as percent of last peak current, %	Noise as percent of last peak current, %
8	18.93	28.47	-5.92	2.63	2.12	5.12	4.49	2.78	3.60	2.66
10	16.15	38.45	-5.95	3.37	3.25	5.62	5.32	14.20	14.35	14.03
12	16.24	50.48	-7.6	4.47	4.4	7.74	9.29	13.30	9.18	13.10
14	17.8	47.33	-7.6	4	4.07	7.8	7.72	10.83	10.53	12.82
16	16.9	63.75	-9.35	6	5.7	9.46	10.05	9.68	9.27	12.13

Visual examination of the first current peak at different voltages shows that as the maximum value increases (albeit weakly) the width of the peak does not (Figure 4.1.7) as it would if the rate of the current rise remained constant. The width remains independent of the applied voltage (Figure 4.1.7). The rate of the current change does increase with the increase in the charge transferred by the peak. (Figure 4.1.8) The data indicate that the greater the amount of charge build up, the faster the process of build up occurs. This is an interesting result and it will be discussed further from the point of view of the mechanisms of the discharge development.

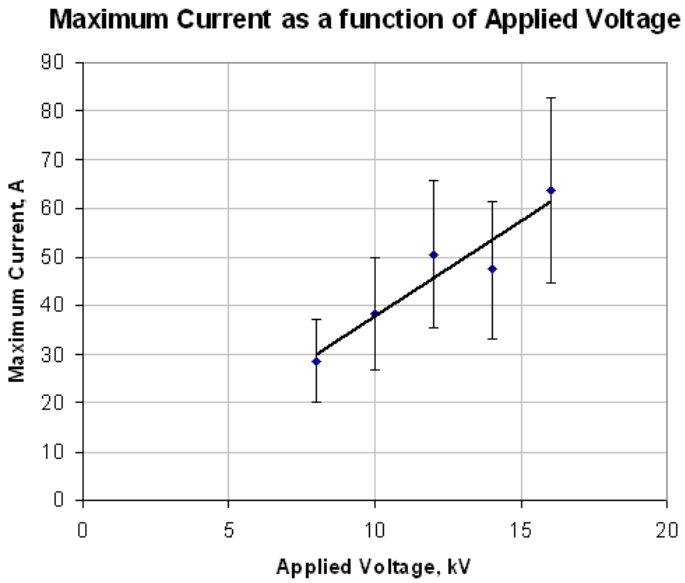

Figure 4.1.5. Maximum current in each pulse is shown as a function of applied voltage

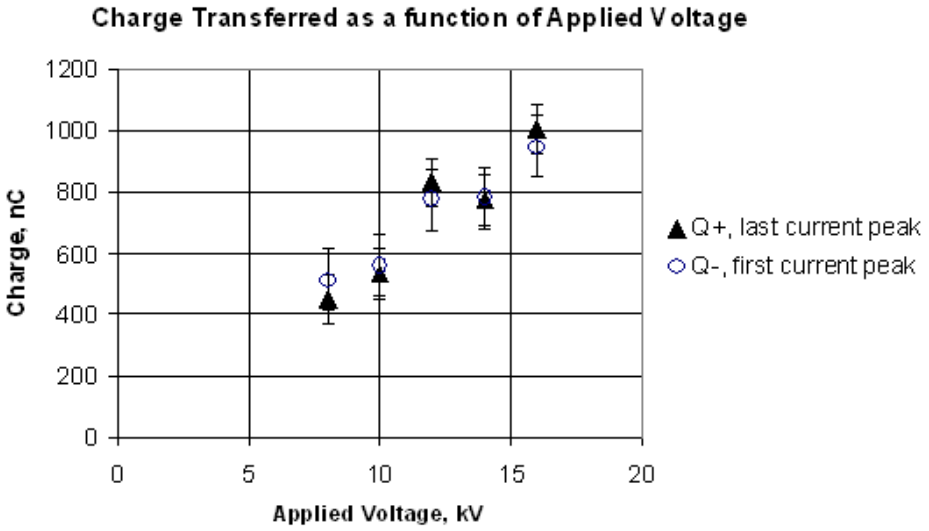

Figure 4.1.6. Charge transferred to the wall of the bubble is calculated as the integral of the first current pulse (open circles) and last peak (triangles) and plotted here versus the applied voltage.

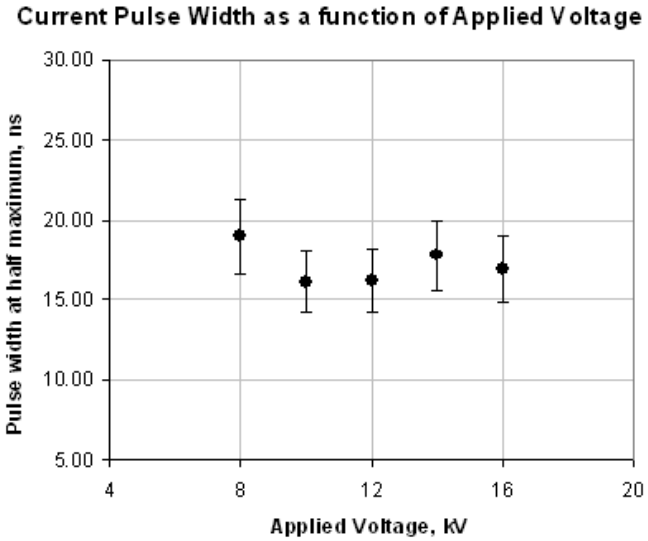

Figure 4.1.7. Width at half maximum of the first current pulse as a function of applied voltage.

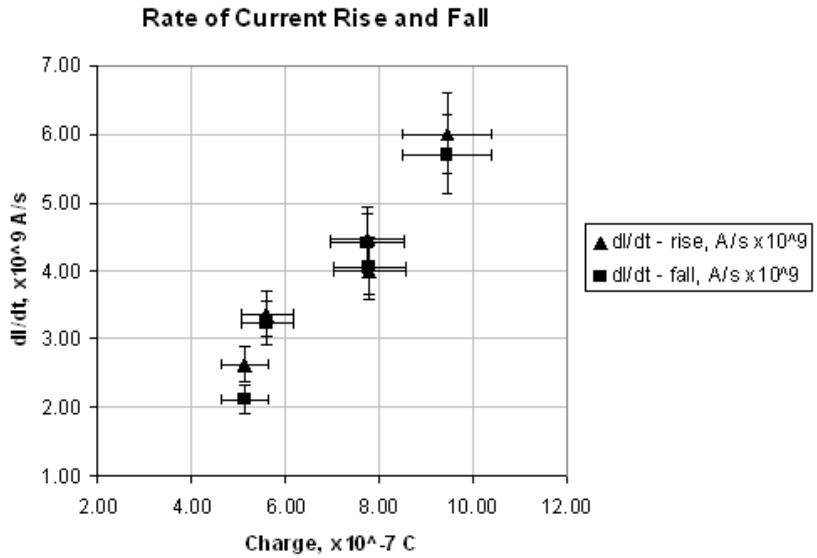

Figure 4.1.8. Rate of current increase and decrease for the first current pulse as a function of the transferred charge.

4.1.3. The effect of pulse repetition on the electrical characteristics

A voltage pulse applied to any single bubble studied here causes a visible bright streamer, an audible sound, and visible mechanical oscillations of the bubble. The bubble remains in place and intact after each pulse. This section describes the effect of the repeated application of voltage pulses, or shots of the same magnitude to a single Ar bubble that remains in place throughout the entire ordeal. The pulses are applied at a rate of 1 Hz and the oscillograms are recorded for every shot for the first 10 shots, after every 5 shots for the first 50 shots, and every 50 shots thereafter. The pulse rate of 1 Hz is low enough so that each discharge process is expected to be unique and not affected by the previous discharge process. The oscillograms for shots number 1, 5, 50, and 150 are shown in Figure 4.1.9.

The most apparent change is in the amplitude of the first peak (Figure 4.1.10). Comparing the oscillograms of the first and fifth shot, it can be seen that the magnitude of the first current peak decreases down to about 60% of its value in the first shot. By the 100^{th} shot the magnitude of the first peak is only 25% of the original value. Two other significant changes accompany the decrease in current magnitude. The first is the increase in the width of the pulse and the second is the appearance of a sizeable current throughout the duration of the voltage pulse. (Table 4.1.4) Here it also makes sense to compare the mean current and the current after the first peak to the noise level in the experiment. The current measured while the voltage pulse is off remains at a fairly high 18% of the second current peak, on average. In contrast, the mean current over the duration of the pulse changes from being at the noise level initially (~18%) to almost matching the current value in the second peak. The charge balance over the duration of the pulse is not maintained and a continuous current is observed. The overall appearance of the current trace is that of flattening peaks and an increasing continuous component of the current.

Repeating similar experiments for an even greater number of shots gives an appearance of saturation. The current traces change drastically at the beginning of the experiment but seem to settle into a pattern for over 100 shots. (Figure 4.1.11)

Comparing the traces for the first peaks in Fig. 4.1.10 and in Fig. 4.1.11 shows the randomness in the timing of the first peak disappears after the first few shots. With continued repetition, the peaks shift to an earlier time and settle into a consistent time.

The inherent degree of randomness in each discharge process makes it difficult to determine at what time the changes in the bubbles become significant enough to affect

the consequent discharge processes (assuming that is what is occurring). After the first few shots are recorded, the next 32 shots are collected and averaged by the scope. This means that the information for shots #5 – 35 is contained in the averaged traces. It is clear from Figs. 4.1.11 and 4.1.12 that the current traces still preserve the characteristics of the first few shots. The traces have decreased in magnitude (compare the Figs. 4.1.12 and 4.1.4f for the average and the first shot at 16kV), but not broadened significantly, and the mean current is still zero. The result of averaging a signal that has some variation in the starting time is a broader current peak. This artificial broadening precludes any meaningful interpretation of the peak width calculations. The averaging also lowers the mean current values both between the peaks and over the entire pulse.

The data indicate that changes in the current trace, such as reduction in the peak values, wider peaks, and an increase in the average current begin to reach significant proportions after 50 – 100 shots. Since the frequency of the shots is 1 Hz, 50 – 100 shots mean 50 – 100 μs of voltage ON time and 50 – 100 seconds overall bubble treatment time. These considerations are important since chemical processes continue after the voltage is turned off.

(a)

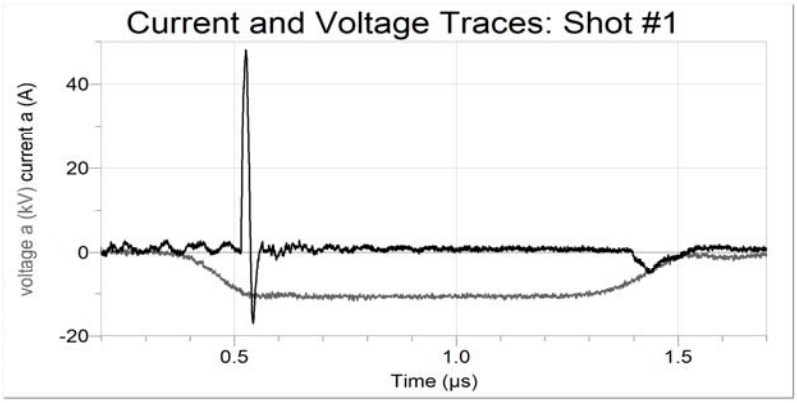

(b)

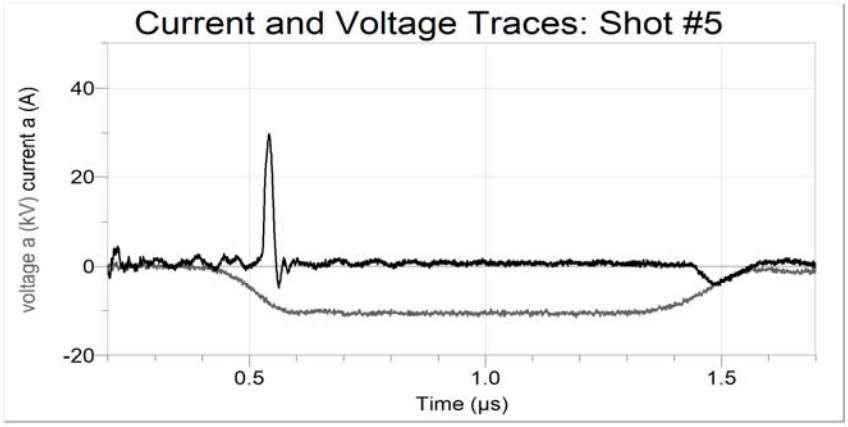

(c)

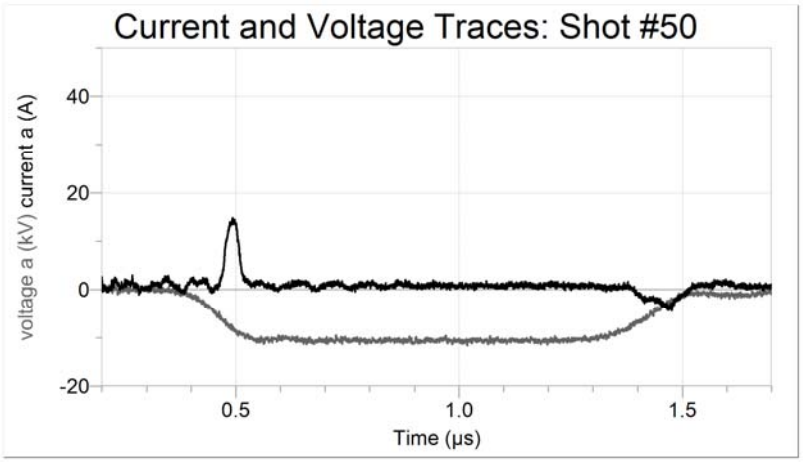

(d)

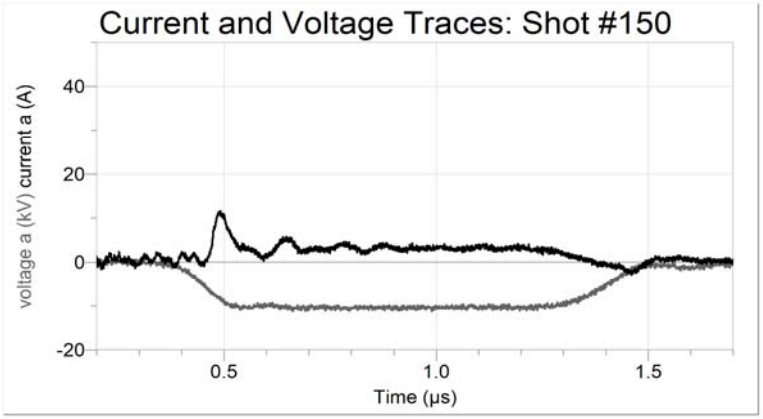

Figure 4.1.9. The oscilloscope traces shown in figures a – d correspond to discharges in the same Ar bubble subjected to voltage pulses at a rate of 1 Hz. The shot # for each discharge is given in the figure. The applied voltage is 10 kV.

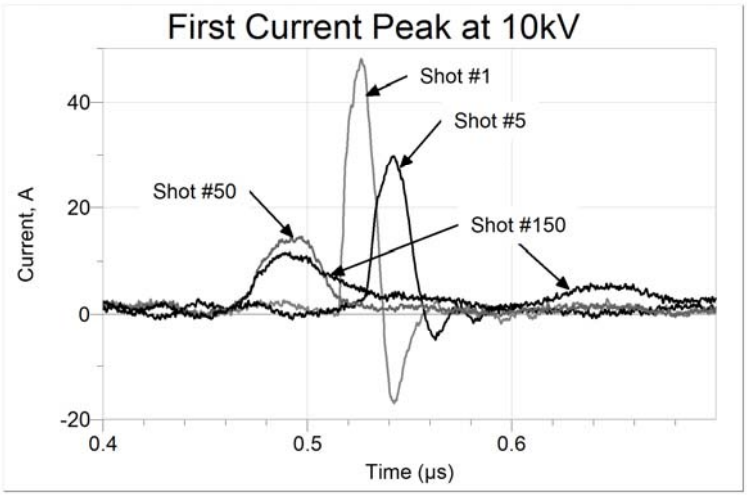

Figure 4.1.10. This figure gives a closer look at the first current peaks in each of the oscillograms in figure 4.1.9.

Table 4.1.4. Data for the discharges in the same Ar bubble with repeated shots. 10 kV pulses are applied at a rate of 1 Hz.

Data for repeated 10kV shots for the same Ar bubble									
Shot #	Width of first current peak, ns	Max Current for first peak, A	Time for maximum current, ns	Max Current for last peak, A	Charge transferred (integral of first peak), x10^-7 C	Charge transferred (integral of last peak), x10^-7 C	Mean Current between peaks as a percent of last peak, %	Mean Current as percent of last peak current, %	Noise as percent of last peak current, %
1	15	48.04	526	-5.18	6.587	1.406	16.6	18.0	16.6
5	20	29.83	542	-4.4	5.17	0.77	17.1	19.0	21.7
50	33	14.76	492	-4.324	5.106	2.004	20.2	22.0	19.6
150	44	11.62	491	-2.895	6.713	1.174	**110.3**	**79.9**	15.6

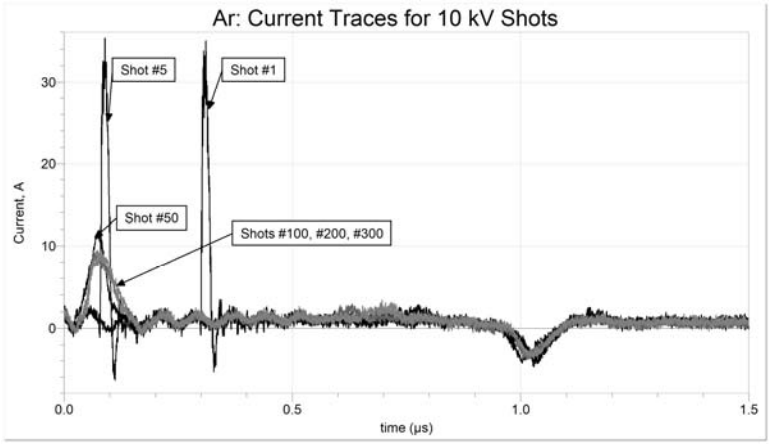

Figure 4.1.11. Comparing later shots (#100 – 300) and the earlier shots

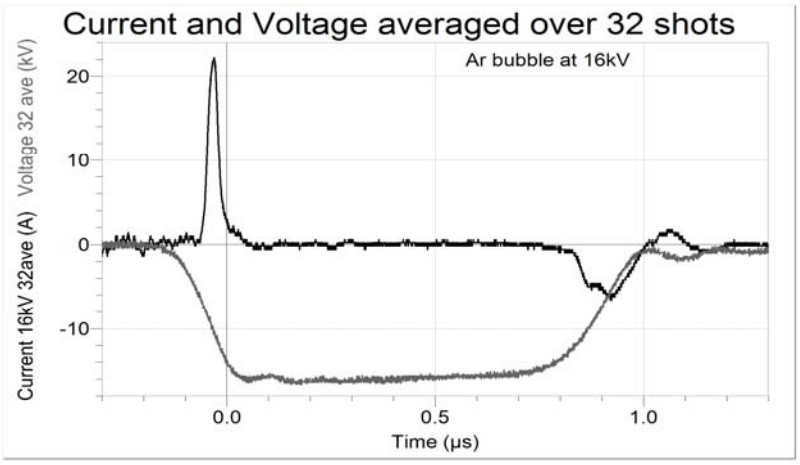

Figure 4.1.12. This figure shows the current and voltage traces averaged by the oscilloscope over 32 applied pulses.

4.1.4. Bubble Size Experiments

At a fixed distance between the electrodes and for the same voltage, measurements reveal a dependence of the discharge characteristics on the size of the bubble. Figure 4.1.13 shows the optical emissions produced by the discharge at 5 kV in bubbles of three different sizes. The trace for the 2 mm bubbles shows only the initial peak and a small magnitude peak during the voltage shut-off stage. In bigger bubbles repeated peaks are evident, with the greater number of peaks corresponding to bigger bubbles. The intensity of the last peak increases with the size of the bubble. This increase in the number of emission peaks in larger bubbles is the first piece of evidence that hints at the importance of the surface of the bubble for the formation and development of the discharge.

References:

1. K. H. Becker, U. Kogenlschatz, K. H. Schoenbach, R. J. Barker, (2005), *Non-Equilibrium Plasmas at Atmospheric Pressure*, IoP Publishing, Bristol and Philadelphia
2. N. Jidenko, M. Petit, J. P. Borra, (2006), **J. Phys. D: Appl. Phys.** Vol. 39, pp. 281–293
3. R. Hippler, S. Pfau, M. Schmidt, K. H. Schoenbach, (2001), *Low Temperature Plasma Physics*, Wiley_VCH, Berlin
4. H. Raether, (1964), *Electron Avalanche and Breakdown in Gases* (London: Butterworths)

4.2. Emission decay rates in various spectral regions

This section is devoted to the temporal evolution of the optical emissions from an Ar bubble during the discharge. A large bubble, approximately 8 mm in diameter is used in all experiments since extra brightness is needed for optical measurements. Ar bubble emission was recorded with a PMT using several band filters with a band width of 10 nm and center wavelengths of 310 nm, 750 nm, 760 nm, 777 nm, 810 nm, and 840 nm. The discharge, each in a single Ar bubble, was produced by applying 1 μs long voltage pulses of 8 kV, 10 kV, 12 kV, 14 kV, 16 kV, and 18 kV at the flat top portion of the signal. The data discussed here are organized by the filter wavelength first and then within each wavelength section, it is separated by the applied voltage. To assess both the repeatability of the data and the effect of the impurities on the light emitted and the current, each measurement was repeated approximately 100 times. The first three to five trials are recorded individually, then 32, and finally 156 trials are averaged. Figure 4.2.1 shows a

typical oscillogram taken during the first pulse applied to a new bubble. As discussed in the previous section, the shape of the current signal changes after the first few repeated pulses are applied to the same bubble (Figure 4.2.2). The temporal development of the current pulses is important in the analysis of optical emission data.

The oscillograms show the PMT signal leading the current signal by 10 +/- 0.5 ns consistently for all trials and all voltages in all optical ranges tested. Similarly, the optical emission peaks 15 +/-5 ns ahead of the current. These time delays cannot be viewed as caused by the discharge processes, since they are at the level of the time resolution of the apparatus. The response time of the Hamamatsu PMT is slightly (~5 ns) faster than the Pearson current coil. In addition, the 10 ns shift between the two signals is a result of the cable length mismatch. The cables connecting the current probe to the scope are 9 feet long and the combined length of the optical fiber (4') and the oscilloscope cables (2') is 6 feet, so the difference coincides with the distance traveled by the signal in 10 ns.

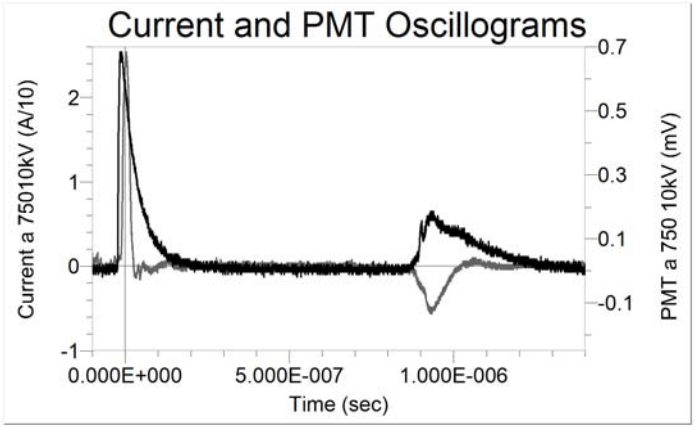

Figure 4.2.1 A sample oscillogram showing the current and PMT traces for the discharge in Ar bubble at 10 kV. A 750 +/-10 nm filter is used on the PMT. This is a typical example for one of the first few pulses applied to a new bubble.

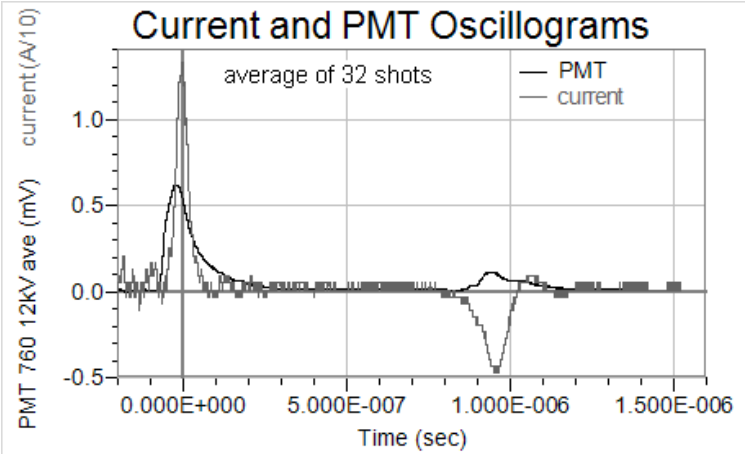

Figure 4.2.2 A sample oscillogram showing the current and PMT traces for the discharge in Ar bubble at 12 kV. A 760 +/-10 nm filter is used on the PMT. Thirty two (32) shots with a pulse frequency of 1 Hz have been averaged by the oscilloscope. This is a typical example of an oscillogram after multiple repetitions of pulses have been applied to the same bubble.

4.2.1. Investigation of Ar lines regions 750, 760, and 810 nm

The Ar optical emission signal (in the ranges of 750 nm, 760 nm, and 810 nm) rises very sharply, but does not decay at the same rate as the current. The optical emission decays slower and continues after the current diminishes. The oscillograms clearly show variations in the optical signal while the current is present. An attempt was made to fit exponential decay curves to the first part of the optical decay curve, before the current reached zero. This analysis generated decay rates much shorter than those after the current was diminished. Inconsistencies in the PMT signal make this fitting process difficult and not clearly justified.

Once the current diminishes, it is possible to fit one exponential decay curve to the signal with a RMSE better than 1%. The decay constants for optical emission signals

are then calculated from the parameter of the exponential decay curve fitted to the PMT signal in the region after the current diminishes. Each single shot trial is analyzed several times to determine the possible spread of parameter values. The actual values for the decay constants obtained in this manner depend strongly (+/-25%) on the actual choice of the time interval used for curve fitting, but the trends (discussed below) hold. Although the current pulse changes shape and magnitude during repeated pulsing, as described in the previous section, the optical emission decay rates are independent of the number of repetitions (See Figure 4.2.3). This has been confirmed for up to 50 repetitions. The decay of optical emission in the examined wavelength regions does not change (within experimental error), but the change in current slows.

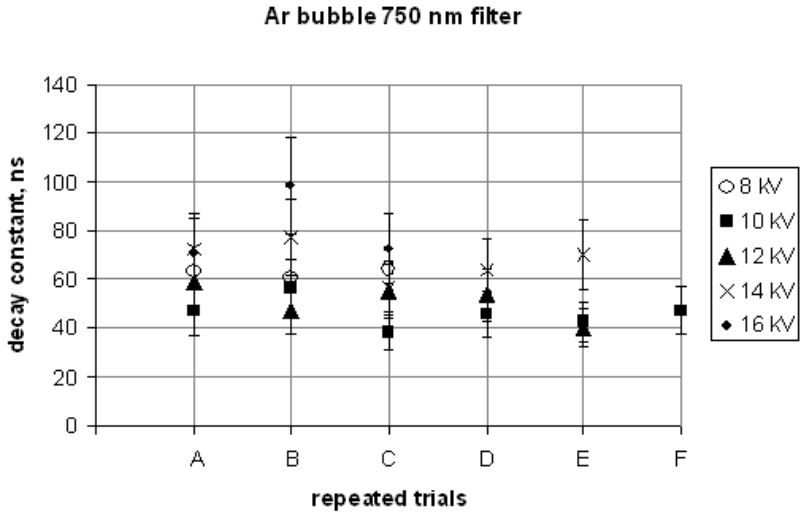

Figure 4.2.3 Decay constants for optical emission measured with the 750 nm filter the first time a voltage pulse is applied to a new bubble. Decay constants are plotted versus the order of the shot applied to the same bubble for shots A – F where A is shot #1. Results are shown for a series of different voltages.

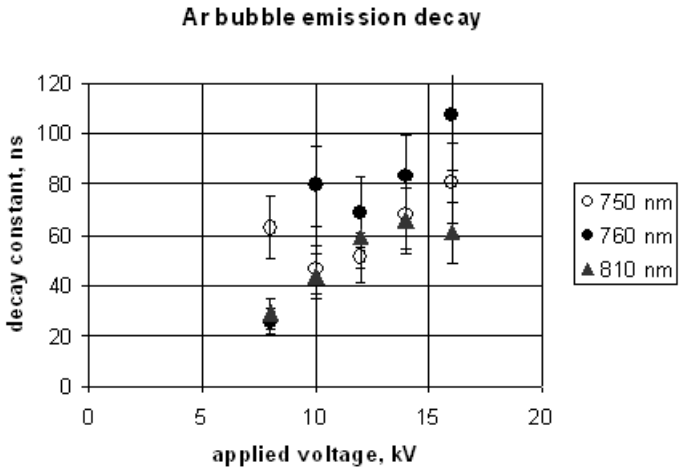

Figure 4.2.4 This graph shows a summary of the results for all three wavelength regions. The decay constants here are computed from individual oscilloscope traces and averaged for repeated trials at the same voltage. It is apparent that the decay constants increase with increasing voltage. The decay constants for all three wavelength ranges increase with increasing voltage.

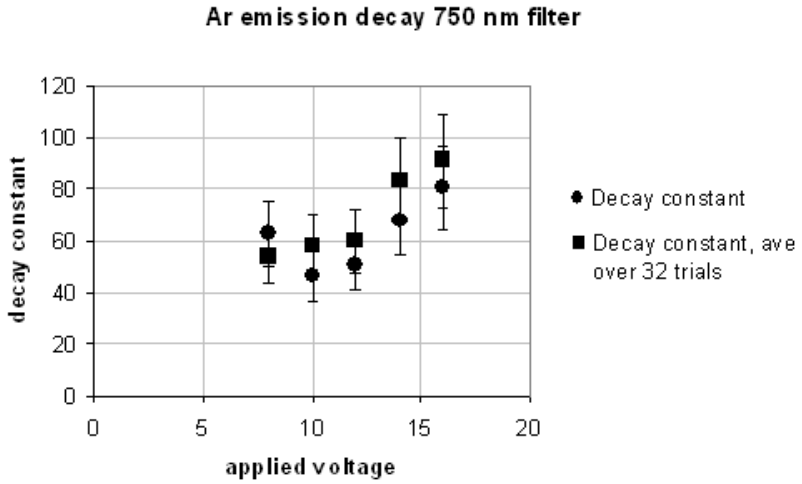

Figure 4.2.5 The graph shows decay constants as a function of applied voltage for optical emission measured with the 750 nm filter. The graph compares the results obtained by averaging several decay constants computed for individual trials with decay constants found by first averaging the oscilloscope signal for 32 trials. The tendency to increase with voltage is better expressed when the measurements using the oscilloscope calculated average signal.

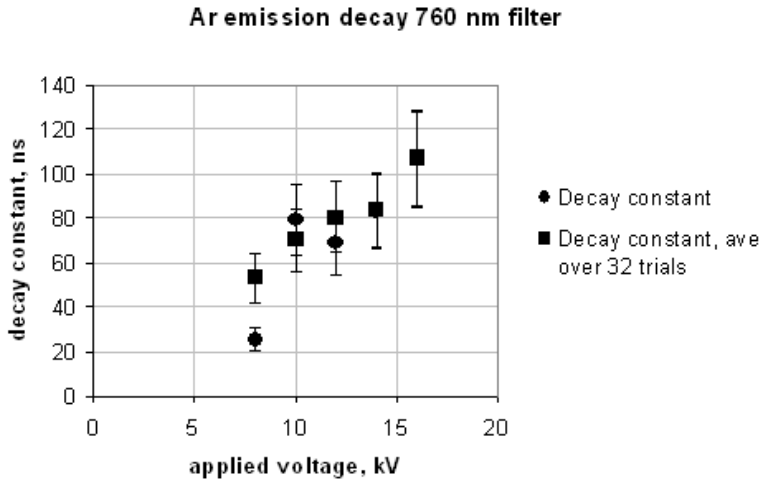

Figure 4.2.6 The graph shows decay constants as a function of applied voltage for optical emission measured with the 760 nm filter. The graph compares the results obtained by averaging several decay constants computed for individual trials with decay constants found by first averaging the oscilloscope signal for 32 trials. The tendency to increase with voltage is better expressed when the measurements using the oscilloscope calculated average signal.

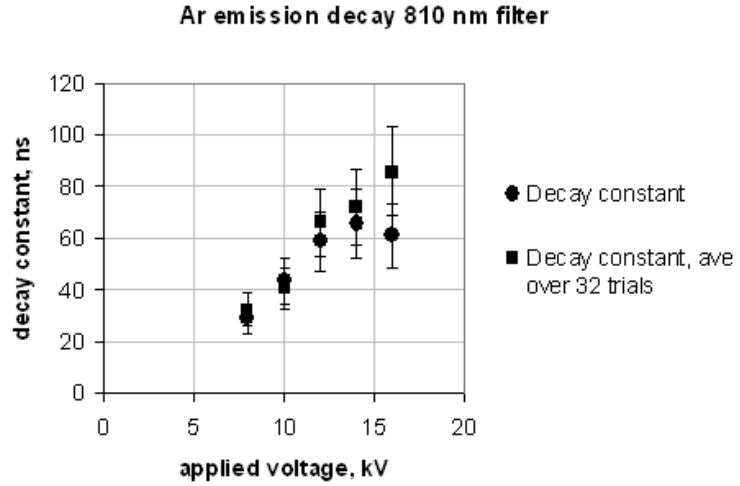

Figure 4.2.7 The graph shows decay constants as a function of applied voltage for optical emission measured with the 810 nm filter. The graph compares the results obtained by averaging several decay constants computed for individual trials with decay constants found by first averaging the oscilloscope signal for 32 trials. The tendency to increase with voltage is better expressed when the measurements using the oscilloscope calculated average signal.

Table 4.2.1 This table presents a summary of decay constants for different voltages in frequency range. The decay values are obtained from the oscillograms of each individual pulse and the values for repeated pulses at a given voltage are averaged. These results are plotted in figure 4.2.4 (See Appendix 1 for more detailed record of these calculations).

Decay after first peak, ns			
Voltage, kV	750 nm	760 nm	810 nm
8	63	26	29
10	46	79	44
12	51	69	59
14	68	83	66
16	81	107	61

To investigate the dependence of the decay rates on the applied voltage, two kinds of averaging have been used. One way is to determine the decay rates for each trial and average the results. The decay rates determined for each trial are averaged for each voltage in a given optical range. The results are summarized in Table 4.2.1 and plotted in Figure 4.2.4. The error is estimated at about 20% in all ranges. In spite of the individual variations and within the experimental error, the decay constant shows a tendency to increase with voltage for all spectral ranges tested here.

The second way of averaging is to use the oscilloscope to automatically average the signal for 32 shots at 1 Hz (Fig 4.2.2). The averaged data files are then used to find the decay rate for each applied voltage. This technique can be used since the decay constants have been shown to be independent of repetition for up to 50 consecutive shots. The results are presented in Figures 4.2.5, 4.2.6, and 4.2.7 for the 750 nm, 760 nm, and 810 nm filters respectively. The robustness of the illuminated trends becomes apparent

from this exercise as the individual fluctuations are smoothed and all the trends remain. This analysis increases the confidence in these results.

As evident from the data in Table 4.2.1, the decay rates are consistently lower in the 750 nm and 810 nm ranges and longer in the 760 nm. The decay rates in all of these three ranges increase with increasing voltage as evident in figures 4.2.5 – 7 and Table 4.2.1. The shortest observed decay rates are ~26 – 30 ns.

Several Ar emission lines fall into the described filter band regions. The 750.39 nm and the 751.47 nm lines are the only two in the range of the 750 nm filter. Although not a single line, the radiative lifetimes of these two lines are close, 22.7 ns for the 750.39 nm line and 24.88 nm for the 751.48 nm line. The 760 nm filter admits only one strong line, the 763.51 nm line with radiative lifetime of 40.82 ns. The 810 nm filter admits two lines, the 810.37 nm with the radiative lifetime of 40 ns and the 811.53 nm, radiative lifetime of 30.2 ns. All experimental results shown in Table 4.2.2 give decay constants longer than the radiative lifetimes of the upper energy levels of the corresponding emission lines.

Table 4.2.2 The data in this table represent the same conditions as the results presented in table 4.2.1 except for the averaging method. Here 32 shots are averaged by the oscilloscope and the resulting traces are analyzed. The radiative lifetimes for Ar lines in each filter range (from the NIST atomic spectra database[1]) are given at the bottom of the table for comparison with the experimental results.

Averaged decay constant, ns			
Voltage, kV	750 nm	760 nm	810 nm
8	**54**	**53**	**32**
10	**58**	**71**	**40**
12	**60**	**81**	**66**
14	**83**	**84**	**72**
16	**91**	**107**	**86**
radiative lifetimes for	22.7	40.82	40
individual lines [1]	24.88		30.2

In summary, the results show that the Ar emission in the three specified spectral ranges decays at a rate slower than it would due to spontaneous radiative relaxation. These decay constants increase with increasing voltage applied to the system.

4.2.2. Investigation of optical emission from an Ar bubble in the 310+/-5 nm region.

Water vapor in the bubble and liquid water at the surface of the bubble are constantly present in all experiments. The 310+/-5 nm region isolated by the band pass filter is mostly dominated by the rotational 306.4 nm system of OH ($A^2\Sigma^+$ - $X^2\Pi$) 0 – 0 transition. The OH 0 – 0 band has the greatest intensity at 308.9 nm (as shown in the spectrum in Figure 4.4.1b) and four band heads are visible. This band filter also allows the transmission of a portion of the second positive system of N_2 (always present in systems open to the atmosphere), but the highest intensities of this band should be beyond the transmission window of the filter. Essentially the data obtained using this filter corresponds to the presence and the behavior of the OH radical. Spectral data shown later in this work, confirms the high intensity of the radiation in this range.

The first set of measurements presented here (Figure 4.2.8) shows the increase in the intensity of the OH band both as a function of voltage and as a function of the bubble size. The increase in emission intensity as a function of voltage is apparent from the graph. The increase in intensity for a larger bubble is not presented in these graphs since

the measurements in Figure 4.2.8(a) and 4.2.8(b) are taken with a different control voltage on the PMT. To be able to see low intensity signal with good resolution, and not to overload the PMT with a high intensity signal, the control voltage needs to be adjusted appropriately. The bubble glows almost the entire time of the voltage pulse once the voltage is high enough that multiple current peaks are present (Fig. 4.2.8 (b)). The larger (8mm in diameter) bubble is used in all experiments except those specifically testing the effect of the size of the bubble.

Figure 4.2.9 shows the optical emission recorded in the 310+/-5 nm region during a discharge in an 8 mm diameter Ar bubble at 9.5 kV. As in the previous oscillograms, optical emission starts immediately with the current signal and decays slower than the current. The difference in the decay rates of the current and the optical emission is clearly seen in the larger view of the highest current peak from the previous oscillograms. The current peaks broaden with repeated shots and so in shots >#50 both the current and optical emission follow the same time schedule. Table 4.2.2 shows the results of time constant calculations for repeated shots of the same bubble at 5kV. The average decay rate for OH emission is 34+/-7 ns at 5kV. Increasing voltage for the same size bubble does not seem to affect the decay rate (Table 4.2.3). Individual fluctuations of results at one voltage are about to the same order as the variations of the signal across several voltages. The relationship on voltage cannot be determined from this data.

The overall average decay constant for the OH 0-0 band is determined to be 31.9 +/- 7.7 ns. The updated value for the radiative lifetime of the ($A^2\Sigma^+$ - $X^2\Pi$) transition is 686 +/-70 ns [2]. The experimental value is dramatically lower than the radiative lifetime of this transition.

The prominent presence of the OH band radiation in the optical emission from Ar bubbles is important. This highly oxidizing and reactive agent is used in many cleaning and decomposition applications of discharges in bubbles in water. For the purposes of understanding and characterizing this discharge, the presence of OH rotational band gives a convenient way to determine the rotational temperature of the gas in the bubble (Section 4.4.2.3.1).

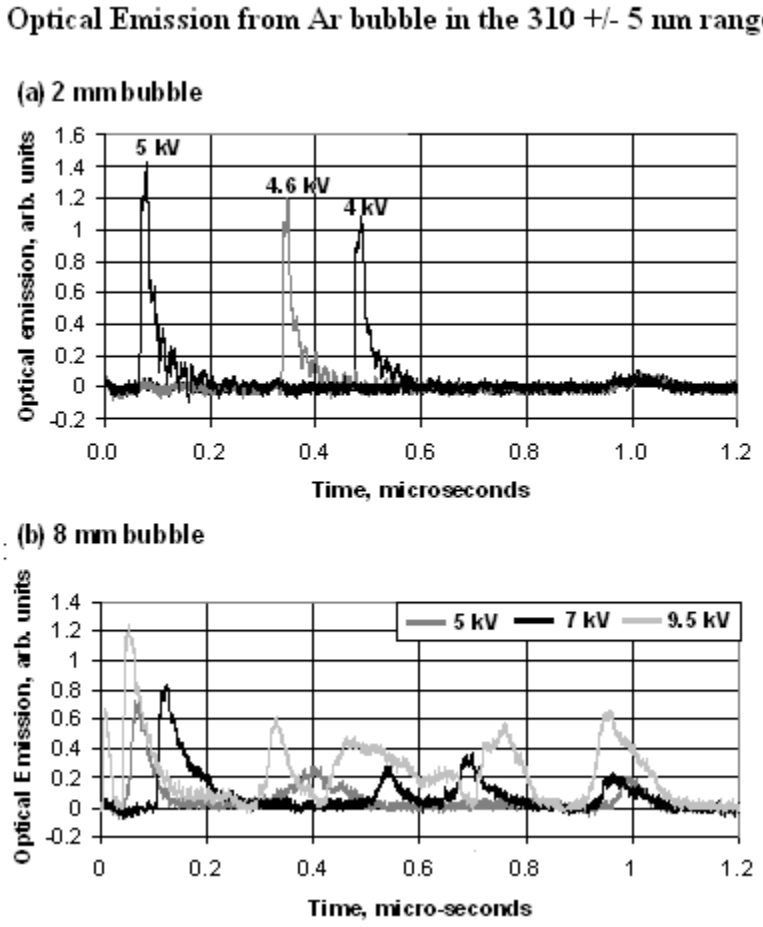

Figure 4.2.8 Optical emission signals are shown here for a 2 mm and for an 8 mm diameter bubble. Figure (a) shows the signals recorded at 4 kV, 4.6 kV, and 5 kV applied to the same 2-mm bubble. Figure (b) shows the signal recorded at 5 kV, 7 kV, 9.5 kV applied to the 8-mm Ar bubble.

(a)

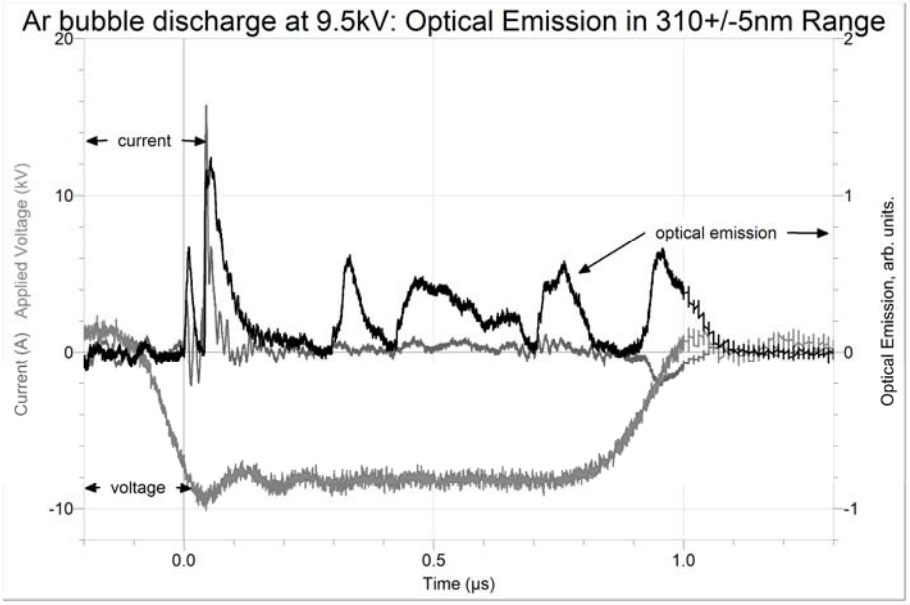

(b)

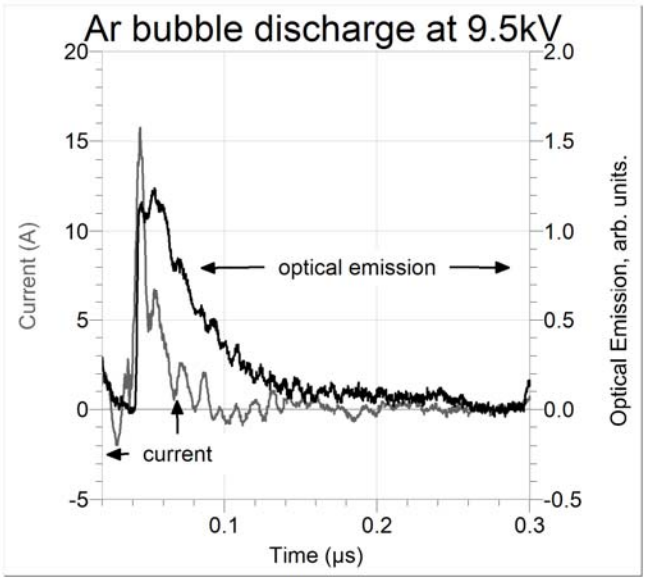

Figure 4.2.9 Graph (a) shows optical emission together with the current and voltage oscilloscope traces for an 8 mm Ar bubble discharge at 9.5kV. Multiple current and emission peaks are present. A larger view of the highest intensity emission and current peaks in graph (b) makes it easier to see the slower emission decay rates compared to current.

Table 4.2.3 Optical emission decay rates in the 310 nm range at 5 kV for repeated shots for the same Ar bubble.

OH band emission decay constant at 5kV	
trial	decay constant, ns
1	37.1
2	27.8
3	30.6
4	31.0
5	24.5
AVERAGE	**30.2**
STD. DEV	**4.7**

Table 4.2.4 Optical emission decay rates in the 310 nm range for Ar bubble discharge at different voltages

OH band emission decay constant at different voltages	
Voltage, kV	decay constant, ns
4.5	27.6
5.0	29.6
5.4	24.5
6.0	24.5
7.0	45.5
8.0	37.9
9.5	33.6
AVERAGE	**31.9**
STD. DEV	**7.7**

In conclusion,

- OH radicals are produced in the discharge in Ar bubbles in water.
- Experimentally determined decay time for the OH ($A^2\Sigma^+ - X^2\Pi$) transition is 31.9 +/- 7.7 ns, more than an order of magnitude shorter than the radiative lifetime of 686 +/-70 ns [2] for this transition.

References:

1. Ralchenko, Yu., Kramida, A.E., Reader, J., and NIST ASD Team (2008). *NIST Atomic Spectra Database* (version 3.1.5), [Online]. Available: http://physics.nist.gov/asd3 [2008, August 15]. National Institute of Standards and Technology, Gaithersburg, MD.
2. J. R. Gillis, A. Goldman, G. Stark, C. P. Rinsland *Journal of Quantitative Spectroscopy and Radiative Transfer*, **68, Issue 2**, (2001), Pages **225**-230

4.3. Time resolved optical imaging

This section contains the results of the imaging the discharge in an Ar bubble under a set of typical conditions. The voltage of 12 kV is above the minimum but not the highest tested in other experiments. An 8 mm bubble is used for almost all experiments that involve optical emission studies. As mentioned above (Chapter 3) the objective lens produced 8 pixels/millimeter resolution and so a bigger bubble is more suitable. The results reported here include the images with 1200 ns exposure repeated 100 times, the images with 5 ns exposure with a 5 ns step (241 steps take the 1200ns of the voltage pulse), and the images taken with 20 ns, 100 ns, and 200 ns exposures both repeated and sequential (see sections 3.4.2-3 on imaging). In all the images shown here, the needle appears on the left side of the image instead of at the top, and the bubble surrounds the needle on the right side. The image is rotated 90 degrees counterclockwise from the physical set up.

4.3.1. Time-averaged images

The images with the 1200 ns exposure give time-average picture taking into account the light emitted at any time from the time the voltage starts to rise to the time voltage drops to zero. These time-averaged images are used to get a general overview of the discharge from a spatial point of view. The images immediately reveal two main characteristics. From one shot to another, the discharge takes a different path through the

bubble, appearing to shoot at a different place on the bubble. The second most prominent feature is the brightness of the needle area. The area around and in front of the tip of the needle appears brightest in all shots. One hundred consecutive shots were fired and recorded in 100 frames of images. Sample frames are shown in Figure 4.3.1. The frames are randomly selected and so the similarity as well the variation among this sample set is representative of the entire set of 100 images. For example, shots #4 and #20 look almost identical, while in the other shots the discharge takes different paths. Most frequently, the discharge appears to shoot for the bubble surface either directly in front (below in reality) of the needle or to some other close region. In frames #7 and #72, the discharge seems to take a path along the top surface of the chamber. This interpretation of the image is not certain since the same exact image would result if the discharge propagated toward a part of the bubble wall almost directly across from the needle, not down, but horizontally toward the observer. Viewed in its flat projection this path to a close region at the top of the bubble would look as though it was directed along the top wall. In most frames, the light appears to extend along the wall of the bubble. Some part of this is probably the discharge continuing along the wall after making contact with the water surface, but some of this may be due to the reflection of light from the surface of the water.

The WinSpec® software available from PIActon, the manufacturer of the ICCD camera used in optical emission experiments here, provides the user with the ability to set up and plot three dimensional graphs showing the intensity of the signal recorded at each pixel on the CCD. This 3-D plot is useful for identifying detailed variations in the image that are difficult to discern from either grey-scale or color coding information about the intensity of the signal. A sample 3-D plot (corresponding to frame #3) is shown in Figure

4.3.2. The corresponding image frame is shown in the top left corner of the figure. An outline of a bubble is sketched by hand for visualization purposes. The position of the bubble and the needle are determined from a separate reference shot of the chamber without the discharge.

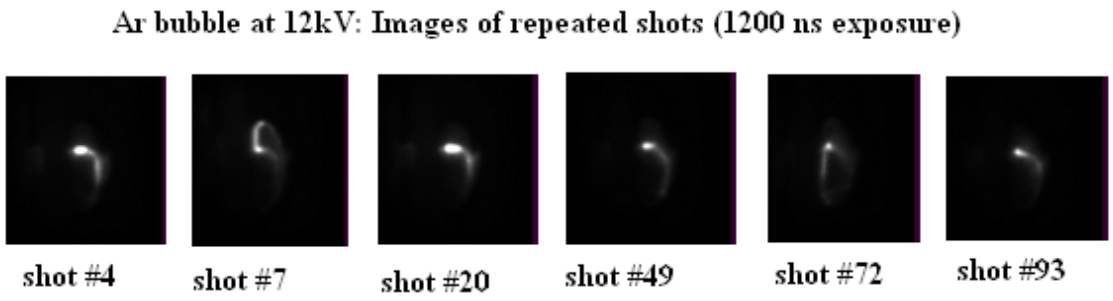

Figure 4.3.1. The figure shows random samples selected from 100 frames of 1200 ns exposure images. 12kV voltage pulses are applied to Ar bubbles at a rate of 1Hz and the images are synchronized with the discharge.

Fig. 4.3.2 clearly shows the maximum photon count directly around the tip of the needle. The tip of the needle is 4 pixels or 0.5 mm long and the tip is located at (55, 80) in pixel coordinates. The intensity decreases sharply away from the tip of the needle and extends toward the bubble wall. A region along the bubble wall appears to be bright.

This preliminary set of images provides a general overview of the discharge. It appears to emit light most intensely in the region surrounding the tip of the needle and extend toward the bubble wall. These results lack information on the temporal evolution of the discharge. Where does the discharge originate, what sequence of events does it follow from the start, how does it extinguish? A more detailed investigation has been conducted to answer these questions and the results follow.

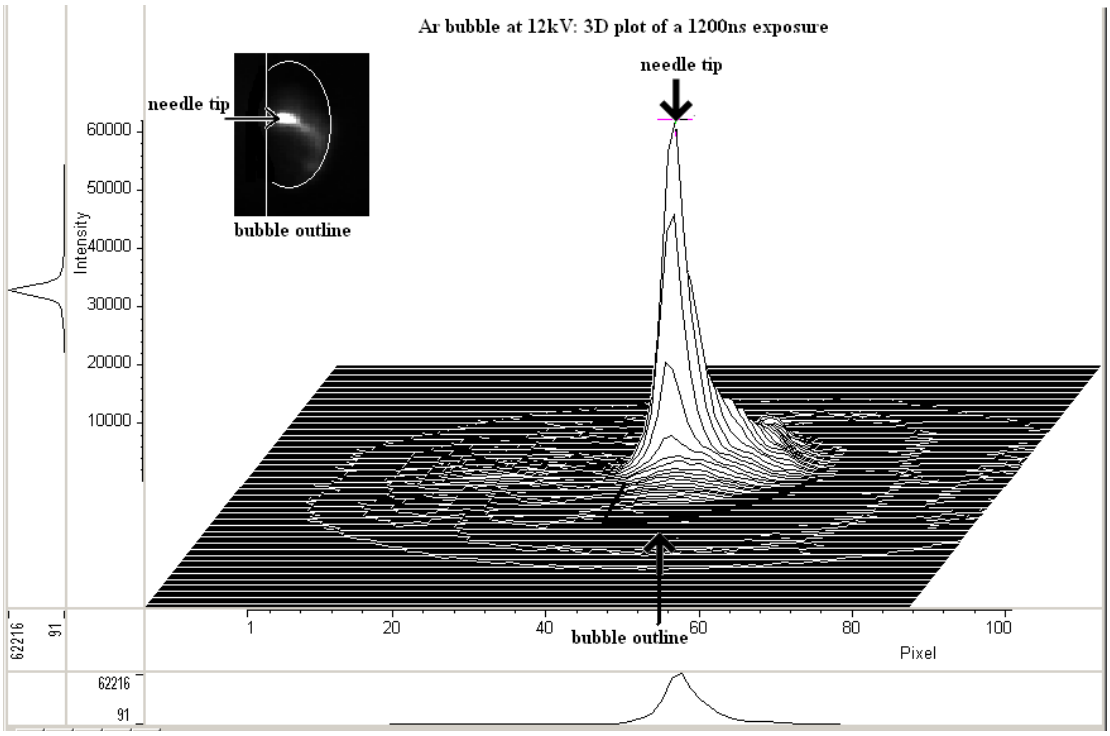

Figure 4.3.2 The graph shows the intensity (arbitrary units) recorded at each pixel on the CCD in frame #3. The image is one of 100 images taken of a discharge in an 8mm diameter Ar bubble. Images are synchronized with voltage pulses (12kV at 1Hz). The image of the discharge is shown in the upper left corner. The arrows indicate the location of the tip of the needle (x=55, y=80 pixels) and the outline of the bubble. At the bottom and on the left side of the graph are the cross sections of the graph along y=80 and x=55 lines respectively.

4.3.2. Time-resolved images

The time resolved sequence of images presented here is also taken with 12kV pulses applied to an 8 mm Ar bubble at a rate of 1Hz. The images are also timed relative to the discharge and are gated to a 5 ns exposure. The camera gating advances 5 ns with each exposure, so these are 5 ns snapshots of discharge processes taken at consecutive times during discharge development. The first frame is taken the first time a pulse is applied to a new bubble, but frame 200 is taken during the 200th shot at the same bubble

and 1000 ns into the process. For a more detailed explanation please see the experimental Sections 3.4.2-3 and Fig. 3.4.3 on camera gating. The first nine shots of this sequence did not capture any light, and the images of the discharge start with shot #10. From the camera timing, it is known that this time corresponds to the start of the current. The voltage has reached the flat part of the curve at the time the current starts. (See Fig. 4.1.2) The applied voltage remains essentially constant for about 800 ns, so most of the frames are recorded with 12kV applied to the Ar bubble system.

The sequence of frames shown in Figure 4.3.3 is selected to highlight the changes in the discharge. Therefore at the time of rapid change, corresponding to current buildup or fall, for example, frames are selected at close time intervals for more detailed information. During the times of low activity, the frames shown are separated by longer time periods. Selected samples are presented for illustration purposes. All recorded frames have been analyzed in these experiments. The table includes information on the intensity scale chosen for each image. The changes in the intensity scale mean that relative to frame #15, frames #21 – 56 are brighter in reality, and frames #66 to the end are dimmer. Even with this change of scale, some of the detailed information from the brightest images is lost, and some of the dimmer frames show background light reflected off the water surface. This reflected light is also visible in the brightest shots, in frames #12 – 21, for example. Each frame in Fig. 4.3.3 is also accompanied by the value and the location of the maximum intensity in the given frame.

Frames #10 - 20 show a rapid increase in light intensity. Time values from these measurements should be treated qualitatively only, since there are both random variations and systematic changes in the signal from one shot to the next as presented in section 4.1.

Visually, it appears that the discharge starts at the tip of the needle and is non-uniform. The brighter regions then develop along the direction away from the needle until reaching the water (see Fig. 4.3.3 frames #15 – 18). Upon reaching the bubble wall, the discharge continues along the water, sometimes forming a bright region at the point of the initial contact with the wall.

The graphs of recorded light intensity at each pixel on the CCD are extremely helpful in verifying visual impressions quantitatively. A set of these graphs is shown in Figures 4.3.5 and 4.3.6. To help reading the graphs, the location of the needle and the maximum intensity are indicated on one sample graph (Figure 4.3.4). In addition, the bubble outline is sketched in and the location of secondary intensity peaks is also indicated. The corresponding image frame is given in the upper left-hand corner of the figure, also showing the location of the needle and the outline of the bubble. The location of the needle is (55, 58) in this experiment, and the contour lines are plotted along the x and y directions from the location of the tip of the needle. The location of maximum intensity right at the tip of the needle and the extension of light emission toward the bubble wall are clearly visible on the graph.

Frames #12 to 21 show the increase in intensity around the needle and the extension of the discharge region toward the wall. The intensity increases more drastically around the needle than elsewhere in the discharge. It is interesting to notice that once the discharge has reached the surface of the bubble, a bright area forms at the water edge. As the discharge begins to extinguish (Fig. 4.3.3, frames #23 – 56), the light diminishes first in the bulk of the bubble between the needle and the water, and the bright spot at the bubble wall lingers (as seen in frame #26).

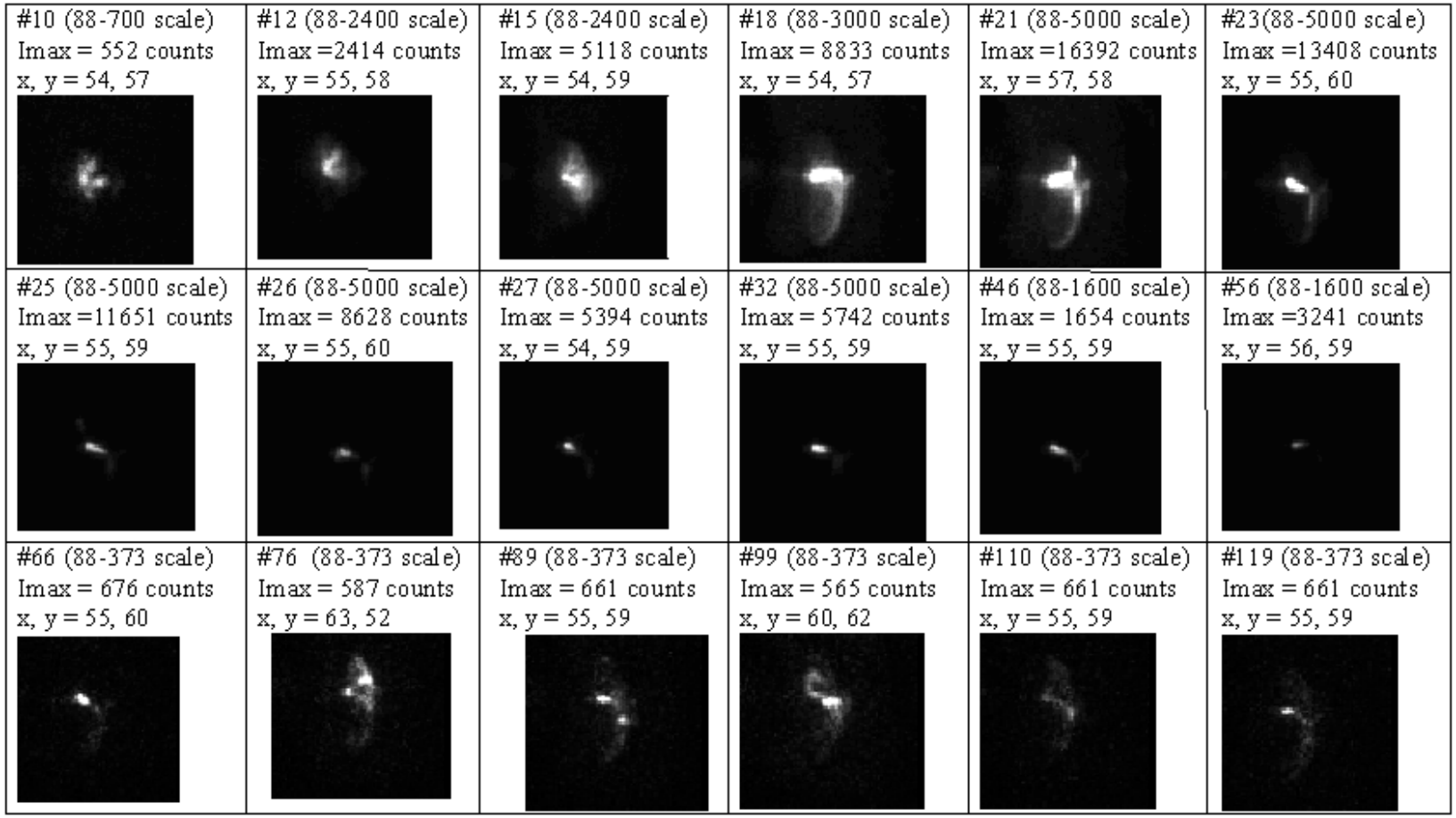

Figure 4.3.3a The figure shows selected frames from the large Ar bubble 12kV image sequence. Information given with each image includes the frame number, maximum intensity in each frame, and the location (x, y) of this maximum. The scale is chosen in favor of faint detail sacrificing some of the bright details. This also makes diffuse light reflected off water surface visible in most pictures. (The figure is continued on the next page)

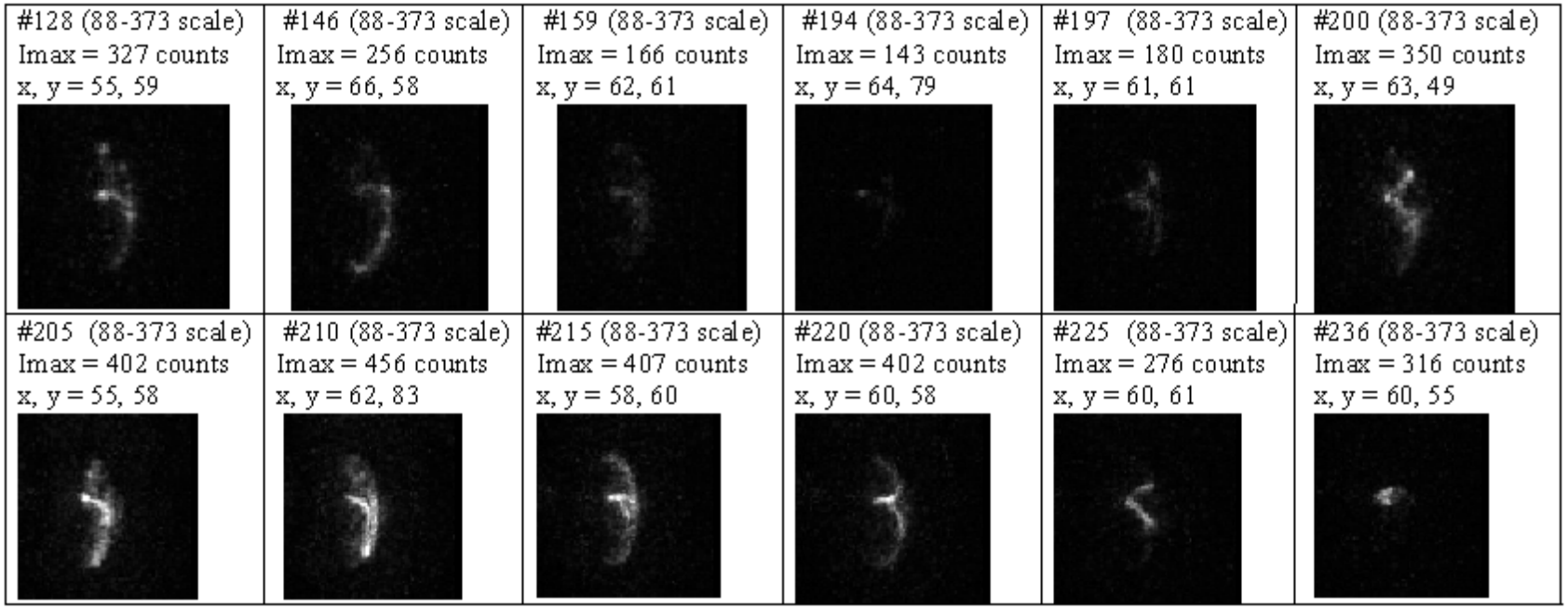

Figure 4.3.3b The figure shows selected frames from the large Ar bubble 12kV image sequence. Information given with each image includes the frame number, maximum intensity in each frame, and the location (x, y) of this maximum. The scale is chosen in favor of faint detail sacrificing some of the bright details. This also makes diffuse light reflected off water surface visible in most pictures.

The discharge then continues to shrink towards the needle while the area immediately around the tip of the needle continues to emit light almost the entire time the voltage is on.

Statistical analysis of each frame provides information on the position of the intensity maximum and minimum, their values, and other statistical information. The graph in Figure 4.3.7 shows the x and y coordinates of maximum intensity in each frame. This graph allows us to see again that the needle is the brightest most frequently, followed by an area on the bubble wall and a region in the bubble from the needle to the water. The graph illuminates a following interesting feature of the discharge. Almost the entire surface of the bubble is covered with points of maximum intensity, indicating that the discharge strikes and reaches various points along the bubble wall.

Graphs in Figures 4.3.8 and 4.3.9 show the x-coordinate and the y-coordinate as functions of the frame number. These graphs illuminate the temporal evolution of the discharge. It is clear from these plots that the region around the needle is the absolute brightest region in the bubble for about 80 frames or about 400 ns, long after the discharge is essentially extinguished. It is when the light intensity is only a factor of 2 above the background that the brightness of other areas becomes comparable to that of the region around the needle.

4.3.3. Reproducibility of repeated shots

Experiments with a set timing and exposure time provide information about the discharge in the same time interval during the discharge and allow a comparison between

repeated applications of voltage pulses to the same bubble. Ar bubbles are again subjected to 12kV applied voltage pulses repeated at 1Hz. During each pulse an image is recorded as soon as the discharge begins. The exposure time for these images is 20ns longer than the previous experiment, but still short enough to get some information about the initial stages of the discharge. Several of these images are shown in Figure 4.3.10. The images and their 3-D plots are used to determine the effective radius of the bright area. This measurement is taken in pixels and converted to millimeters. The average region with light intensity above two times the background level extends about 0.85+/-0.05 millimeters from the tip of the needle. The discharge during this time hasn't yet reached the surface of the bubble (Figure 4.3.11). From frame to frame the discharge looks the same as it does in the first few frames of the previous experiment. Although the spatial resolution is not sufficient to see any kind of detailed structure of the discharge, the experiment provides an average view of the early stage of the discharge.

4.3.4. Imaging small bubbles

Bubbles that are 2-3 millimeters in diameter are considered small compared to the 8 mm bubbles previously discussed. The report on this experiment is short since the small size of the bubble coupled with low resolution, prevent detailed examination of the structure of the discharge. The experiments clearly support the observation that the discharge begins in the region around the needle and progresses out toward the water (Figure 4.3.12).

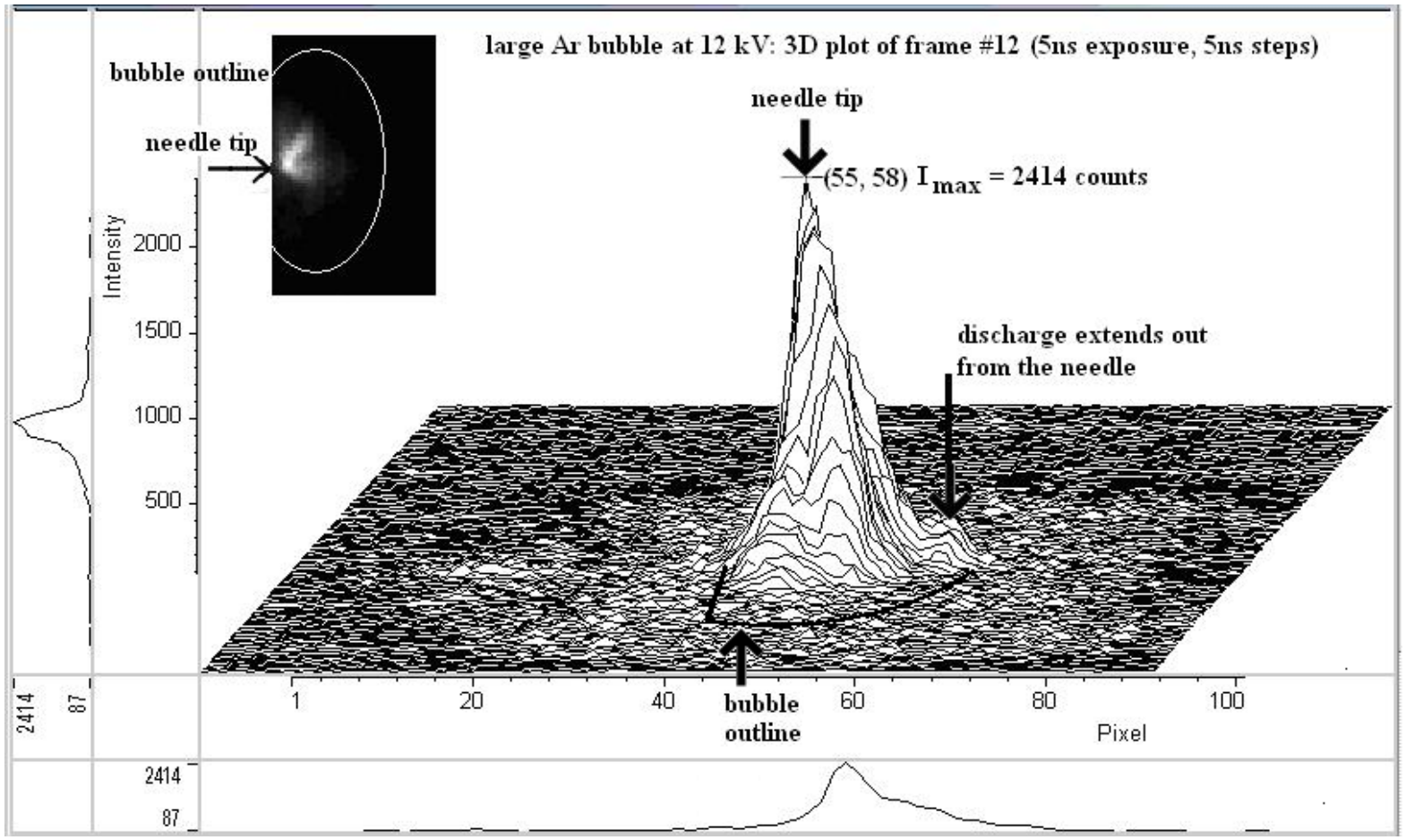

Figure 4.3.4. Shown, is a 3D plot of light intensity in frame #12. The image of frame #12 is shown in upper left of the figure. This is the second 5ns step since the first captured light. and The maximum photon count per pixel in this frame is 2414 at 55, 58 (pixel location). The arrows indicate the position of the needle (pixel coordinates 55+/-1, 58+/-1) and the extension of the light away from the needle. Along the bottom and the left edges of the figure are the contour lines along y= 58 and along x=55 respectively. Approximate bubble outlines are sketched in for visualization purposes.

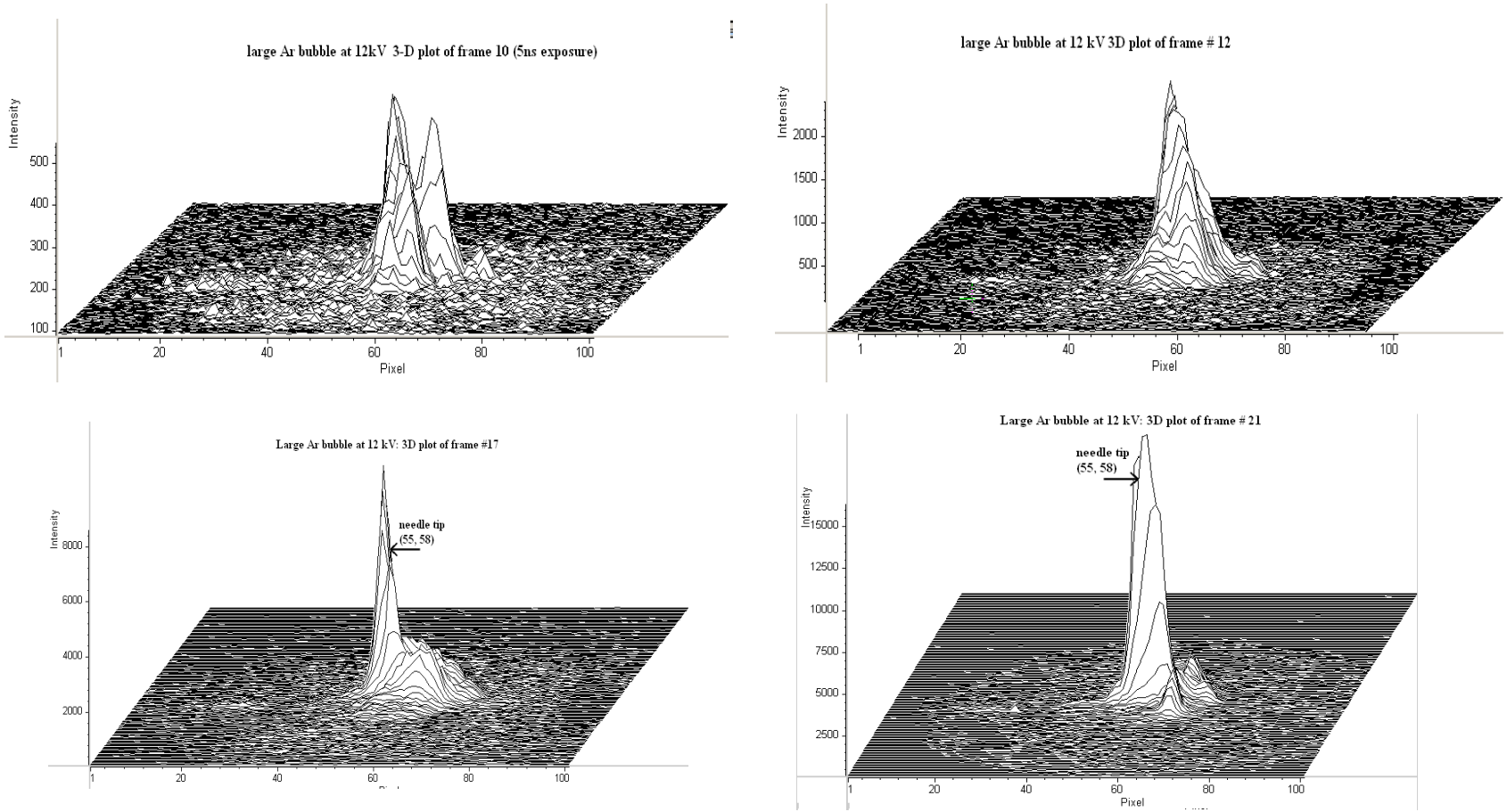

Figure 4.3.5. Graphs of light intensity recorded at each pixel location for selected frames. Light is emitted by the same Ar bubble subjected to 12kV voltage pulses applied at a frequency of 1 Hz. Each frame is gated for a 5 ns exposure time and the time the frame is taken advances 5 ns for each shot/frame. The arrows show the coordinates of the tip of the needle. This figure shows the increase in intensity from frame to frame. Selected frames are (as marked) #10, 12, 17, and 21.

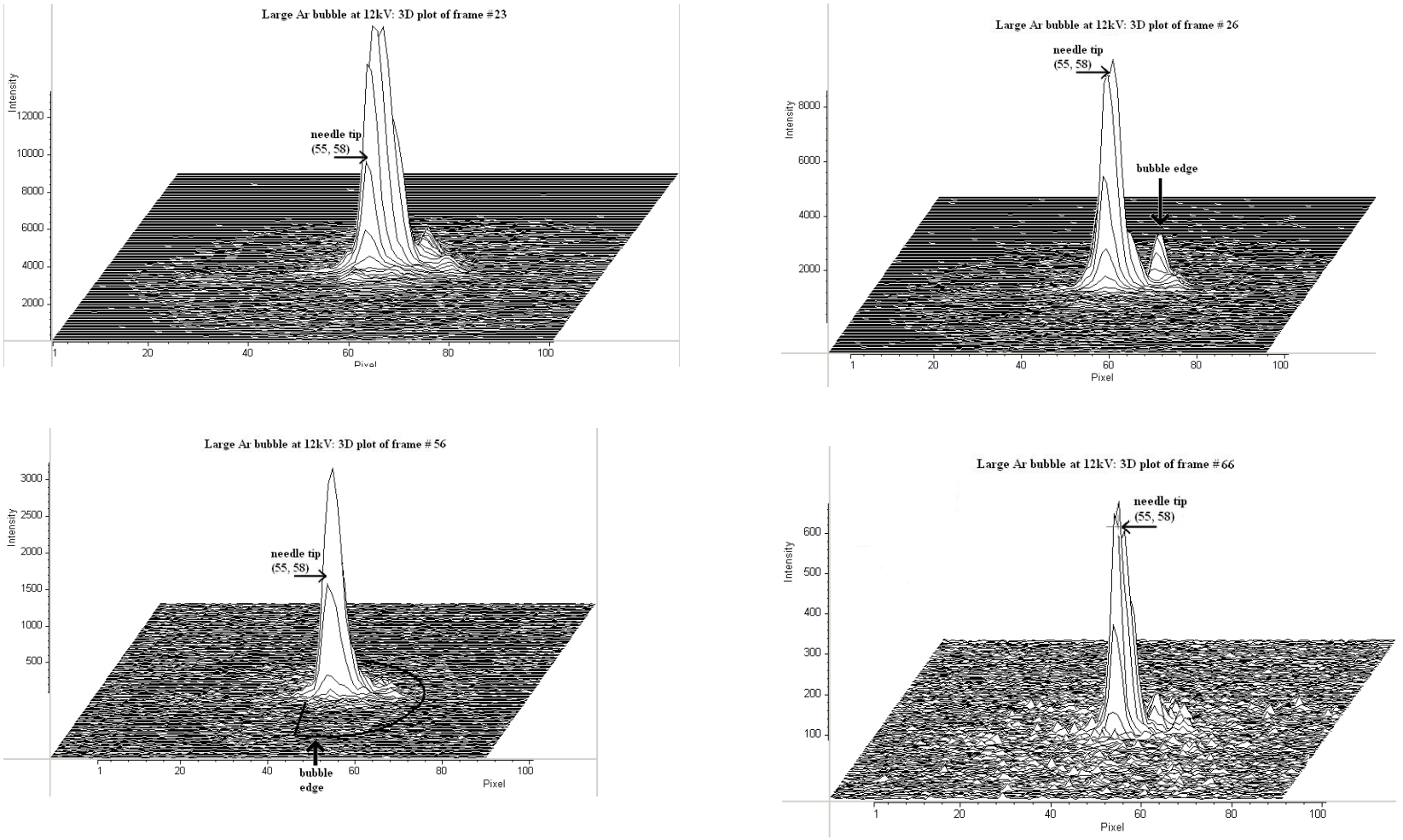

Figure 4.3.6. Graphs of light intensity recorded at each pixel location for selected frames. Light is emitted by the same Ar bubble subjected to 12kV voltage pulses applied at a frequency of 1 Hz. Each frame is gated for a 5 ns exposure time and the time the frame is taken advances 5 ns for each shot/frame. The arrows show the coordinates of the tip of the needle. This figure shows the decrease in intensity from frame to frame. Selected frames are (as marked) #23, 26, 56, and 66.

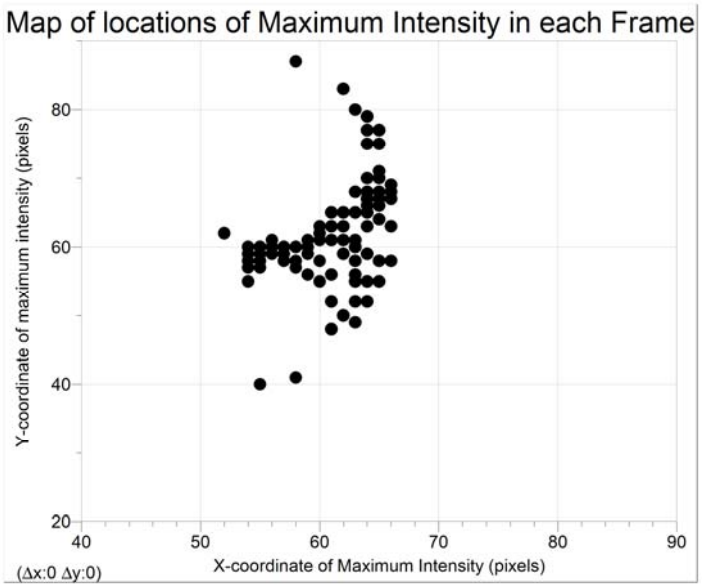

Figure 4.3.7 The graph shows the locations of intensity maxima in each frame for the entire set of images. The graph includes the data from 231 images taken of the discharge in an 8 mm Ar bubble at 12kV. The graph shows a higher density of points in the region around the tip of the needle, along a path to the bubble wall and at the bubble wall.

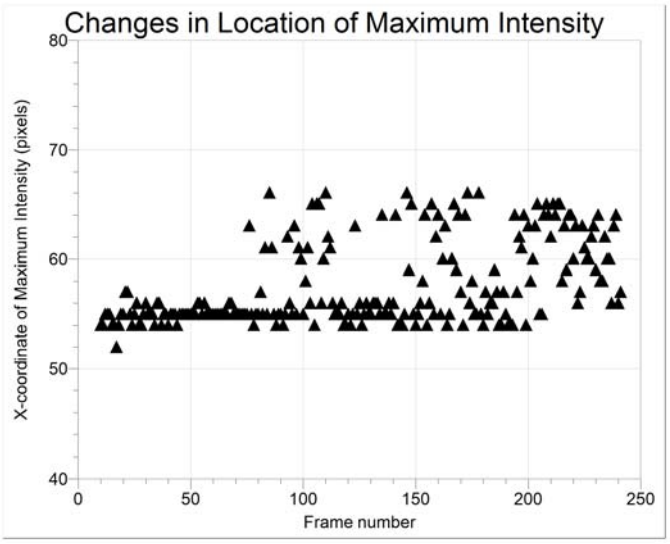

Figure 4.3.8. The graph shows the x-coordinate of intensity maximum as a function of the frame number. Images are taken sequentially advancing the timing by 5 ns with each shot. The graph shows that the intensity maximum is always around the needle for the first ~70 frames or 350 ns.

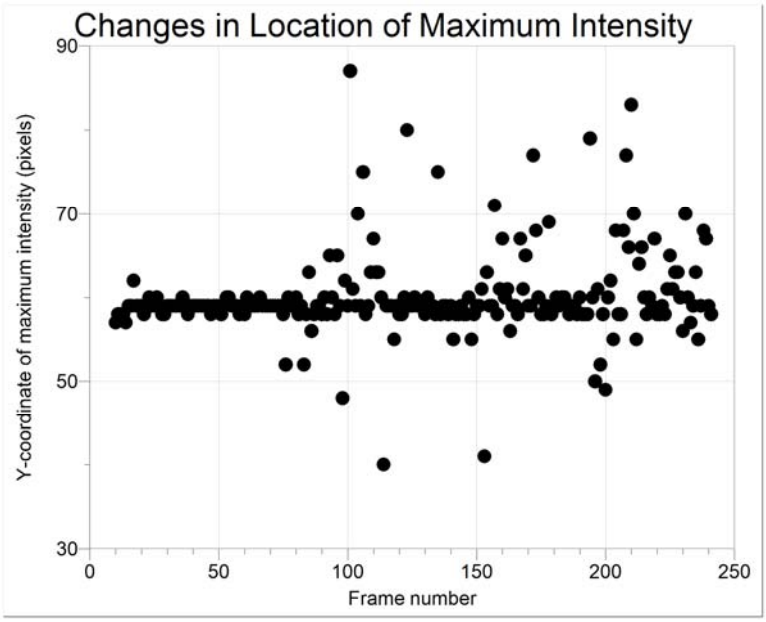

Figure 4.3.9 The graph shows the y-coordinate of intensity maximum as a function of the frame number. Images are taken sequentially advancing the timing by 5 ns with each shot.

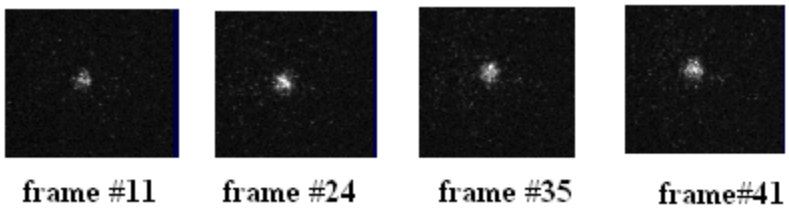

Figure 4.3.10. The figure shows images of the first 20 ns of a discharge in an Ar bubble at 12kV. The exposure time for each frame is 20 ns.

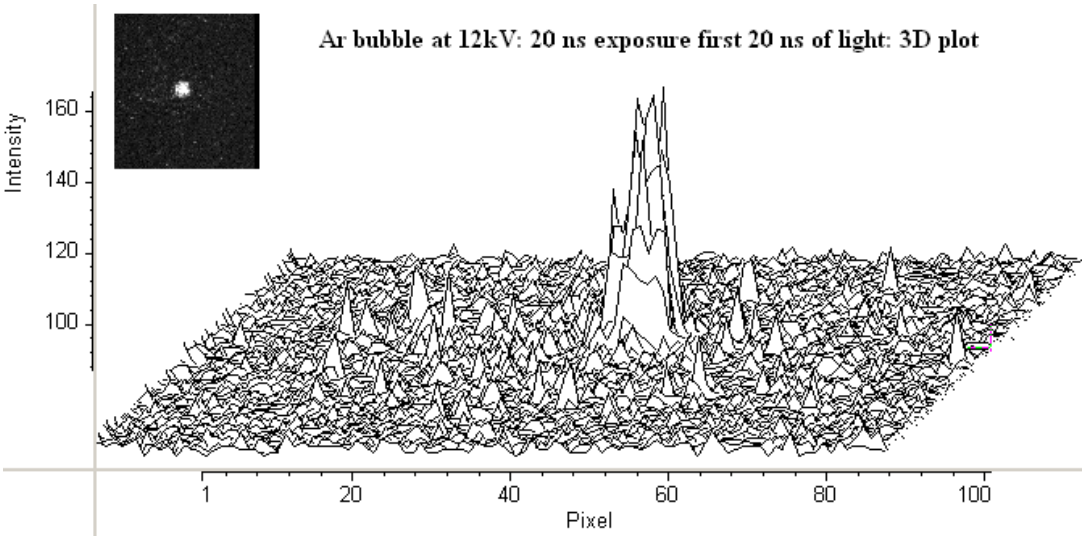

Figure 4.3.11. The graph of intensity at each pixel for the first 20 ns is shown for a discharge in an Ar bubble at 12kV. Exposure time for one frame is 20 ns.

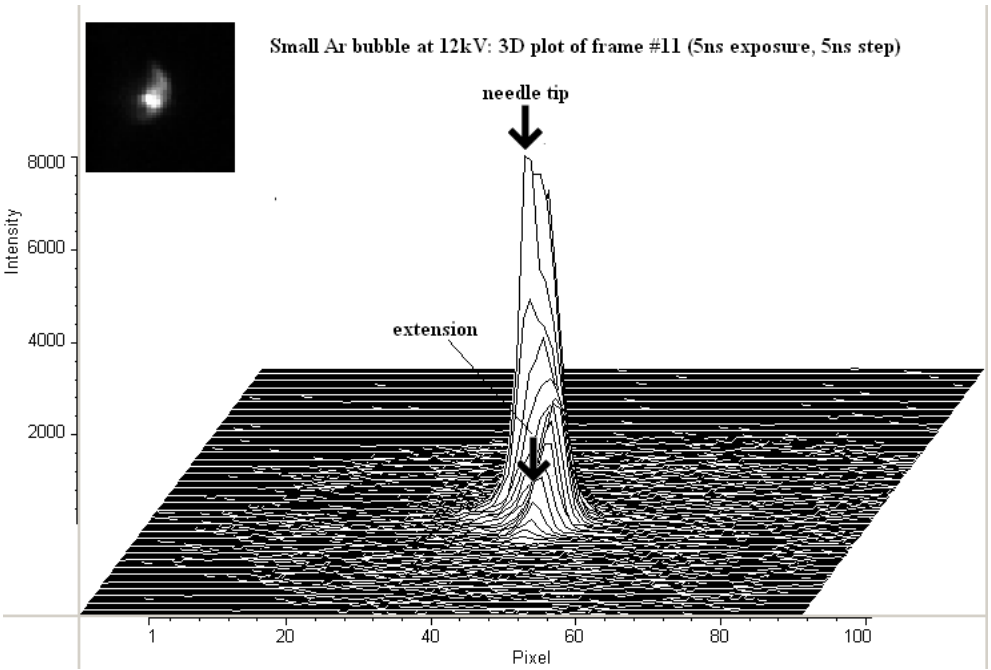

Figure 4.3.12. The figure shows the graph of intensity at each pixel for a 2mm diameter Ar bubble at 12 kV. The graph and the image represent the data for frame #11 of a 241 frame sequence with a 5 ns step and 5 ns exposure time.

4.3.5. Comments on the data

A picture is worth a thousand words and very appealing, but results must be interpreted carefully since many complications need to be taken into account. Comparing frames 10 and 20 for example, means comparing a 5ns snapshot 50 ns into the tenth shot with a snapshot 100 ns into the 20^{th} shot. The electrical characteristics of the discharge show that changes occur with repeated shots. It is clear that all indications of duration of light emission should be compared to either the averaged results or the results for later shots. The electrical signature of the signal retains it main characteristics for up to 50 shots, so the beginning of the sequence may be considered representative of the processes that occur during the first current peak and some time after. The ending shots are still representative of the events occurring during the reverse current pulse since the reverse pulse is present in all shots.

The light reflected from the water's surface is prominently featured in most frames. In some frames there is even an appearance of two discharge paths occurring simultaneously. A careful examination of the location of each path shows that the second path is a reflection of the first one in the water. The bubble also distorts the image and so the actual path may look as though the discharge travels along the top of the chamber or the bubble wall but that may be just the point of view of the camera objective. Most of the time, it has been possible to overcome these difficulties

4.3.6. Summary of Imaging Results

The images provide clear time-resolved information about the discharge. The discharge starts in the region around the needle, increasing in intensity in that region, and then beginning to extend out from the needle toward the water surface. Upon reaching the water's surface, the discharge continues along the surface sometimes spitting into a couple of different paths. A relatively bright area sometimes appears at the point where the discharge strikes the surface of the water. The discharge follows different paths through the bubble striking the walls in various places. Once the light intensity reaches a maximum level, the discharge begins to extinguish. The decrease in light emission begins

along the discharge path between the water and the needle. The region at the bubble wall goes out next. The region around the tip of the needle continues to glow and at higher voltages may be visible in the recorded images almost the entire time the applied voltage remains constant. Once the voltage drops to a low enough level, the discharge restarts. It seems to follow a similar sequence of events as the primary discharge, but with a greater variability in the recorded light intensity due to the lower overall intensity level.

In conclusion, the most striking properties of the discharge in the Ar bubble, are as follows:

- In repeated trials the discharge follows different paths in the bubble striking different parts of the bubble wall.
- The region around the needle is the brightest region in the discharge and continues to glow almost throughout the duration of the voltage pulse.
- The discharge develops first at the needle and extends out toward the wall.
- The discharge extinguishes first the regions in the gas farthest from the needle shrinking around the tip of the needle.
- A secondary discharge has similar characteristics but is of lower intensity than the primary discharge.

4.4. Discharge Investigation Using Emission Spectroscopy

Ar discharge spectra are presented in Figure 4.4.1. These spectra cover the regions of 260 – 370 nm and 630 – 870 nm and contain (as expected) both line emission and molecular rotation-vibrational bands. Radiation intensity in the region from 400 nm to 600 nm is too low to discern any features, so this region is omitted. The spectra show atomic lines as well as molecular bands and are used in this investigation to gather as much information as possible about the discharge process in an Ar bubble. This section is divided into subsections based on the type of information that may be gathered from the spectrum.

4.4.1. Optical emission and the production of active species

The shorter wavelength part of the spectrum (260 – 370 nm) is dominated by the molecular band emissions. Most of these emission bands have been identified as OH or N_2 vibration-rotation bands. Other bands are identified as those of O_2. The gas in the bubble includes Ar, H_20 as equilibrium vapor pressure close to the surface of water, and air as an impurity introduced mostly due to air originally in the water samples. Air was not removed from the water in any of the experiments in this study. The spectra clearly confirm the presence of OH, O, and H in the discharge. These chemically active species are important for industrial applications of this discharge.

The OH 306.4 nm system corresponding to the $A^2\Sigma^+ - X^2\Pi$ transition[1, 2] is prominent in the spectrum (Figure 4.4.1b). In addition to simply indicating the presence of this chemically active radical, the emission band is used below for estimating the rotational temperature of the molecules. This system is evident in spectra in the 260 – 400 nm range (Figures 4.4.1a – 4.4.1c). Measurements indicate an apparent increase in intensity of OH emission with increased applied voltage. Numerical estimates are not possible for either this effect or the effect of the processing time (number of shots) on the concentration of the OH radical. The fiber optic cable used to transmit the optical signal from the bubble to the monochromator is centered on the bubble to allow the widest possible collection angle. The discharge follows different paths through the bubble, so the

amount of light collected from one particular discharge event may be quite different from the amount of light collected from another discharge.

(a)

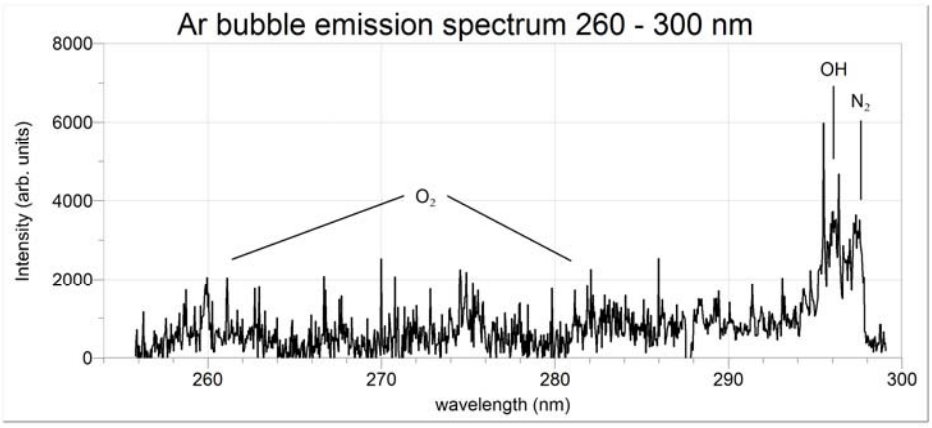

(b)

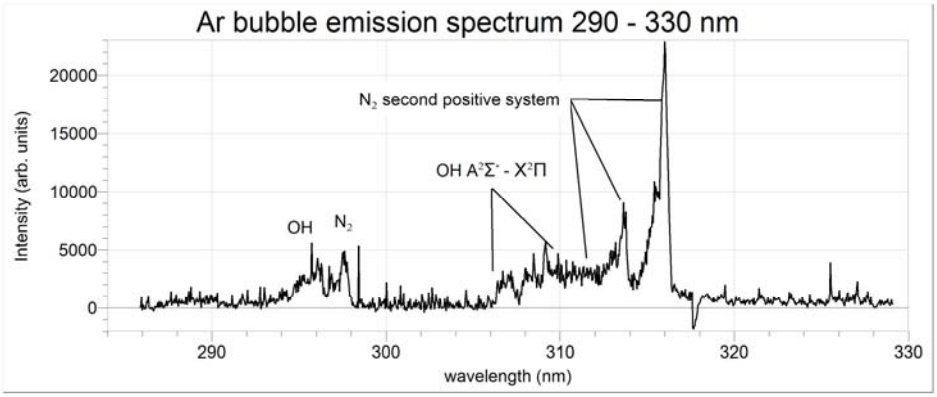

(c)

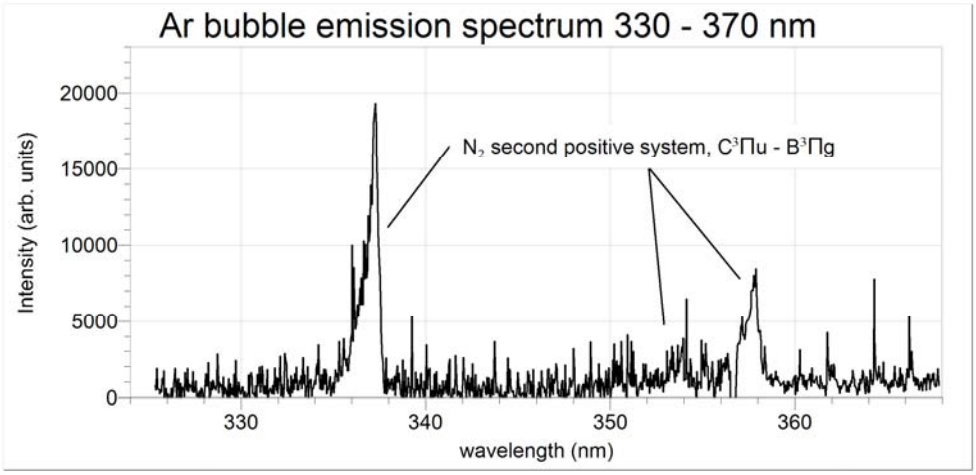

(d)

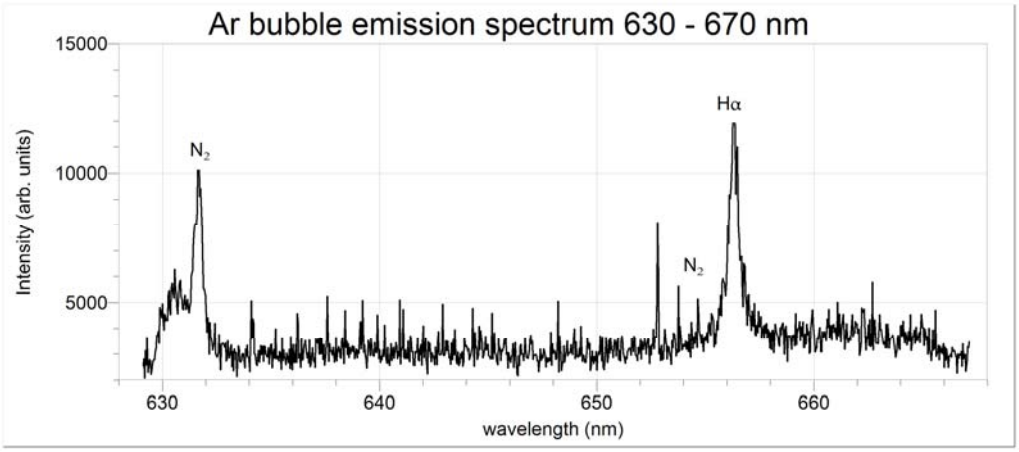
Ar bubble emission spectrum 630 - 670 nm
Intensity (arb. units)
15000
10000
5000
N2
Hα
N2
630
640
650
660
wavelength (nm)

(e)

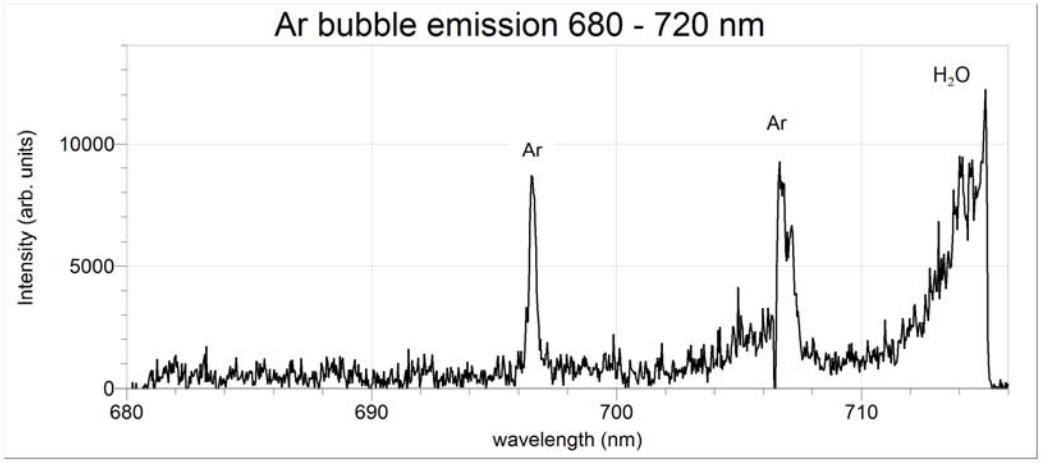
Ar bubble emission 680 - 720 nm
Intensity (arb. units)
10000
5000
0
Ar
Ar
H2O
680
690
700
710
wavelength (nm)

(f)

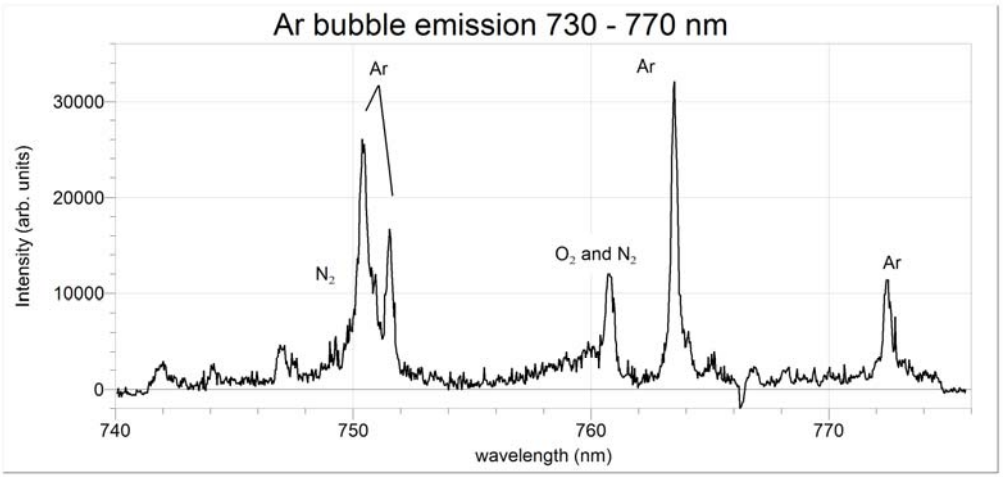
Ar bubble emission 730 - 770 nm
Intensity (arb. units)
30000
20000
10000
0
Ar
Ar
N2
O2 and N2
Ar
740
750
760
770
wavelength (nm)

(g)

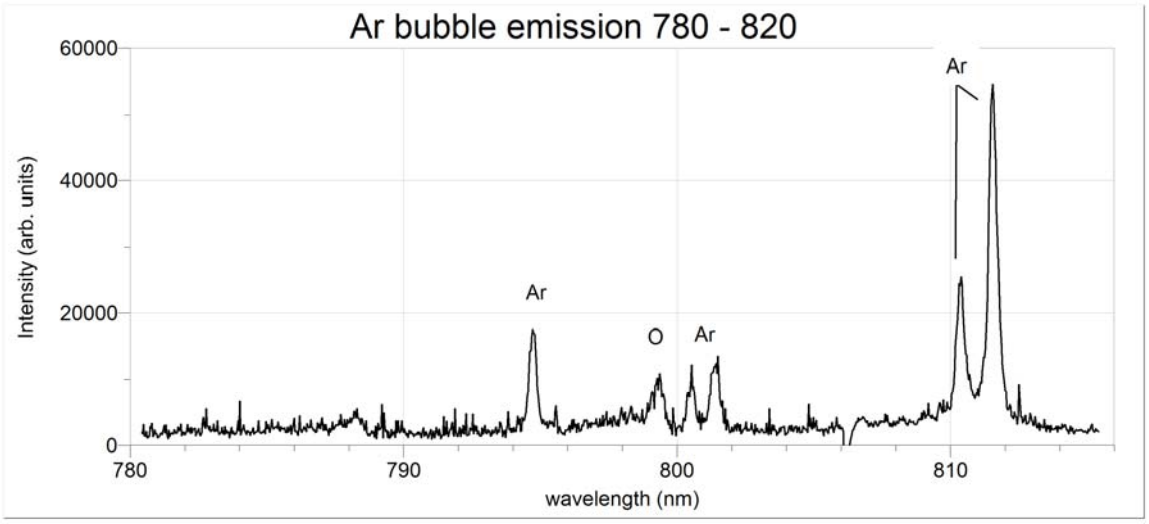

(h)

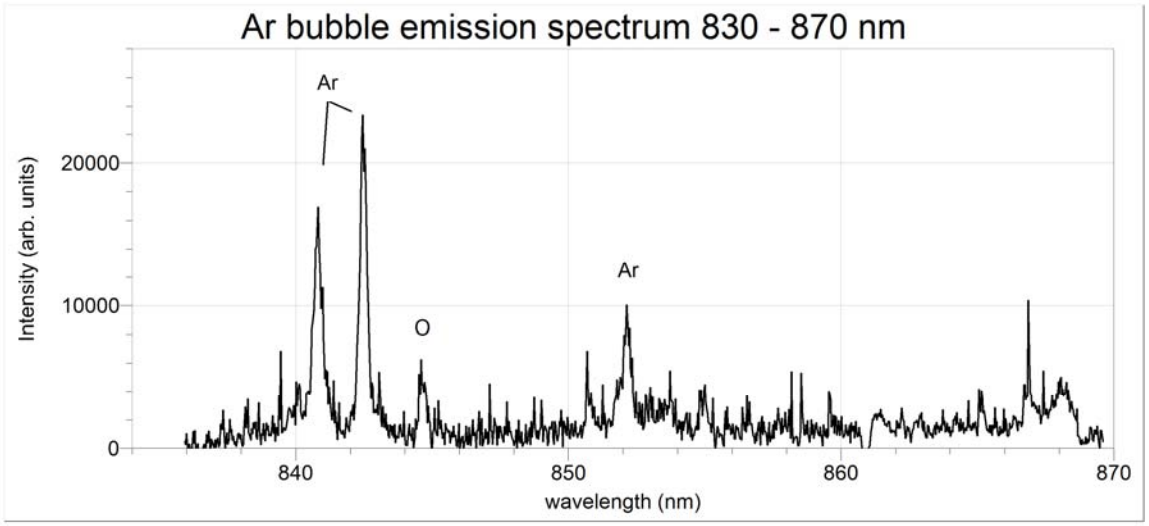

Figure 4.4.1 (a – h) The graphs show a sample spectrum of optical emission from a discharge in an Ar bubble. The monochromator-ICCD set up is designed to take snapshots of 40 nm wide spectral windows. The entire operating range of 250 – 850 nm was scanned but the range of 400 – 600 nm is not shown here since the emission intensity is low in that range. As an example, this is light emission from a discharge in an 8 mm bubble at 12 kV taken with a 200 ns exposure and 50 accumulations.

This makes quantitative comparison of intensity from shot to shot impossible. The measurements based on intensity ratios are not affected.

Discharges in pure nitrogen usually have N_2 and N_2^+ bands present. In this discharge, molecular nitrogen is present as an impurity added to Ar gas. N_2 molecular bands are visible in almost throughout the entire spectrum shown here (Fig 4.4.1), but N_2^+ emission is absent within the experimental background level. The N_2 second positive band corresponding to the $C^3\Pi_u$ – $B^3\Pi_g$ transition is used below for estimating the vibrational temperature in the discharge.

Atomic lines of Ar, H (H_α), and O are featured prominently in the spectra (Figure 4.4.1d – 4.4.1g). Ionized Ar lines are also recorded and used for analysis below. An attempt to find H_β and H_γ hasn't been entirely successful. H_β may be identified, but the intensity of H_γ emission is too low. Atomic oxygen lines are strong and indicate the presence of this important oxidative agent.

4.4.2. Plasma Parameters using Spectroscopic Methods

4.4.2.1. Electron Temperature

Electrons receive the input electric field energy directly and transmit this energy to atoms and molecules in the gas through collisions. In Ar bubbles most of these collisions result in excitation of Ar atoms that then decay back to their ground state.

$$A + e \rightarrow A^*_i + e \rightarrow A_k + e + h\nu \tag{4.4.1}$$

where species A is excited into a state A^*_i by an inelastic collision with an electron e and then relaxes into a state A_k emitting a photon $h\nu$. The line intensities of the emitted radiation can be used to glean some information about the impacting electrons. This is not a direct line to the electron energy. Relating the electron energies to line intensities requires detailed information about the electron energy distribution, the excitation and de-excitation mechanisms. Line intensity can be written as[3, 4]

$$I_{i,k} = 4\,\pi\alpha\left(\lambda_{ik}\right) n_A b_{ik} Q_{i,k} \int_{\nu_o}^{\infty} \sigma(v) v^3 f_e(v)\, dv \tag{4.4.2}$$

where $\alpha(\lambda_{ik})$ is the spectrometer sensitivity in the given spectral range, n_A is the number density for the atoms or molecules A, b_{ik} is the branching ratio for state i, Q_{ik} is the radiative decay rate for state i divided by the total decay rate (decay rate plus collisional quenching rate), $\sigma(v)$ is the effective electron impact cross section at a velocity v, and f(v) is the electron distribution function. To relate line intensity and electron energy, the distribution function f(v) is needed, but detailed knowledge of the distribution function is rare. Assuming a Maxwellian distribution,

$$f_e(v) = \left(\frac{m_e}{2 \cdot \pi \cdot k \cdot T_e} \right)^{\frac{3}{2}} \cdot \exp\left(\frac{m_e \cdot v^2}{2 \cdot k \cdot T_e} \right) \tag{4.4.3}$$

a characteristic temperature may be determined. Since the electrons are not always Maxwellian, this temperature characterizes the excitation process but not necessarily the electrons.

Several approaches may be taken when using equation (4.4.2) to assess the electron temperature. The most thorough approach is to model a certain frequency range in the spectrum entirely. The model then assumes Maxwell-Boltzmann distribution for the electrons (as in (4.4.3)), uses experimental values for the rest of the parameters and sets up the line intensity as a function of temperature only. The temperature is then optimized by fitting the computed spectrum to the experimental one.[5] Modeling of this discharge is an exciting problem to solve in the future.

Two other ways are possible: evaluating the intensity ratio of two lines[7] and constructing a Boltzmann plot for a series of spectral lines.[6] Both of these approaches have been attempted in this study.

4.4.2.1.1. Electron Temperature Using Line Intensity Ratios

It is clear from equation (4.4.2) that in order to use experimental emission lines, the lines must be carefully selected. The lines should be close enough so that the apparatus sensitivity is about the same. The transitions must be excited directly by collisions with electrons. These transitions must occur spontaneously without the interference of collisions with self, other atoms or other molecules. The following

assumptions help simplify (4.4.2): excitation by electron-collision, pure radiative decay, and Maxwell distribution of the electron energies. Then, the line intensity may be written as[7]

$$I_{i,k} = \frac{h\nu_{ik} n_A A_{ik} g_i}{Q(T)} \cdot \exp\left(-\frac{E_i}{k \cdot T_{exc}}\right) \tag{4.4.4}$$

where (ν_{ik}) is the frequency of emitted radiation, g_i is the degeneracy of the upper level, Q(T) is the partition function, E_i is the upper level energy, and A_{ik} is transition probability for spontaneous radiative emission from i to k. Using the ratio of the two intensities

$$\frac{I_{m,n}}{I_{i,k}} = \frac{\nu_{mn} A_{mn} g_m}{\nu_{ik} A_{ik} g_i} \cdot \exp\left(-\frac{(E_m - E_i)}{k \cdot T}\right) \tag{4.4.5}$$

the Boltzmann factor can be determined if transition probabilities A_{nm} and A_{ik} are known accurately. The transition probabilities depend very strongly on the plasma conditions for which they are determined. The majority of sources report these parameters for low pressures when for a given emitted wavelength, neither cascading effects into the upper state, nor quenching of that state is important. These complexities make it difficult to obtain numerical characteristics of the discharge from spectral analysis. The 750.4 nm and the 751.5 nm Ar lines are often chosen for qualitative assessment of the changes in excitation temperature.[7] These lines are excited largely through direct electron-impact excitation from ground state, [5, 9, 10] have short radiative life time, [5, 8, 10] and are close in the spectrums so that instrument sensitivity is the same for both lines. In pure Ar particularly at lower pressures, these two lines would be perfect for temperature assessment. The spectra in the range of 740 – 780 nm (Fig 4.4.1f and 4.4.2) show strong emission at 750.4 and 751.5 nm. The ratio of the line intensities clearly changes in the spectra taken during the first 200 ns of the discharge and the spectra taken during the later part of the discharge (see the camera gating shown in Fig. 4.4.3). During the first 200 ns of the discharge, the integrated line intensity ratio is 2.3+/-0.2 and does not change with increasing voltage. During the later part of the discharge, the intensity of the 750.4 nm line drops appreciably compared to the 751.5 nm line and appears to increase with voltage. Experimental results are shown in Fig. 4.4.4.

The interpretation of these results is complicated by the effect of O_2 and N_2 on these two lines. The N_2 first positive system has a relatively strong band at 750.39 nm that may interfere with the experimental determination of the intensity of the Ar line of this wavelength.

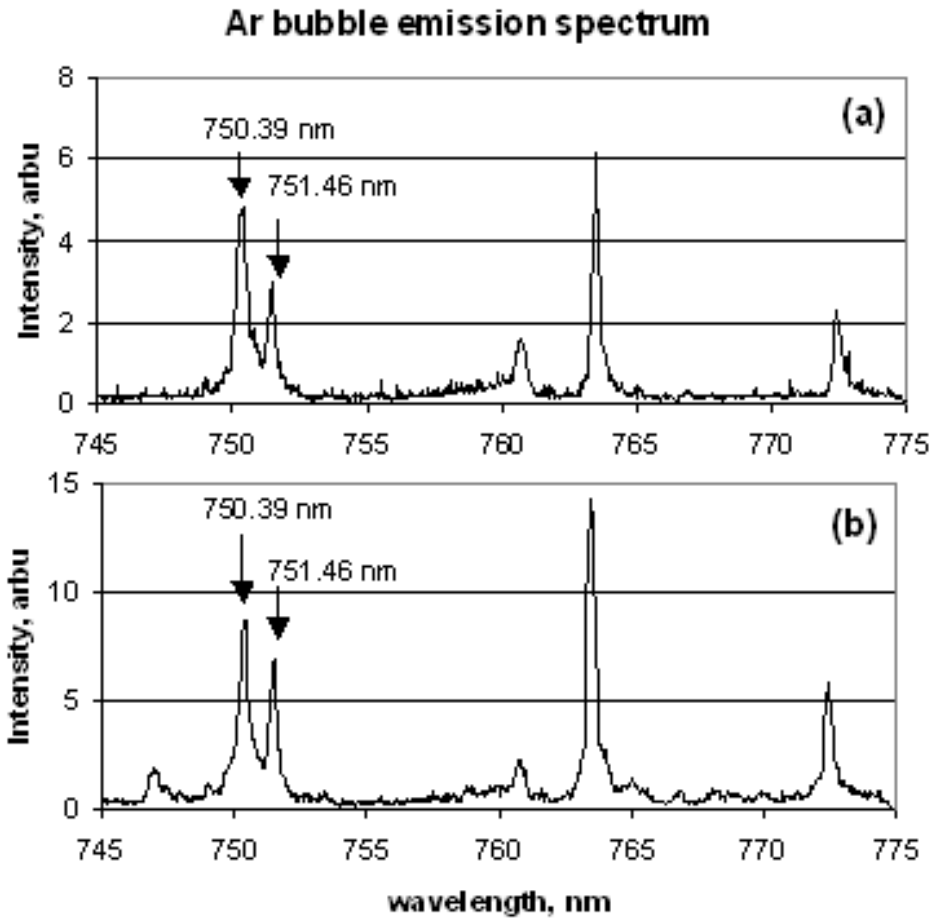

Figure 4.4.2 Ar I emission spectra for the applied voltage of 18kV, 100 accumulations during (a) the first 200 ns of the discharge and (b) the remaining 800 ns.

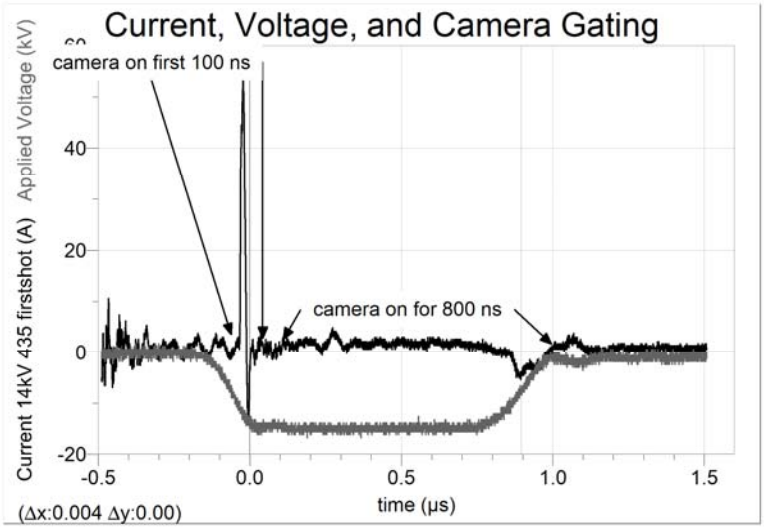

Figure 4.4.3 These current and voltage oscillograms are shown for reference. The ICCD on the monochromator is gated to record the spectrum during the first current pulse (approximately the first 100 or 200 ns) and in other experiments the camera is gated for the time following the first current peak (approximately the later 800 ns).

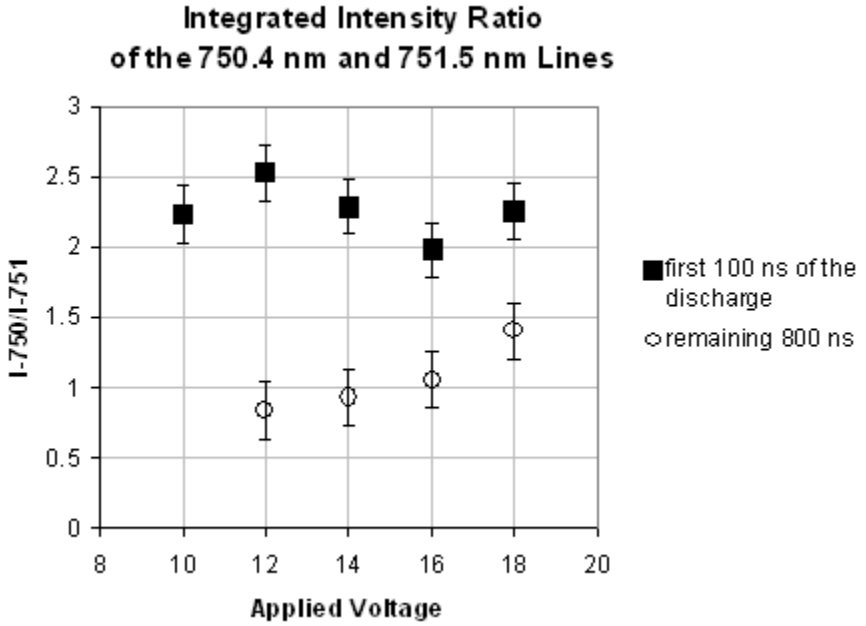

Figure 4.4.4 The graph shows the ratio of the integrated intensity of the 750.4 nm line to that of the 751.5 nm line during the first 100 ns of the discharge and during the remaining 800 ns. The integrated intensities are calculated for different applied voltages. The ratio consistently and drastically decreases after the first 100 ns of the discharge. The ratio during the later time of the discharge shows a tendency to increase with applied voltage.

The presence of both O_2 and N_2 has been reported to effect Ar emission. Ar 750 nm line and other lines emitted by the 4p($2p_n$) Ar* states decrease in intensity due possibly to resonance-enhanced quenching by atomic oxygen.[11, 12]

4.4.2.1.2. Electron Temperature Using a Boltzmann Plot

Computing the excitation temperature from a Boltzmann plot has the advantage that the validity of the approach is verified at the same time. Expression 4.4.5 can be written as

$$\ln\left(\frac{I_{i,k}\lambda_{ik}}{A_{ik}g_i}\right) = -\frac{E_i}{k \cdot T_{exc}} + C \qquad (4.4.6)$$

where C is a constant. Using experimental intensities for a set of Ar lines, the logarithm on the left side is plotted against the energy of the upper state E_i. If the plot is linear, then excitation temperature can be determined from the slope of the line. The lines chosen for this exercise and their information are given in Table 4.4.1. The lines are chosen by looking up electron excitation collision cross sections for the upper states for these lines.[5, 9, 10] An effort has been made to exclude the lines that are likely to be excited from metastable states.

Table 4.4.1 Information on the Ar transitions is taken from the NIST Atomic Spectra Database and used in the calculations of excitation temperature.

ArI line information for finding excitation temperature

wavelength, nm	**751.46**	**794.82**	**852.144**	**840.82**	**840.82**	**826.45**
g_i	1	3	3	5	5	3
A_{ik}	4.29E+07	1.97E+07	1.47E+07	2.44E+07	2.44E+07	1.68E+07
E_i, eV	**13.273**	**13.282**	**13.282**	**13.302**	**13.302**	**13.328**
Intensity, arb. units (example data)	2.00	0.836	0.619	1.06	1.08	0.718

One sample Boltzmann plot is shown in Figure 4.4.5 and the results are summarized in Table 4.4.2. The values for transition probabilities are taken from NIST Atomic Spectra Data Base and the Kuruzc database for high energy

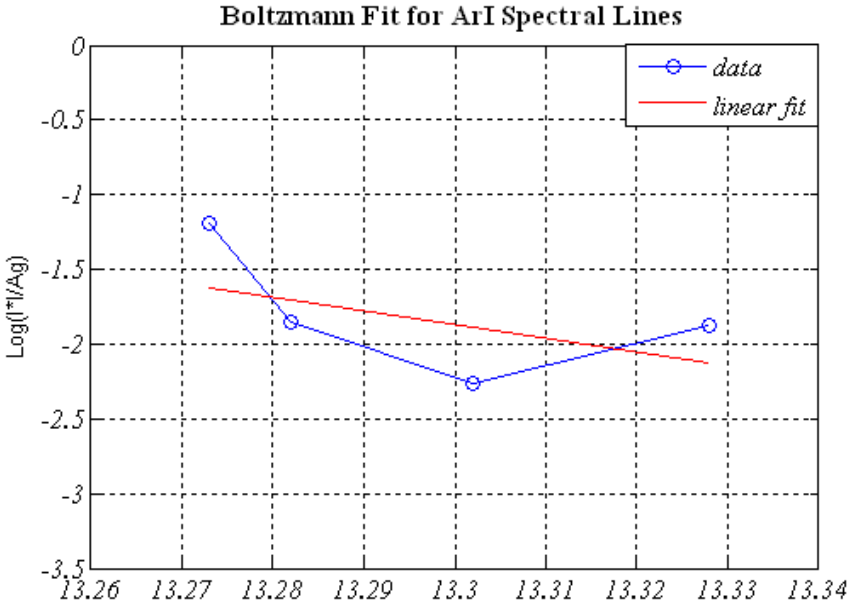

Figure 4.4.5 An example of a Boltzmann plot for the ArI lines listed in table 4.4.1

Table 4.4.2 Excitation temperatures resulting from calculations similar to those shown in Fugure 4.4.5

Excitation Temperature from Boltzmann Plot		
Applied voltage in kV and the time during discharge (first 200 ns; all 1200 ns)	Texc in eV using integrated intensity and Aik from cfa.harvard.edu	Texc in eV using integrated intensity and Aik from NIST
12 kV first	0.0940	0.1014
12 kV all	0.0897	0.0964
14 kV first	0.1020	0.1109
14 kV all	0.1160	0.1276
16 kV first	0.0663	0.0699
16 kV all	0.0662	0.0698

astrophysics (http://www.pmp.uni-hanover.de/cgi-bin/ssi/test/kurucz/sekur.html). The temperature and C are allowed to vary to fit the experimental plot of $\ln(R_p)$ versus E_i. The fitting process is carried out in the MATLAB environment, and the temperature is returned in eV. These calculations return the excitation temperature in the range of 0.07 – 0.1 eV or about 700 – 1100 K. These values seem too low to account for excitations to 13.3 eV levels in Ar by electron-atom collisions.

Another attempt to assess the excitation temperature involves using the hydrogen line sequence, H_α, H_β, H_γ, H_δ. This method is also fraught with difficulties, as only the H_α and H_β are reasonably high intensity, and the H_γ and H_δ lines are very low in intensity with a signal to noise ratio of about 1.3:1. The large uncertainty in these measurements (~40%) demotes this calculation to a level of a ballpark estimate. The calculations have been carried out for 10, 12, and 18 kV and the results are shown in figure 4.4.6. This method gives a much more reasonable estimate of the electron temperature in the range of 0.6 to 0.8 eV (6600 – 8800 K).

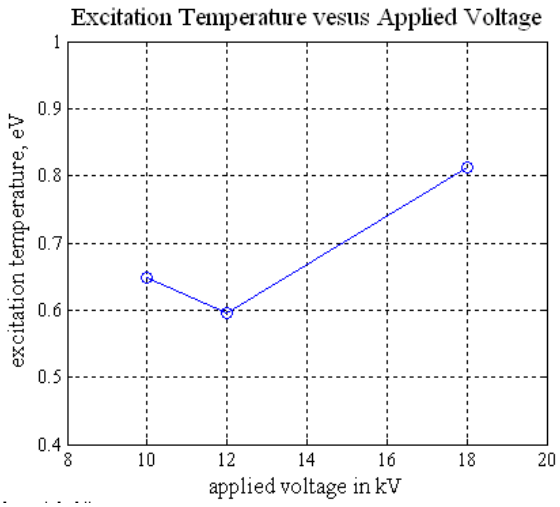

Figure 4.4.6 The graph shows the excitation temperatures determined using H lines for several discharge voltages. Excitation temperature values range from 0.6 to 0.8 eV (6600 – 8800 K).

The results of the two methods just described differ by an order of magnitude. In this case, a third try is reasonable. The third attempt is made using the same technique but this time employing ArII lines. The presence of these lines although very weak is

reasonable to expect in this discharge due to the high density (10^{14} - 10^{15} cm^{-3}) indicated by the charge transferred by the current (See Section 4.1 for details). Locating these lines and finding their intensities is just as difficult as it is working with hydrogen lines. One benefit of using ArII lines is that the spectral region where a sufficient number of these lines are located is not crowded by other emissions, so these lines can be identified with a high degree of certainty in spite of their low intensity. The entire data table including all the line information used in the calculations is shown in Appendix . Transition time, upper level energy, and other information is from the NIST Atomic Spectra Database. An example of a Boltzmann plot is shown in Figure 4.4.7, and the results are summarized in Table 4.4.3. The calculations have been carried out in the MatLab environment as for previous calculations and curve fitting. The results of this method agree with the values determined using H emission. In addition, the temperature appears higher during the first 200 ns of the discharge and decreases with time, since the value for the first 200 ns is 0.75+/-0.05 eV and the value for the entire 1200 ns is 0.65+/-0.05 eV. These data also confirms the trend shown by the line intensity ratios, the decrease in the excitation temperature during the later stages of the discharge.

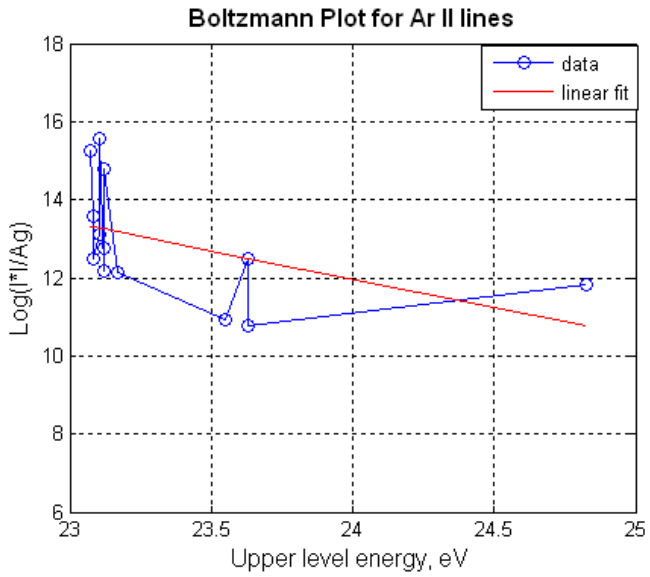

Figure 4.4.7 Logarithm of intensity versus the upper energy level for a set of ArII lines. The scatter in the data is caused by the low intensity of these lines. This trial is for using a spectrum with 200 ns exposure, 100 accumulations, first 200 ns of the discharge in Ar bubble at 14kV.

Table 4.4.3 The table lists excitation temperatures for various conditions and times of the discharge. The temperatures appear higher during the first 200 ns of the discharge and decrease during the later stages of the discharge. Listed are the temperature from spectra accumulated over the first 200 ns and over 1200 ns of the entire voltage pulse. 100 accumulations are used in all cases.

Excitation Temperatures using ArII lines		
	First 200 ns	Entire 1200 ns
Applied Voltage	Excitation Temperature, eV	Excitation Temperature, eV
10.00	0.77	0.645
14.00	0.69	0.6216
16.00	0.79	0.5387
18.00	0.77	0.5896
Average	**0.75**	**0.60**
St. Dev.	**0.05**	**0.05**

4.4.2.1.3. Electron Temperature: Summary

The complexity of the spectra analyzed here includes atomic and ionic line emission, molecular band emission, and a high background noise level due to the high base temperature of the ICCD camera. In addition, the discharge occurs at high pressure and at high electron density. The analysis required a varied and thorough approach where several methods are used and the results are compared. Three out of the four methods attempted produced reasonable values for the electron temperature. More importantly, these methods all highlight the same trends:

1. The electron (excitation) temperature is in the range of about 0.63 – 0.82 eV (7000 – 9000 K).
2. The electron temperature is highest some time during the initial 100 – 200 ns of the discharge and independent of the applied voltage.
3. The electron temperature decreases during the later stages of the discharge and a slight dependence on the applied voltage may be evident.

4.4.2.2. Vibrational excitation temperature

4.4.2.2.1. Vibrational excitation temperature using N_2 emission bands

The spectra shown in Figure 4.4.1 are rich with molecular vibrational bands. These bands correspond to electronic transitions between different vibrational states. Due to their high energies, excitation into various vibrational levels usually results from electron collisions. Spectral information can be interpreted to yield vibration excitation temperature.[12] The method here is almost identical to that used for determining the excitation temperature for various electronic states of Ar atoms. Vibrational bands used for this calculation need to be plentiful and well isolated to accurately determine their corresponding intensities. Nitrogen impurity provides a convenient way of determining vibrational temperature. The bands corresponding to the N_2 second positive system ($C^3\Pi_u$ – $B^3\Pi_g$ transition)[1, 2] are visible in Figures 4.4.1a, b, c.

The first step, as previously is to choose the emission bands in the spectra. The strongest band corresponds to the 0 – 0 transition between the upper ν'=0 and the lower ν" = 0 states. The recorded spectrum does have a strong band in the region of the 0 – 0 transition but only the band with the peak at 337.13 nm is visible; the intensity of the other with Δν=0 is too low. Two other bands with Δν=+1and Δν=-1 are present. The sequence with the strongest head (1 – 0) at 315.9 nm appears readily in the Ar discharges, is easy to identify, and strong, but at the shorter wavelengths it overlaps with the OH 306.4 nm system. The second band system with Δν=+1 is the 357.69 nm system that is well isolated, but again the lower intensity bands drown in the background noise and are impossible to identify. The high level base signal is due to the need for a minimum of 50 accumulations in each experiment and the relatively high temperature of the CCD (-20 ^oC). Finally, only the 315.9 nm system provides three bands useful for finding and plotting the intensities. The data on the transitions used here (corresponding heads at 315.93 nm, 313.6 nm, and 311.7 nm) are shown in Table 4.4.4.[2, 13] The region around 310.05 nm is not useful since the intensity there is greatly enhanced by the overlap with the OH band (See Figure 4.4.1b or 4.4.6).

To construct a Boltzmann plot the energy of upper states needs to be determined. Diatomic molecules may be treated as anharmonic oscillators, so that the energy of a state with a quantum number ν= 1, 2, 3, 4 (for this sequence) is given[1] by

$$G(\nu) = \omega_e(\nu + ½) - \omega_e x_e(\nu + ½)^2 + \omega_e y_e(\nu + ½)^3, \qquad (4.4.7)$$

where G(ν) is the energy of the upper state, and the constants are ω_e= 2047.178 cm^{-1}, $\omega_e x_e$= 28.4450 cm^{-1}, and $\omega_e y_e$= 2.08833 cm^{-1}.[15] The values for the calculated energies as well as other transition information are also found in Table 4.4.4. A representative Boltzmann plot is shown in Figure 4.4.8. Since the energy scale is in electron-volts, vibrational temperature is the reciprocal of the slope of the linear fit. The plots are constructed for every trial and every experimental condition. Rotational temperature calculated using the spectra taken using the first 200 ns of the discharge exhibits much greater variation than the temperature calculated from the spectra taken with 1200 ns gating. The regression coefficient varies from 0.8775 to 0.9913 for the 200 ns gating, but for the 1200 ns it changes from 0.9542 to 0.9918. This is reasonable considering the much lower intensity and therefore much lower signal to noise ratio in spectra taken with 200 ns gating. The results for the vibrational temperatures are summarized in Table 4.4.5.

Table 4.4.4 Calculations of vibrational temperature use the information in this table. The band system used is a part of the nitrogen second positive system that appears readily in Ar discharges even at low nitrogen concentrations.

Nitrogen Second Positive System Transitions with Δν=-1					
*wavelength, nm	frequency, s-1	*upper state quantum number, *v'*	*lower state quantum number, *v"*	Upper level energy, G, eV	**Transition probability, A, x10^7 s-1
315.93	9.489E+14	1	0	0.3729	1.380
313.6	9.560E+14	2	1	0.6127	1.141
311.7	9.618E+14	3	2	0.8455	0.640
310.4	9.658E+14	4	3	1.0712	0.304
*Information from source [2]					
**Information from source [13]					

Using the spectra taken with 1200 ns gating gives temperature values consistent within 3.5% of the average value of 0.84 eV (+/-0.03 eV) or 9000 K. The spectra taken during the first 200 ns of the discharge give results with much greater spread of 11%. The average temperature during this time period in the discharge is 0.73 +/- 0.08 eV or 8000 K.

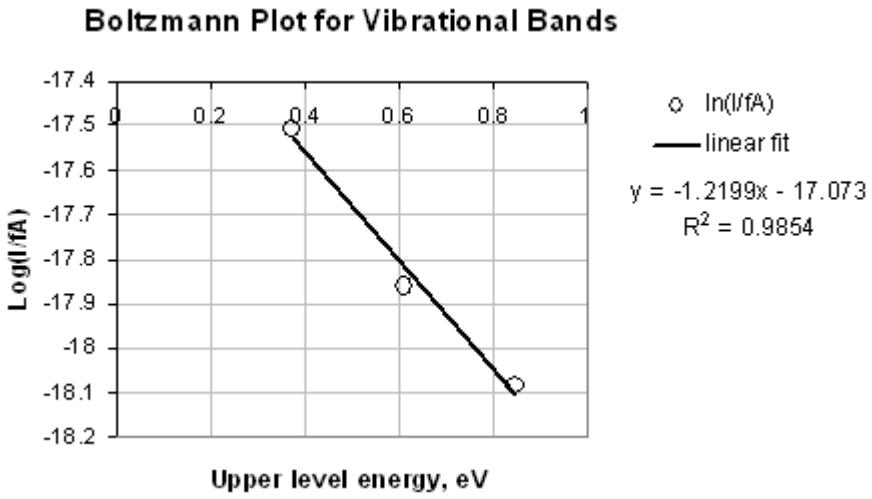

Figure 4.4.8 The graph is a representative Boltzmann plot of the logarithm of intensities versus the upper energy of the transition. Transition information is found in table 4.4.4. The slope of the linear fit yields the vibrational temperature: Tvib = 0.82 eV = 9000 K from this plot.

Table 4.4.5 Results of the vibrational temperature calculations are summarized here. Average vibrational temperature from spectra with 1200 ns exposure is higher than vibrational temperature from spectra taken during the first 200 ns of the discharge.

Vibrational Temperature: Summary of the Results		
From spectra taken during:	entire 1200 ns of the discharge	first 200 ns of the discharge
Applied Voltage, kV	Vibrational Temperature, eV	Vibrational Temperature, eV
10.00	0.83	0.64
12.00	0.88	0.75
14.00	0.82	0.81
16.00	0.88	0.65
18.00	0.82	0.79
AVERAGE	0.84	0.73
STD. DEV.	0.03	0.08

The vibrational temperature during the first 200 ns is lower, without an overlap and within experimental error than the overall average temperature. There is no dependence on the applied voltage. The high degree of linearity in the graphs (although constructed on three points) testifies to the applicability of the Maxwell – Boltzmann distribution to the population of the upper energy states. In this experiment, these states appear to be relatively well thermalized.

It is interesting to compare the results of this section to the results for the Ar atom excitation temperature. The vibrational temperature range of 8000 – 9000 K matches the electron (excitation) temperature range of 7000 – 9000 K, so the results are identical within experimental error. In addition, both studies found the corresponding temperatures to be independent of the applied voltage. Different trends are observed when comparing the time-resolved results. The electron excitation temperature is higher during the first 200 ns and lower in the later part of the discharge, while the vibrational temperature is lower during the first 200 ns and seems to increase slightly during the later part of the discharge. These weak trends may be rooted in the physical processes of the discharge or may be due to the experimental difficulties, but this should be further discussed later in

this work. The most significant is the fact that the spectroscopic analysis of the atomic line emission and molecular band spectra produced essentially the same values for excitation temperature of the selected transitions.

4.4.2.2.2. Summary of vibrational temperature

The vibrational excitation temperature for discharge in Ar bubbles has been determined using the vibrational bands of N_2 second positive system ($C^3\Pi_u - B^3\Pi_g$ transition). The $\Delta v=-1$ sequence with the strongest head (1 – 0) at 315.9 nm has been chosen for analysis. The maximum intensities at 315.93 nm, 313.6 nm, and 311.7 nm have been determined and the Boltzmann plot used to find the excitation temperature. The linear fits have regression coefficients of ~0.94 and the resulting temperatures range from 0.73 – 0.84 eV.

The results are as follows:

- The average temperature over the entire 1200 ns is 0.84+/-0.03 eV or 9000 K.
- The average temperature during the first 200 ns of the discharge is 0.73 +/- 0.08 eV or 8000 K.

4.4.2.3. Rotational temperature

4.4.2.3.1. Rotational Temperature Using OH emission

The geometry and electrical properties of the discharge in a gas bubble forbid any use of probes or other invasive techniques to assess the energies of the ions and other heavy species in the discharge. Spectroscopic methods continue to provide an alternative way to characterize the discharge. High resolution spectroscopy reveals the individual line structure of the vibrational bands due to the rotational sublevels.[1, 15] in each electronic vibrational state. Short lifetime and relatively small energy differences between the rotational sublevels usually result in the rotational state reaching

thermodynamic equilibrium with the translational motion of atoms and molecules of the gas. The assumption of thermodynamic equilibrium and therefore the applicability of the Boltzmann distribution may be checked again while simultaneously determining the rotational temperature by constructing a Boltzmann plot using the resolved line structure of the vibration-rotational bands. This approach is impossible since the apparatus function of the monochromator used in this study $\Delta\lambda$=0.15 nm is too high to produce high-resolution spectra.

Unresolved vibrational bands can also be used to assess the rotational temperature, either by using the global maxima of characteristic regions within partially resolved bands or by modeling the spectrum of an unresolved band and fitting it to the experimental spectrum. [14, 15, 16] The OH 306.4 nm $A^2\Sigma^+ - X^2\Pi$ system is partially resolved (Figure 4.4.1b and 4.4.9) and sensitive to changes in rotational temperature. As seen in Fig 4.4.9, it is easy to distinguish three regions in this band: 306.3 nm – 307.3 nm, 307.6 nm – 308.8 nm, and the region ahead of 308.9 nm. The global maxima of the first two regions are found and the ratio of the maximum intensity of the second region to that of the first is used to estimate rotational temperature.[16] The method is valid for ratios $R_2/R_1 > 0.6$ or temperatures below 3000 K, the condition that holds for the experiments described here. Spectra have been analyzed for applied voltages of 10, 12, 14, 16, 18 kV, for different time periods during the discharge, and for repeated trials under the same conditions. The results for R_2/R_1 for the various experimental situations are found in Table 4.4.6. The temperature is estimated by using the graph from Pellerin[18] for the appropriate apparatus function (Figure 4.4.10). The temperature estimate is only approximate but the ratio R_2/R_1 itself should indicate the trends in the temperature variation. The average temperature overall is approximately 1500 K with the lowest and the highest reaching about 1200 K and 2000 K, respectively. Rotational temperature, as evaluated by this method, appears lower during the earlier time in the discharge and higher later during the pulse.

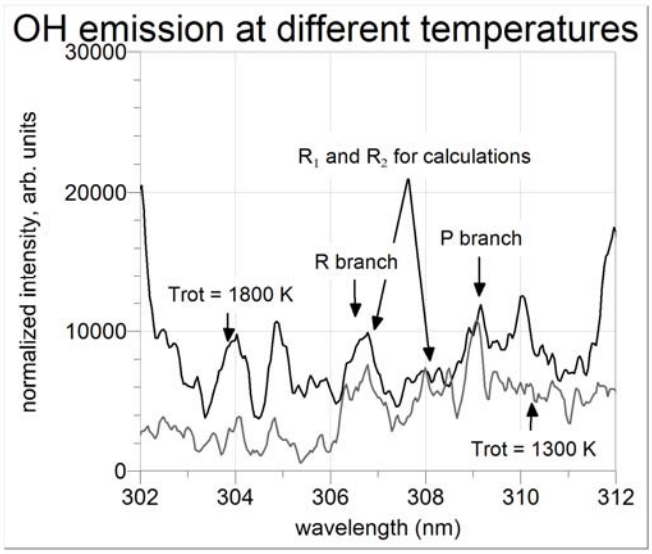

Figure 4.4.9 The two OH emission spectra shown here are normalized for the P branch emission. The spectra correspond to two different rotational temperatures. At higher temperatures, the R- branch emission increases relative to the other regions. Constructing intensity ratios that involve this branch gives information on the temperature trends.

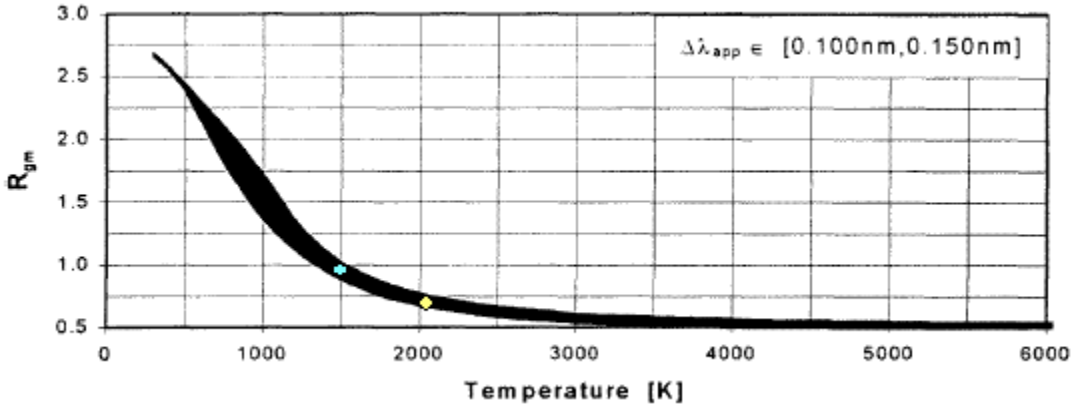

Figure 4.4.10 This figure is taken from Pellerin (1995). The graph shows the ratio of global maxima of partially resolved regions R_g/R_m as a function of temperature. R_2/R_1 is used in this experiment (as described in the text) and the highest and lowest experimental ratios are marked on the graph. From the graph, these ratios correspond to a temperature range of approximately 1500 – 2000 K.

Table 4.4.6 Summary of results for the rotational temperature using the OH emission band analysis R_2/R_1 ratio decreases with increasing rotational temperature

OH emission analysis				
repeated 10 kV pulses applied to the same bubble				
first 200 ns of the discharge				
trial # at 10kV	R1 global max, arb. units	R2 global max, arb. units	R2/R1	approx. Trot, K
1	3900	3800	0.97	
2	3400	2900	0.85	
3	3000	2429	0.81	
4	3300	3200	0.97	1300
AVERAGE			0.90	1200
ST. DEV.			0.08	
repeated 10 kV pulses applied to the same bubble				
entire 1200 ns of the voltage pulse				
trial # at 10kV	R1 global max, arb. units	R2 global max, arb. units	R2/R1	approx. Trot, K
1	12000	9000	0.75	
2	12700	8700	0.69	
3	12000	8238	0.69	
4	11000	8666	0.79	
5	11000	8500	0.77	
6	10770	7700	0.71	
AVERAGE			0.73	1700
ST. DEV.			0.04	
OH emission at different voltages				
first 200 ns of the discharge				
Voltage, kV	R1 global max, arb. units	R2 global max, arb. units	R2/R1	approx. Trot, K
10	3900	3800	0.97	
13	9300	6990	0.75	
14	3500	3184	0.91	
14	4200	3260	0.78	
16	4500	4400	0.98	
18	2000	1880	0.94	
AVERAGE			0.89	1400
ST. DEV.			0.10	
entire 1200 ns of the voltage pulse				
Voltage, kV	R1 global max, arb. units	R2 global max, arb. units	R2/R1	Trot, K
10	12000	9000	0.75	1700
13	3500	2604	0.74	
14	13700	10240	0.75	
16	21260	18530	0.87	
18	14520	12750	0.88	
18	5000	4088	0.82	1500
remaining 1000 ns after the first current pulse				
Voltage, kV	R1, arb. units	R2, arb. units	R2/R1	Trot, K
10	10320	6728	0.65	2000
13	10000	8030	0.80	
14	10000	7855	0.79	

4.4.2.3.2. Rotational Temperature Using N_2 Emission Bands

The OH band itself is sensitive to the temperature changes, but it is not well isolated and some known and unknown sources also emit light in this spectral region. For example, as seen in Figure 4.4.1b, the N_2 second positive system with the head band at 315.9 nm and degraded toward the higher energies encroaches on this region. Some unknown lines also appear in this region more or less prominently at times. Estimating the maximum of the 306.3 nm – 307.3 nm region caused difficulties since the maximum was taken over by what appears to be an FeI 306.72 nm line that could be a product of the stainless steel needle cathode. This method as used in this work provides only an estimate and does not verify the condition of thermal equilibrium.

The second method used to verify the results and to assert the applicability of thermal equilibrium involves modeling the spectrum from a chosen band from the N_2 second positive system, $C^3P_u - B^3P_g$. Since N_2 is an uninvited guest to the Ar bubble (although sometimes a welcome one), it is not easy to find a band that is present consistently in the spectrum, and is strong enough and isolated enough to prevent interference from other lines or bands. The 0 – 0 band with the peak at 337.13 nm is usually the strongest in the spectrum and it is a prominent feature in the spectrum shown in Figure 4.4.1c. It seems to be a good choice although some unidentified activity does seem to occur sometimes if the intensities of the N_2 emissions in the spectrum are low. The modeling program written in Visual Basic is provided by Dr. Kevin Martus, William Paterson University, Wayne, NJ. The program allows manual input of some band parameters such as the relative positions of the P, R, and Q branches, runs a minimization routine as a function of rotational temperature and returns the value of the temperature and the mean square error. The experimental and theoretical bands are normalized at the intensity maximum. Testing the program to sensitivity to temperature changes showed that in the temperature range of about 800 – 2000 K, changes of +/- 100 K did not affect the mean square error. For temperatures returned by the model this means a sensitivity of about 10%. A sample fit showing the theoretical and the experimental spectrum is found in Figure 4.4.11.

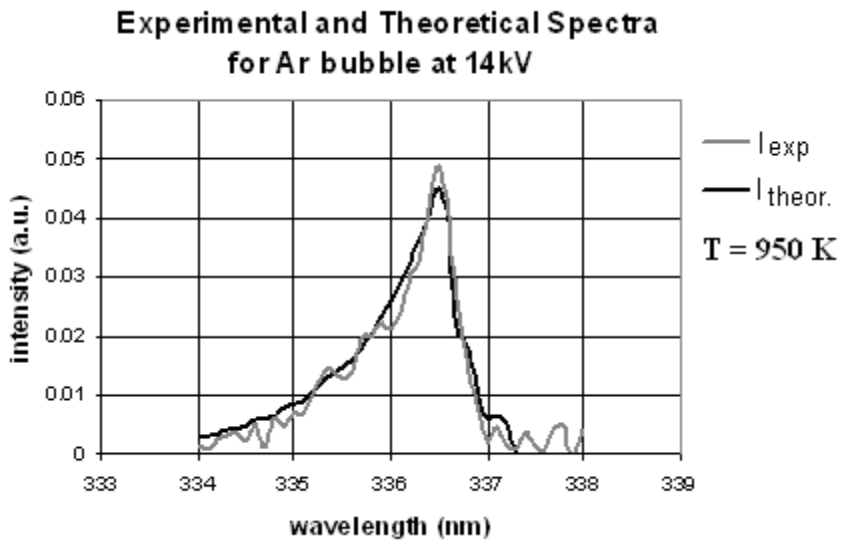

Figure 4.4.11. The graph shows the experimental spectrum of emission from Ar bubble at 14kV and the fitted theoretical spectrum. Theoretical spectrum is modeled for Trot = 950 K. The spectrum is taken with 1200 ns exposure and 100 accumulations. The RMSE of the fit is 0.0002 a.u. and the sensitivity of the fit to temperature changes is about 10%.

Spectra are fitted for various experimental conditions and the resulting temperatures are listed in Table 4.4.7. Repeated trials are reported for the applied voltage of 14 kV with the average rotational temperature of 1050 K. The repeated pulse application does not have an affect on the rotational temperature. The temperature is also not affected by the changes in the applied voltage. The results in Table 4.4.7b show that the average rotational temperature over the entire time of the discharge 1000 K is lower than the 1200 K average during the first 200 ns of the discharge, although the two values overlap within the experimental uncertainty of +/- 100 K. The overall results give rotational temperature in the range of 900 – 1300 K with the average of 1100 K.

The spectrum modeling technique returns a lower temperature value than the partially resolved band method with averages of 1100 K and 1500 K, respectively. Taken at face value this is a significant difference. The agreement is reasonable considering the difficult nature of the spectrum, the varying concentrations of N_2 as an impurity and OH as the product of the discharge affecting the intensities in the spectrum and hence the signal/noise level and the presence of various species, some unidentified. The rotational temperature of 1100 – 1500 K determined by these two methods is much lower than the

electron and vibrational temperatures of 7000 – 9000 K determined also by spectral analysis.

Table 4.4.7 Rotational temperature using N_2 2nd positive 0 - 0 band (peak at 337.13 nm)

(a)

From spectra taken during entire 1200 ns of the discharge at 14 kV	
Repeated trials	Rotational Temperature, K
1	1000
2	1200
3	900
4	1100
AVERAGE	1050

(b)

Rotational Temperature: Summary of the Results		
From spectra taken during:	entire 1200 ns of the discharge	first 200 ns of the discharge
Applied Voltage, kV	Rotational Temperature, K	Rotational Temperature, K
12	900	1200
14	1050	1200
16	1000	1100
18		1300
AVERAGE	1000	1200

Rotational Temperature: Summary

The rotational excitation temperature has been determined using two methods: taking the ratio of the global maxima of partially resolved bands within the OH 306.4 nm $A^2\Sigma^+ - X^2\Pi$ system and modeling emission in the 0 – 0 head band at 337.13 nm of the N_2 second positive system, $C^3P_u - B^3P_g$. The method using the OH band gives a higher temperature value than the modeling method. Results are as follows:

- The OH band method gives the overall average temperature of 1500+/-300 K, or ~0.13 eV. Rotational temperature evaluated by this method appears lower during the earlier time in the discharge and higher later during the pulse.
- The modeling of the N_2 second positive system 0-0 band gives the overall average of 1100+/-100 K or ~0.1 eV. The average over the entire time of the discharge 1000 K is lower than the 1200 K average during the first 200 ns of the discharge, although the two values overlap within the experimental uncertainty of +/- 100 K.

4.4.2.4 Electron Density

4.4.2.4.1. Line ratio approach for electron density estimate

The first estimate of the electron density in this discharge is obtained from the analysis of a current pulse (Figure 4.4.12). The charge transmitted by the first current pulse in a typical discharge is in the range of 0.5 – 0.7 μC. The size of the plasma channel is estimated (from the images) to be in the range of $2x10^{-3}$ – $5x10^{-3}$ cm^3. These values give a plasma density n_e on the order of 10^{14} cm^{-3}. This is a high density estimate that requires a degree of ionization of about 10^{-6}. The presence of ArII lines in the spectra provides evidence of electron collisions with Ar+ in the discharge and therefore supports the high electron density estimate.

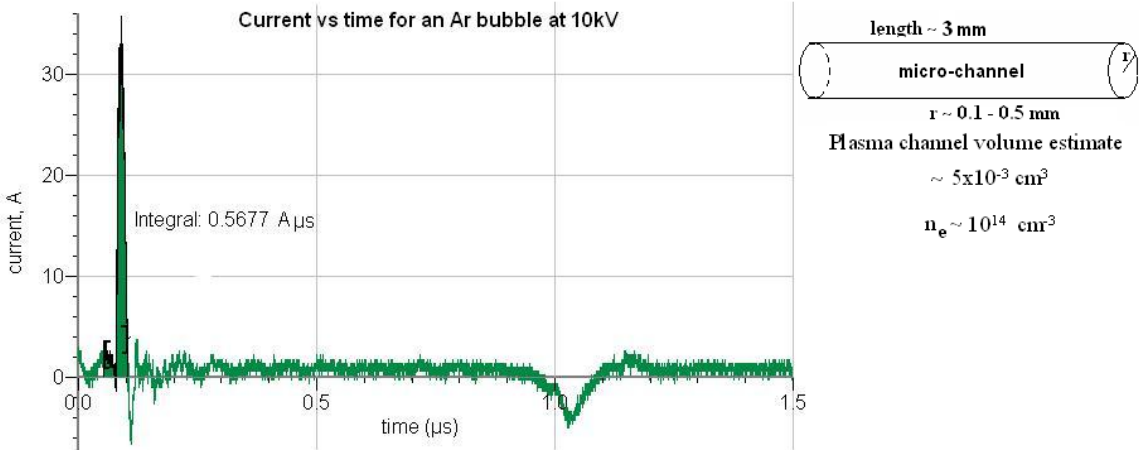

Figure 4.4.12 The graph shows a representative oscillogram used to compute the total charge transmitted during the first current pulse. The charge transmitted is in the range of 0.5 – 0.7 μC giving a plasma density estimate of 10^{14} cm^{-3}.

Electron impact excitation can by accomplished directly from ground state or by a two-step process through a metastable state. Schematically,

$$Ar + e \rightarrow Ar^* + e$$

or

$$Ar + e \rightarrow Ar^*_m + e \quad \text{followed by} \quad Ar^*_m + e \rightarrow Ar^* + e$$

For Ar, the minimum energy for excitation from ground state is ~11.5 eV. The observed strong Ar I emission lines (figure 4.4.1e – f) correspond to 4p → 4s transitions where the upper state energy is ~13 eV. The threshold energy for electron excitation of these levels from ground state is then ~13 eV, but the threshold energy for excitation from the metastable level is ~1.5 eV. The density of the excited levels then depends on the density of "fast" electrons for the levels excited from ground state, but the levels excited from the metastables depend on the number of "slow" electrons. Cross sections for excitation of the metastable levels into higher levels can be much higher than excitation from ground state particularly at high electron densities ($>10^{10}$ cm^{-3}). The Ar I 750.4 nm line is excited mainly from the ground state, and the 811.53 nm line is excited mainly from the metastable states. Since the line intensities depend on the number densities of the impacting electrons, the line intensity for the 811 nm line depends on the number of "slow" electrons and the line intensity of the 750 nm line depends on the number of "fast" electrons. The number of "slow" electrons is much greater than the number of "fast" ones and so the number of "slow" electrons is close to the total number of electrons in the plasma, or plasma density. In low density, low pressure discharges the line intensities of the 811 nm and 750 nm lines are often used to evaluate the changes in the electron number density.[20, 21] The applicability of this method is being explored in this study.

Integrated line intensities for the 811 nm and the 750 nm lines are determined for the various applied voltages and also for spectra taken during the first 200 ns of the discharge and during the entire duration of the voltage pulse. The data are collected from spectra such as shown in Figure 4.4.1e – f and integrated intensities are calculated from the line profiles. Individual intensities are averaged for three to five trials and ratios are computed taking the average intensity values for different voltages. Table 4.4.8 shows the results for 12 kV and 16 kV applied voltage. For comparison, the ratios are also shown for the 750 nm and the 751 nm lines used previously for the assessment of electron energies.

Table 4.4.8 Ratios of integrated line intensities are calculated for the 811.53 nm, 750.4 nm, and 751.5 nm Ar lines. All ratios are relative to the 750.4 nm line.

Time During the Applied Voltage Pulse:	First 200 ns	First 200 ns	Entire 1200 ns	Entire 1200 ns
Applied Voltage	Integrated Intensity Ratio I_{811}/I_{750}	Integrated Intensity Ratio I_{751}/I_{750}	Integrated Intensity Ratio I_{811}/I_{750}	Integrated Intensity Ratio I_{751}/I_{750}
12	1.40	ave 0.45	0.90	1.19
16	0.69	ave 0.45	0.75	0.94

The ratio of the intensity of the 811 nm line to that of the 750 nm decreases with applied voltage for both exposure times. Interpreting this ratio as indicating the increase in the electron density means that the electron density decreases with voltage, a trend that is in direct contradiction to previous measurements of the discharge current. The contradiction warrants a closer look at the reasons behind the interpretation of this line intensity ratio as the indicator of electron density.

The line intensities depend on the number densities of electrons, the number densities of Ar upper excited levels, and the rate coefficients for each transition. The ratio of the intensity of the 811 nm line to that of the 750 nm is given by[20, 21]:

$$\frac{I(ArI,\ 811\ nm)}{I(ArI,\ 750\ nm)} = a \cdot \left(\frac{K_{g\to 1} \cdot N_A \cdot N_{e,f} + N_{A,m} \cdot N_{e,s} \cdot K_{m\to 1}}{K_{g\to 2} \cdot N_A \cdot N_{e,f}} \right) \qquad 4.4.8$$

where the number densities of the slow and fast electrons are $N_{e,s}$ and $N_{e,f}$ ($N_{e,s} >> N_{e,f}$), K_m and K_g are the rate coefficients of the electron impact excitation from metastable and from ground states. N_A and $N_{A,m}$ are number densities of ground and metastable states of Ar atoms, and indexes 1 and 2 refer to the corresponding radiating states, and a is a proportionality constant. The numerator in 4.4.8 takes into account the excitation of the upper energy level for the 811 nm line by the fast electrons directly from ground state and by the slow electrons from the metastable intermediate state. The line intensity ratio varies with the changing density of the metastable states and the density of the slow and fast electrons. This expression can be written as

$$\frac{I(ArI,\,811\ nm)}{I(ArI,\,750\ nm)} = a \cdot \left(\frac{K_{g\to 1}}{K_{g\to 2}} + \frac{N_{A,m}}{N_A} \cdot \frac{N_{e,s}}{N_{e,f}} \cdot \frac{K_{m\to 1}}{K_{g\to 2}} \right) \qquad 4.4.9$$

Changing electron energy distribution affects the ratio of the excitation rate constants $K_{g\to 1}/K_{g\to 2}$. This change is very small since the levels 1 and 2 are close in energy (~13.2 eV and 13.5 eV). This was one of the main difficulties with using line ratios for finding the electron temperature. The line ratio depends on the ratio of the slow to fast electrons and on the density of the metastable states. If the energy distribution of the electrons remains constant under the experimental conditions then the line ratio can be used to determine the concentrations of metastables. On the other hand, if the concentration of metastables remains constant then the changes in the line intensity ratio indicate the changes in the ratio of slow to fast electrons $N_{e,s}/N_{e,f}$, indicating the changes in the electron energy distribution. The ratio of the metastable states to the Ar atom density is given by

$$\frac{N_{A,m}}{N_A} = \frac{N_{e,f} \cdot K_{g\to m}^{eff}}{k_d + N_{e,s} \cdot Q_e + N_A \cdot Q_A} \qquad 4.4.10$$

where the numerator describes populating the metastable level and the denominator takes care of destruction. The rate coefficient $K_{g\to m}^{eff}$ is an apparent rate constant that includes excitation into a metastable state from the ground level and cascading down into this level from higher levels. The population of metastable states decreases by diffusion out the plasma channel, and by relaxing collisions with electrons and neutral atoms.

In low density, low pressure plasmas, only the diffusion process plays an important role in reducing the population of metastable states. The expression for line intensity ratio can be simplified and becomes

$$\frac{I(ArI,\,811\ nm)}{I(ArI,\,750\ nm)} = a \cdot \left(\frac{K_{g\to 1}}{K_{g\to 2}} + \frac{N_{e,s} \cdot K_{m\to 1}}{k_d} \right) \qquad 4.4.11$$

illuminating the dependence on the density of the slow electrons Ne,s~Ne, essentially equal to the total density of electrons.

The time scale of this discharge (~100 – 200 ns), makes the diffusion process negligible. The high density of neutrals N_A and high plasma density (~$N_{e,s}$) make it impossible to ignore quenching effects. In this case, the line intensity ratio is given by

$$\frac{I(ArI,\,811\ nm)}{I(ArI,\,750\ nm)} = a \cdot \left(\frac{K_{g\to 1}}{K_{g\to 2}} + \frac{K^{eff}_{g\to m} \cdot N_{e,s}}{N_{e,s} \cdot Q_e + N_A \cdot Q_A} \cdot \frac{K_{m\to 1}}{K_{g\to 2}} \right) \qquad 4.4.12$$

where the slow electron density figures both in the excitation factor and in the quenching factor. There is no strong dependence on the slow electron density now, or sensitivity to the slow to fast density ratio. Instead the relationship can be dominated by quenching processes that decrease the intensity ratio.

In conclusion, the decrease in the ratio of the integrated intensities of the 811 nm and the 750 nm Ar I lines (shown in Table 4.4.8) can be attributed to the quenching effects decreasing the number density of the metastable Ar levels. For the high pressure, high density conditions of this experiment, plasma density is best estimated using the combined current and imaging data. This approach results in the estimate of $N_e \sim 10^{14} cm^{-3}$.

References:

1. G. Herzberg, Molecular Spectra and Molecular Structure, Vol. 1 (Spectra of Diatomic Molecules), Van Nostrand-Reinhold, New York, (1950).
2. R. Pearse, A. Gaydon, The Identification of Molecular Spectra, Chapman and Hall Ltd., London, (1976)
3. H. R. Griem, Principles of Plasma Spectroscopy, Cambridge University Press, (1997)
4. V. M. Donnelly, J. Phys. D : Appl. Phys. **37**,(2004)
5. A. Bogaerts, R. Gijbeis, J. Vicek, J. Appl. Phys., Vol. 84, No. 1, 121-136, (1998)
6. F J Gordillo-V´azquez, M Camero, C. G´omez-Aleixandre, Plasma Sources Sci. Technol. **15** (2006) 42–51
7. M. Cornett, M. George, B. Fries, H. Walde, L. Casson, Society of Vacuum Coaters, 45th Annual Technical Conference Proceedings (2002)
8. M. V. Malysheva, V. M. Donnelly, J. Vac. Sci. Technol. A **15**, No.3, (1997), 550 - 558
9. M. Hayashi, "Bibliography of Electron and Photon Cross Sections with Atoms and Molecules Published in the 20th Century - Argon", National Institute For Fusion Science, Report No. NIFS-DATA-72, Jan. 2003.
10. G. Raju, IEEE Transactions on Dielectrics and Electrical Insulation Vol. **11**, No. 4, 649- 674 (2004)
11. N. Sadeghia, D. W. Setser, A. Francis, U. Czarnetzki, and H. F. Do¨bele, J. Chem., Phys., Vol. **115**, No. 7 (2001) 3144-3154
12. M. Brown, B.Ganguly, A. Garscadden, Plasma Sources Sci. Technol. **11** (2002) 190–194

13. R. Hippler, H. Kersten, M. Schmidt, K.H. Schoenbach, Eds., Low Temperature Plasmas, Fundamentals, Technologies, Techniques, Vol. 1 und Vol. 2, Wiley-VCH: Berlin (2008)
14. Z. Jelenak, Z. Velikic, J. Bozin, Z. Petrovic, and B. Jelenkovic, Phys. Rev. E, **47**, No. 5, (1993), 3566-3573
15. K. H. Becker, U. Kogelschatz, K.H. Schoenbach, R. J. Barker, Non-Equilibrium Air Plasmas at Atmospheric Pressure, IoP Publishing, Bristol (2005)
16. A. Lafthus, P. Krupenie, J. Phys. Chem. Ref Data, Vol. **6**, No. 1. (1977).
17. N. Masoud, K. Martus, M. Figus, K. Becker, Contrib. Plasma Phys. **45**, No 1, 32-39 (2005)
18. M. Lieberman, A. Lichtenberg, Principles of Plasma Discharges and Materials Processing, New York, 1994
19. S. Pellerin, J. M. Cormier, F. Richard, K. Musiol, J. Chapelle, J. Phys. D. Appl. Phys.**29,** (1996),726-739
20. C.O. Laux, T. G. Spence, C.H. Kruger, R.N. Zare, Plasma Sources Sci. Technol.**12** (2003) 125-138
21. S. A. Moshkalyov, P. G. Steen, S. Gomez, W. G. Graham, Appl. Phys. Lett. Vol. **75**, No.3 (1999) 328-330

4.5. Discharge in Ar Bubbles: Discussion

Electrical discharges in an Ar bubble in water were generated in bubbles 2 – 8 mm in diameter surrounding a 0.1 mm in diameter, 0.5 mm-long, stainless steel needle and submerged in de-ionized water. In this arrangement the needle serves as the cathode with voltage pulses of -5 to -20 kV, 1μs in duration applied to the needle either as single shots or at a rate of 1 Hz (essentially single shots). A stainless steel disk anode is submerged in the water at a distance of 16 mm from the needle. About 1 cm of water separates the bubble from the anode. The water provides a dielectric barrier insulating the anode and allowing charge accumulation on the surface of the water. Previous estimates treating the water-bubble system as two capacitors connected in series (Figure 4.5.1), and the field plot shown here (Figure 4.5.2) give a negligible voltage drop across the water compared to the voltage drop across the bubble. For example, an applied voltage of 8 kV results in a negligible 12 V across the water prior to discharge. For the voltages and time scales in this investigation, water works as a dielectric barrier and limits electrical breakdown to the gas bubble. Electrical discharge occurs in the Ar bubble and the charge gets deposited on the bubble surface as it would on the surface of a solid dielectric material.

For the distances and dimensions given above, an applied negative voltage greater than 8 kV results in small, thin discharges visible in the bubble. The discharge appears brighter for higher voltages and bigger bubbles. The bubble visibly vibrates with each stroke but most of the time maintains its shape and position. The stability of the bubble makes it possible to observe repeated discharges in the same bubble. The discharge has

been investigated using time-resolved electrical measurements and optical emission measurements, both spectroscopic and those using band pass optical filters. These measurements have been analyzed and lend estimates of the discharge parameters, current, charge transferred, optical emission decay constants, electron temperature (excitation temperature for atomic transitions), and vibrational and rotational molecular excitation temperatures.

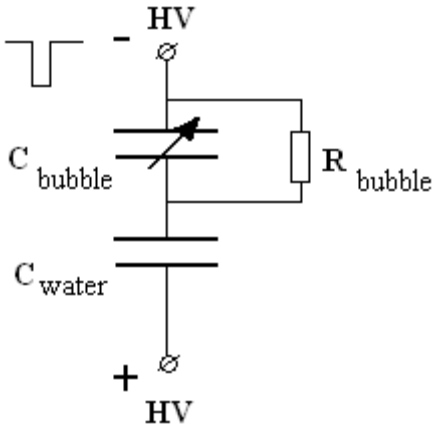

Figure 4.5.1 A schematic diagram of a bubble-water combination is shown. The bubble is represented as a variable capacitor that changes its properties and becomes conductive during discharge

The discharge regime and parameters are summarized in Table 4.5.1. The discharge parameters for a dielectric barrier discharge[4] and two other types of discharge are included for comparison. For applied voltages of 8 – 18 kV, the discharge in the bubble has an average 10 μJ of energy per pulse, transfers an average of 1 nC of charge per pulse, and reaches the peak current in the range of 25 – 60 A. Overall, the combined evidence indicates that the discharge varies both in time and in space, has high electron

density, low electron energy, and that there is an imbalance between the gas, rotational and vibrational temperatures.

Table 4.5.1 Discharge regimes and characteristics for the discharge in Ar bubbles investigated here and for three examples of high pressure discharges in non-uniform field. [2, 4]

Discharge conditions and parameters:	Discharge in Ar bubble	Random Filament DBD	Spark	Corona
Gas	Ar	air or O_2	air	air
Pressure	1 atm	1 atm	1 atm	1 atm
Distance	~ 5 mm	1 mm	0.1 – 10^2 m	
pd	300 – 400 Torr*cm	<100 Torr*cm	>4000 Torr*cm	
Filament radius	~0.1 – 0.5 mm	~0.1 mm	~01. – 10 mm	
Peak current	25 – 60 A	0.1 A	10^4 – 10^5A	1 – 100 μA
Peak current density	~ 500 – 1000 A/cm^2	~ 100 – 1000 A/cm^2	10^4 A/cm^2	
Charge transferred	0.5 – 1.0 μC/first pulse	0.1 – 1.0 nC/filament		
Current pulse duration	~50 ns (first pulse)	1 – 10 ns/filament		
Electron density	~10^{14} cm^{-3}	~10^{14} – 10^{15} cm^{-3}	~10^{16} – 10^{17} cm^{-3}	
Electron temperature	~ 7000 – 9000 K 0.6 – 0.8 eV	1 – 10 eV	1 – 10 eV	
Vibrational temperature	~ 8000 – 9000 K ~ 0.7 – 0.8 eV	~3000 K	20000 K	
Rotational temperature	1100 – 1500 K 0.10 – 0.14 eV	~300 – 500 K		

4.5.1 Discharge Initiation

The electric field strength in the bubble is greatest at the needle negative electrode (Figure 4.5.2). The discharge therefore starts in the cathode region and it is initiated by a Townsend mechanism. The observed initial delay of the first current pulse (Fig. 4.1.1)

corresponds to the random "waiting" time for the appearance of the initial seed electrons. This initial delay disappears at higher voltages (Fig. 4.1.4). Usually in an inert gas

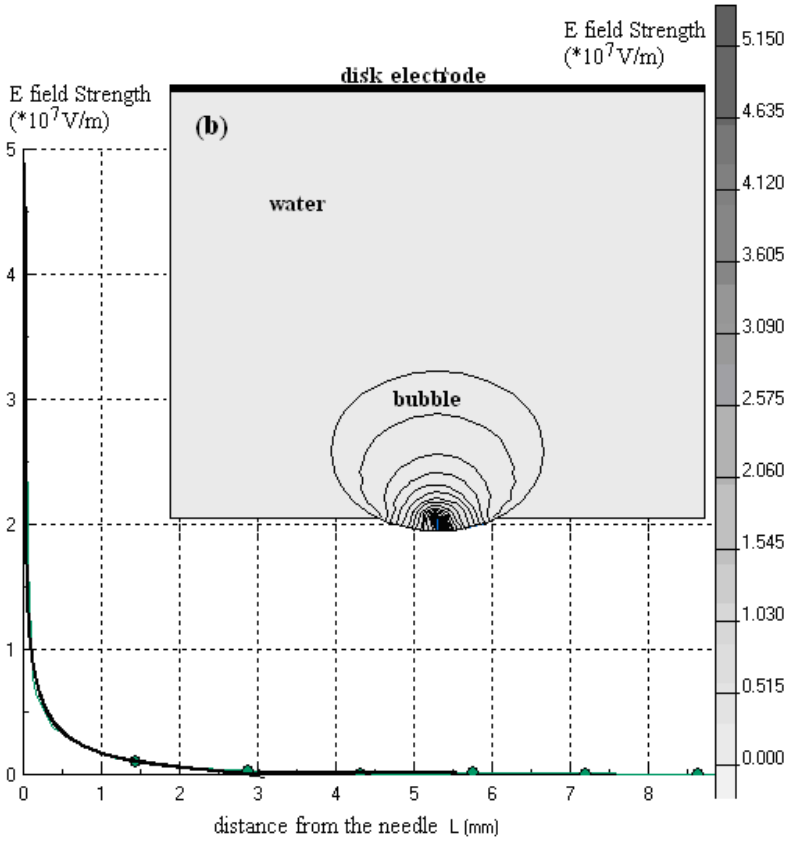

Figure 4.5.2. An electrostatic field map using Quick Field (Terra Analysis) software package. The shaded field map is inverted; here the needle is at the bottom. The graph shows the electric field strength as a function of the distance from the needle. The water surface is reached at about the 4 mm mark and the field is practically zero thereafter.

discharge, these seed electrons are produced by the outside (cosmic ray) radiation, a mechanism completely independent of the experimental conditions. Here the mechanism of discharge initiation seems to be field dependent. Two sources of seed electrons may play a role here, detachment from negative ions and field emission from the cathode. In this experiment, in addition to argon gas, the bubble also contains water vapor and some amount of air associated with the presence of nitrogen and oxygen. In this case, background charge usually exists as O_2^- or hydrated clusters of this molecular ion. A seed

electron may be provided by detaching the extra electron from O_2^-. Electron detachment occurs by collisions with neutral atoms or molecules in the presence of an electric field. Field electron emission from the cathode can also provide the seed electrons and depends strongly on the applied field. For a metal electrode an appreciable electron release occurs at electric fields ~10^6 V/cm.[1] This is value is greater than the field strengths in Figure 4.5.2, but the values in this field plot are based on considering the needle as a solid electrode of the needle's diameter. In reality, the walls of the needle provide a much sharper edge than considered in the QuickField® model. It is realistic to expect both, electron detachment from negative ions and field electron emission from the cathode, to play an important role in providing the seed electrons needed to start the discharge process. Both of these mechanisms can lead to a diminishing delay with increasing voltage as seen in Fig. 4.1.4.

4.5.2 Discharge Propagation

Once the seed electrons become available, electron avalanches start building in the region of the high electric field around the needle electrode (Figure 4.5.3). The images (taken at 5 ns intervals with 5 ns exposure time) show that the region around the tip of the needle is the first to start glowing (Fig 4.3.3). Once the avalanches develop, the discharge has the choice of establishing an ionized region by allowing multiple avalanches to reach the bubble wall or proceeding by streamer development. The Meek criterion establishes the possibility of developing a streamer.[1, 2] The condition means that the avalanches produce a high enough degree of ionization that the outside field is substantially distorted. Electrons moving at fast velocities away from the cathode produce

their own electric field. If this field matches or surpasses the value of the outside field, the result is a moving "cathode" and the new avalanches develop ahead of the moving electrons essentially a moving ionization front. Mathematically, this argument is expressed as follows. The number of electrons produced in a space x_1 to x_2 in the outside electric field E is given by

$$N_e = \int_{x_1}^{x_2} \alpha(E)\, dx \approx 3 \cdot 10^8 cm^{-3} \qquad 4.5.1$$

where $\alpha(E)$ is the ionization rate in the gas at the applied field E. It is an exponential function of applied field

$$\alpha(E) = A \cdot p \cdot \exp\left(-\frac{B \cdot p}{E}\right) \qquad 4.5.2$$

Where E is the applied field in V/cm, p is the pressure in Torr, and for Ar, A = 12 Torr/cm, B = 180 V/(cmTorr). [1,2] Meek criterion for the field of the new electrons,

$$E_a = \frac{e}{4\,\pi\varepsilon_o r_a^{\,2}} \cdot \exp\left(\alpha \cdot \left(\frac{E_o}{p}\right) \cdot x\right) \approx E_o \qquad 4.5.3$$

Simplified, this can be written as

$$\alpha \cdot \left(\frac{E_o}{p}\right) \cdot d = \ln\left(\frac{4\,\pi\varepsilon_o \cdot E_o}{e \cdot \alpha^2}\right) \approx 20 \qquad 4.5.4$$

where d is the distance needed to meet this condition. Taking the electric field to be the average at a distance of 0.5 mm – 1.0 mm from the needle, $E_o \sim 10^4$ V/cm, estimating a(E) using the values for Ar and substituting into the Meek condition, gives an estimate for d. The resulting d = 1.4 mm < 4 is an overestimate, since the field is stronger closer to the needle and it is really equation 4.5.1 that needs to be satisfied. This means that discharge is likely to propagate via an anode-directed streamer. This conclusion is

consistent with a high and highly non-uniform electric field and the high density estimates from the data on charge transfer.

The speed of propagation of the discharge could provide a nice experimental verification of this possibility. Due to the field enhancement, the streamer propagates at speeds faster than the drift velocity of the electrons, usually 10^8 cm/s versus 10^7 cm/s for the drift velocity in the outside field. [1,2] Using the images of the discharge taken with 5 ns second exposure time, it is possible to roughly estimate the time it takes the discharge to reach the surface of the bubble about 4 – 5 mm away. The time is estimated as about 10 ns from the 3D plots of consecutive images of the Ar discharge. The current oscillograms show the current in the first peak rising for about 5 – 10 ns. Assuming that the electrons slow down once the front reaches the surface of the water, this time is another estimate of propagation time. The time estimates agree quite well but the resulting speed of about $5x10^7$ cm/s is exactly between the two values listed above. The main source of error in this estimate is the value for the distance to the wall. The effect of the bubble shape, image resolution, and reflected light make distance measurements difficult to carry out. In addition, each image is of a different discharge event that does not propagate along the same path. The distance measurements from the images introduce a margin of error of ~40%. Again, although not unequivocally proven by the data, the streamer mechanism is clearly expected for the conditions in the Ar bubble in this study.

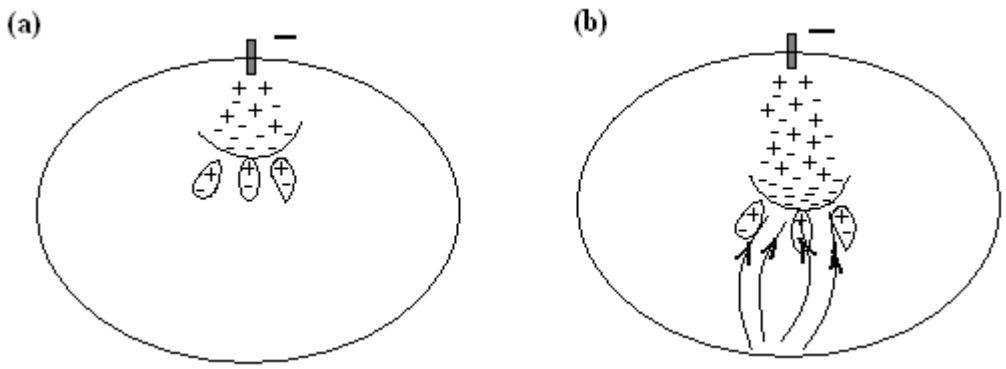

Figure 4.5.3 Propagation and the electric field around the streamer head.

4.5.3 Plasma Channel

The propagating streamer has a thin charged region at its head followed by a channel where the electrons are trapped by the positive ions, a quasi-neutral plasma channel. The width of this channel can be (very roughly again) estimated from the images to be ~ 0.5 mm (approximately 4 – 5 pixels). This bright channel can possibly contain plasma only if the size of this channel exceeds the characteristic Debye length of the plasma. Debye length can be conveniently estimated from the following numerical formula[2]:

$$r_D = 742 \cdot \sqrt{\frac{T_e}{n_e}} \qquad 4.5.5$$

where r_D is Debye length in cm, T_e is the electron temperature in eV, and n_e is electron density in cm^{-3}. For the electron temperature $T_e \sim 0.8$ eV and electron density $n_e \sim 10^{14}$ cm^{-3} obtained experimentally in this investigation (section 4.4), Debye length is $r_D \sim 0.7\mu m$. The Debye length is much shorter than the ~0.5 mm size of the channel. This means that quasi-neutrality can be established in the streamer channel. The emerging

picture is then of a channel with well thermalized, cooler electrons (the fast ones have run ahead of this region). This region is shielded from the field of the needle by the positive ions left behind and the field here is low.

Once the head of the streamer reaches the surface of the water, the electrons are deposited on the water surface and the current decreases. A bright area is on the bubble wall that is visible in the images and the corresponding 3-D graphs. According to the images, the charge spreads along the surface over a region a couple of times greater than the size of the column. For some time after this, the images show three distinct regions in the bubble: the brightly glowing region around the needle, a darker but glowing channel through the gas, and a glowing region at the water surface. These resemble the regions of a glow discharge, except the electrons cannot sink into the anode and are deposited on the surface instead.

Once the charge is deposited, the field intensity decreases and the current drops. The average time for the current to drop is about the same as the time for current to rise, ~10 ns. The current drops long before the images dim.

For the Ar lines examined (Section 4.2), the measured optical emission decay times are greater than the radiative lifetimes of the corresponding transitions. The measured decay times in three 10 nm-wide optical ranges centered on the 750, 760, and 810 nm wavelengths are from 30 to 100 ns compared to 22.7 – 40.82 ns radiative lifetimes of the relevant Ar lines. See Table 4.2.2 for details. These measured decay times increase with increasing applied voltage. At atmospheric pressure, gas is dominated by collision processes and collisional quenching of excited stated is expected to play a major role in the resulting optical emission. If decay is exponential then decay constant τ_d^{-1} is

equal to the sum of the radiative decay τ_r^{-1} and quenching k_Q by collisions with various species,

$$\tau_d^{-1} = \tau_r^{-1} + k_{Q.} \qquad 4.5.6$$

Quenching therefore only decreases decay time τ_d. This description of the emission decay process applies if excitation into the upper state of the radiating transition is not significant and the processes being observed are those involved in depopulating the upper state. Observation of decay time longer than radiative lifetime means that excitation processes can not be ignored. The observed processes must be dominated by changes in excitation; populating the upper states is still an important factor in the observed emission. This explains not only the longer decay times, but also their dependence on the applied voltage. Observed evolution of optical emission appears to follow the decay of plasma. At high pressure, plasma decays by bulk recombination processes. In a complex mixture of gasses many recombination processes are taking place (for example, ion-ion recombination, dissociative recombination, and three body collisions), but electron-ion recombination is likely to dominate. For a plasma density $n_e \sim 10^{14}$ cm^3 and recombination coefficient $\beta \sim 10^{-7}$ cm^3/s, this process has the characteristic decay time $\tau = (\beta n_e)^{-1} \sim 100$ ns. [1] This time is in general agreement with the observed decay rates.

The OH emission decay data do not follow the trends described above. In fact, the measured decay time for OH ($A^2\Sigma^+$ - $X^2\Pi$) transition is 31.9 +/- 7.7 ns, more than an order of magnitude shorter than the radiative lifetime of 686 +/-70 ns [2] for this transition. This behavior is due to the combined effect of the long radiative lifetime with high collision cross section for the OH radical. In other words, many collisions can occur and do during the 686 ns lifetime of the $A^2\Sigma^+$ state.

This discussion leads to a conclusion that plasma continues to exist in the bubble after the current flow stops.

The electron temperature is determined from spectra taken with a 1200 ns exposure, that therefore include the light emitted during the earlier stages of the discharge and during the later stages when a bright plasma channel is established in the bubble. The result is a temperature of 0.6 – 0.8 eV (table 4.5.1). The electron temperature determined from the spectra is determined assuming Maxwellian distribution of electron energy and therefore missing any possible fast beam-type electrons. It seems reasonable that this temperature corresponds to the electron temperature in the plasma channel. These results do not exclude the possible presence of high energy electrons at some stages and/or in some areas in the bubble. Experimental results show that the vibrational excitation temperature (0.7 – 0.8 eV) is about the same as the electron temperature. This seems reasonable considering that electron impact excitation is the dominant mechanism for exciting vibrational states. Rotational temperature measurements indicate gas heating up to 1100 – 1500 K. The length of the voltage pulse allows the discharge to extinguish itself, first by choking the electric field in the channel and then by dissipation of the energy of charged particles in the channel through collisions. This means that the discharge has ample time to deposit its energy. The increase in the gas temperature under these conditions is not surprising. The discharge channel presents a picture of collision-dominated plasma with high electron density, low electron temperature, moderate gas heating, and highly effective energy transfer to the molecular vibrational states.

A series of imaging and spectroscopic studies have been conducted using sequential gating, taking spectra and images in time steps ranging from 5ns to 200 ns.

These studies confirm that the needle starts glowing first, the discharge then propagates within about 5-10 ns reaching the bubble wall, a narrow channel then glows for some time and is then extinguished in about ~200 ns. There is usually no light in the bulk of the bubble ~400 ns prior to the drop of the applied voltage. The channel decay time is consistent with bulk recombination for the plasma density ~10^{14} cm^3.

4.5.5 Needle Region

The images show the bright channel in the bubble gas gets dark first, followed by the glowing region on the bubble wall and then by the needle. The needle region does not seem to extinguish completely at any time during the voltage pulse. Given the high fields in the region around the tip of the needle, a corona-type region may be established around the tip of the needle and continue operating when the field in most of the discharge channel is extinguished. Field plots using QuickField® (Figure 4.5.2) show that deposition of a charge of the order of 1 nC at the surface of the bubble extinguishes the field up to a distance of about 2 mm from the needle. At distances <2 mm the field remains unchanged if the local charge density around the needle is ignored. This shows that the needle region can operate essentially independently of the rest of the discharge channel. A large potential gradient exists in this region and the needle needs to provide electrons for the continued operation of this region. These electrons can reach high energies due to the strong fields in the immediate region around the needle. Farther from the needle, the positive ions shield this area from the remaining plasma channel.

The spectra in the 750 nm region taken during the initial stages of the discharge show that the intensity ratio between the 750 nm and the 751 nm lines does not correspond to Maxwell's energy distribution for electrons. This intensity ratio may be due to high energy electrons. This interpretation is supported by the cross section data for the upper levels of these transitions[9]. The intensity ratio changes dramatically during the later time.

Other spectroscopic evidence of two types of electrons, the high energy beam-like electrons in the needle region and therefore at the start of the discharge process, and the lower energy well-thermalized electrons in the plasma channel, comes from the disappearing nitrogen molecular bands. These bands have high excitation energy and are strong in the spectra taken during the first 200 ns of the discharge and all but disappear at the later times (Fig 4.4.1b, c and Figure 5.2.3).

This supports the idea of a region with high potential drop around the needle electrode producing high energy electrons. These electrons move out of the area leaving the positive ions shielding the needle region. Due to the electrons emitted from the needle, the process can be repeated resulting in an active region around the needle.

4.5.6 Remaining times and places

The discharge dims once the charge is deposited on the surface of the bubble. The surface effects are significant for this discharge and may play a crucial role in formation of OH radicals and other species. These effects are not addressed in this study and warrant a separate investigation.

At the end of the voltage pulse, as the voltage drops below a certain level the discharge is reignited. The fact that the voltage does not drop to zero prior to the initiation of the reverse pulse and the lower amplitude of the current indicate that a residual charge remains in the channel. The proof could come from the images showing the discharge taking the same path. The images do seem to provide this evidence, although extracting it is not easy since the successive images correspond to new discharge pulses.

At the end of the voltage pulse, the current pulse is much broader. Many ions and radicals have been produced in the bubble, so the slowing down of the current growth can be attributed to significant attachment processes that slow down the avalanche development.

The next voltage pulse comes almost a full second after the previous discharge process is extinguished. The long time between the pulses insures the next discharge to be a distinct process with almost no connection to the previous event. The only lingering effect is the increase in water vapor content and the presence of chemical species generated by the previous discharge, such as O, O_3, O_2, H, and possibly other unaccounted for specimens. The presence of these species slows the current rise and the resulting current pulse is much wider than the first pulse. The width of the pulse increases with the number of pulse repetitions.

4.5.7 Summary

- Two types of electrons exist in this discharge: fast beam-like electrons and slow thermalized electrons in the plasma channel.
- An active discharge region is established around the needle where the discharge activity continues through the entire time of the voltage pulse.
- The discharge propagates from the needle by a streamer mechanism taking ~10 ns to do so.
- A plasma channel is established in the bubble where the conditions of quasi-neutrality are satisfied.
- The energy of the thermal electrons is ~0.8 eV.
- The plasma is collisional as determined by the OH decay times
- The vibrational excitation temperature is of the same order as the electron temperature ~0.9 eV.
- The rotational excitation temperature is ~1000 K (0.1 eV) and indicates gas heating in the channel.
- Water serves as a dielectric barrier for the field strength and time scales of this experiment, 1 μs.
- The charge is deposited on the water surface and spreads over an area a few times greater than the width of the discharge channel.
- The plasma channel is extinguished by the charge deposited on the water surface.
- The reverse discharge process occurs when the applied voltage begins to drop.

- The reverse process indicates charge carrier and active species accumulation in the channel.
- A new voltage pulse applied one second later proceeds as an entirely new process. The bubble has no memory of the previous process except for an increase in water vapor content and some long-lived chemical species, such as O, O_3, O_2, H produced by the discharge process.

References:

1. Yu. Raizer, Gas Discharge Physics, Springer-Verlag, New York, (1997)
2. A.Fridman, L. Kennedy, Plasma Physics and Engineering, Taylor & Francis, (2004)
3. M. Lieberman, A. Lichtenberg, Principles of Plasma Discharges and Materials Processing, John Wiley & Sons, Inc., New York, (1994)
4. K. H. Becker, U. Kogelschatz, K. H. Schoenbach, R. J. Barker, Non-Equilibrium Air Plasmas at Atmospheric Pressure, Institute of Physics Publishing, Philadelphia, 2005
5. B. Eliasson, M. Hirth, U. Kogelschatz, J. Phys. D. Appl. Phys. 20(1987) 1421-1437
6. A. Bogaerts, R. Gijbeis, J. Vicek, J. Appl. Phys. Vol. 84, No. 1 (1998) 121-136
7. K. Kano, M. Suzuki, H. Akatsuka, Plasma Sources Sci. Technol. 9 (2000) 314-322
8. A. Fridman, A. Chirokov, A. Gutsol, , J. Phys. D. Appl. Phys. 38 (2005) R1-R24

5. The Investigation of the Discharge in O_2 bubbles

Oxygen and air bubbles have been investigated briefly because of their general interest for application purposes.[1-7] These two gases can also aid the investigation of the discharge in a bubble in a more fundamental way. Pure argon has an extremely low electron affinity and so electron attachment processes are negligible in an Ar plasma, but an Ar bubble in this investigation has varying amounts of electronegative gasses present, ex. O_2, H_2O. The amount of these gasses increases with repeated discharges in the same bubble and the discharge process is affected. Comparing the results for oxygen, argon, and air can provide an additional insight into the discharge process in Ar bubbles in water. The results of the investigation of the discharge in oxygen bubbles and in air bubbles are presented below and compared to the results for Ar bubbles.

5.1. Electrical characteristics of the discharge in O_2 bubbles

The first observation made working with air and oxygen bubbles is the higher starting voltage for these discharges. Using the same distance between the electrodes and controlling the size of the bubble as well as possible, all starting voltages recorded are greater than 10 kV as opposed to 7.4 kV for the Ar bubble. In addition, the starting voltage depends on the polarity of the voltage applied to the needle. In Ar, all experiments are conducted with the needle serving as the negative cathode. Both positive and negative polarities are investigated for air and oxygen bubbles. The starting voltage is lower for positive polarity for both air and oxygen, but the effect is much less pronounced

in air than in oxygen. The geometry of the electrical connections to the experimental chamber is different for positive polarity. The change in length and relative configuration of the wiring changes the overall impedance for the pulse-forming network. In addition, greater amount of heating of the tie-down resistors also affected the matching impedance. These factors lead to the distortion of the voltage pulse. To avoid this affect, the highest voltage used is limited to 18 – 20 kV. The applied voltages investigated are 12, 14, 16, and 18 kV.

Figures 5.1.1 and 5.1.2 show the voltage and current oscillograms for the discharges in Ar, O_2 and air for negative potential on the needle and for positive potential on the needle. The sample results presented in the figure for a comparative overview are taken from the characteristics of the discharges at different voltages. The reason for choosing these voltages is that they correspond to roughly similar overvoltages for these bubbles. Note that the current scale is different in different graphs and so may give an appearance of different levels of noise, although the absolute noise level remains the same. The first overall look at the oscillograms immediately reveals some differences and similarities. The reverse current peak is still present, water working as a dielectric barrier. The most glaring difference is the absence (under any conditions) of the sharp high current peak so conspicuous in Ar discharge and lower overall currents. Air is the closest to having the high first current peak but it resembles Ar peaks after the bubble is subjected to a series of repeated shots. Air has a higher percentage of electronegative gasses initially present than Ar bubbles and so slower current build up may be expected.

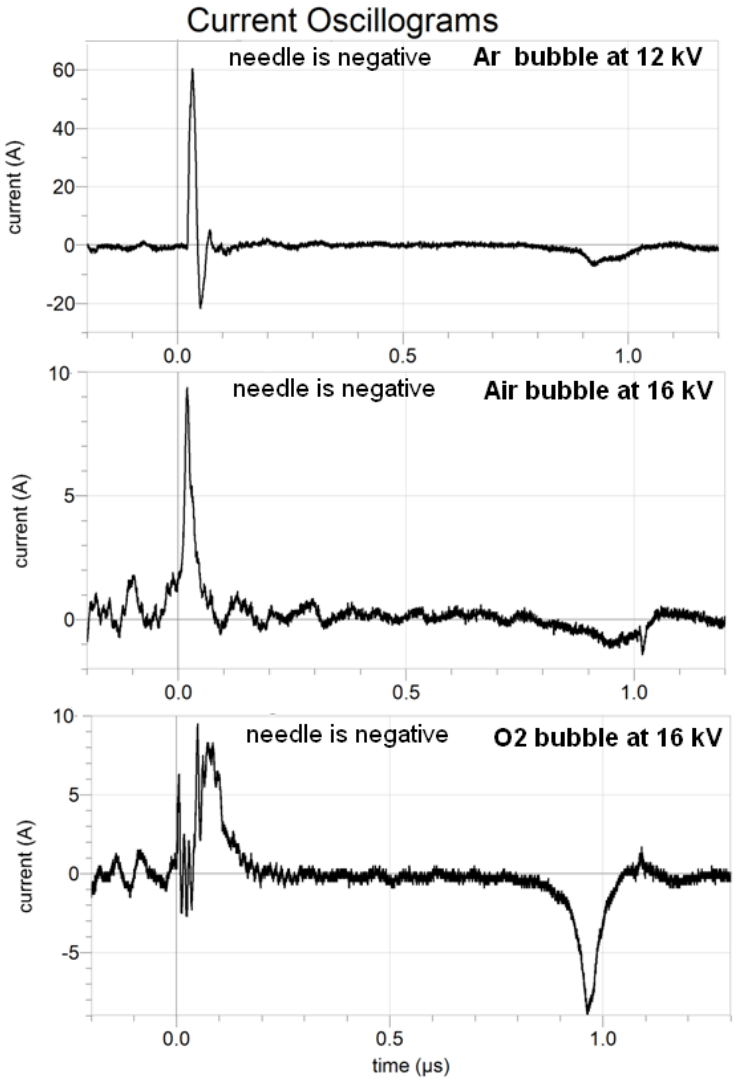

Figure 5.1.1 The graphs show current oscillograms for Ar, oxygen, and air bubbles. The needle is at a negative voltage in all three cases.

The current peak is wider in O_2 bubbles than in Ar and air, and here it is preceded by repeated short pulses. Changing the polarity of the needle does not have any significant effect on the oscillograms of the discharge in either air or oxygen. In oxygen, the preliminary pulses are more pronounced, and in both media repeated current pulses during one voltage pulse occur more frequently. Starting voltage is lower with positive voltage applied to the needle, and so the current is higher for the same applied voltage.

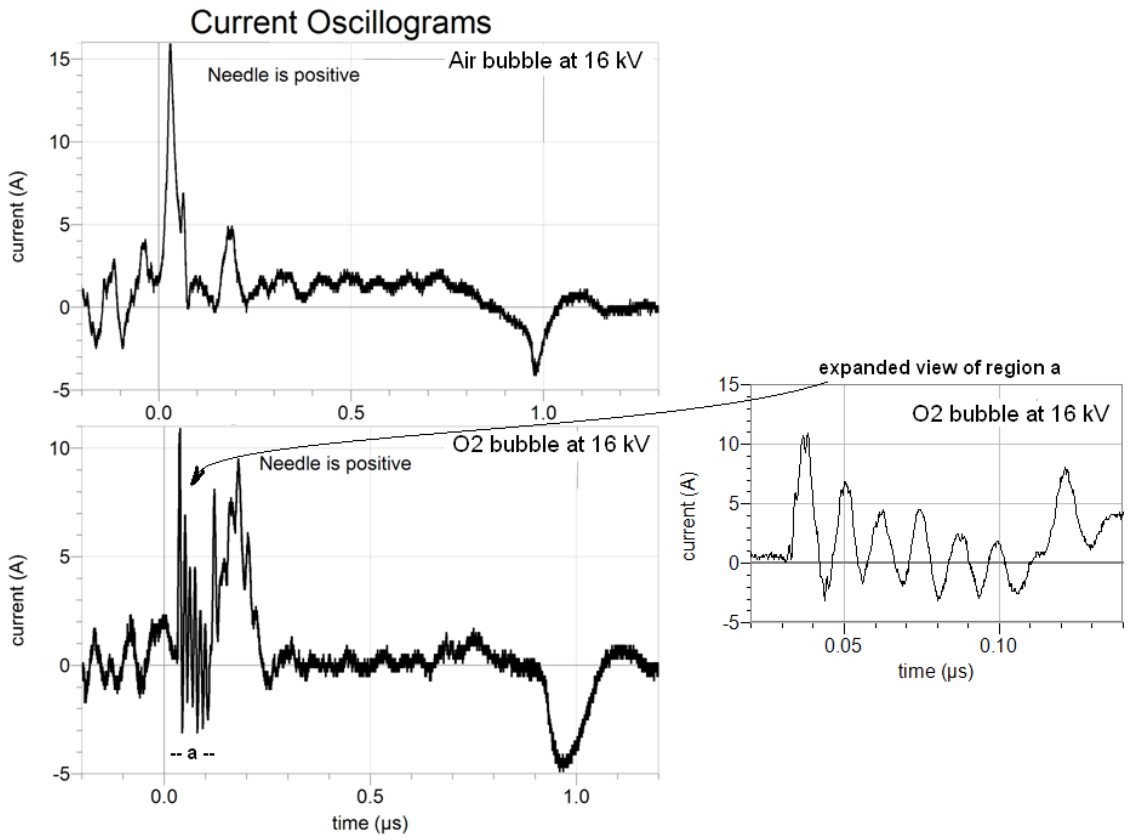

Figure 5.1.2 The graphs show current oscillograms for air (top) and oxygen (bottom) bubbles. The needle is at a positive voltage in both cases. The figure on the right shows an expanded view of the first set of short current pulses on the oxygen oscillograms (marked a).

A more detailed look at the fast pulses preceding the first extended current pulse (Figure 5.1.2 inset) reveals pulses regular in duration and repeated periodically. The duration of each pulse is 10 +/- 1ns. Taking the area under the first pulse gives a charge build up by each pulse as 50 +/- 10 nC. The duration of the pulse and the number of charged particles generated, ~10^{11} for the charge build-up just stated, correspond to the values expected for a single electron avalanche at atmospheric pressure.[8, 10] These pulses repeat, decrease in magnitude and stop, then restart after some time. (See more detailed information about the current in oxygen bubbles in Table 5.1.1). If the short pulses do not restart and do not build up into a more significant current pulse of longer duration, then no reverse current

pulse is present (Figure 5.1.3 a). This means there is no significant charge deposited on the surface of the bubble. Individual avalanches are most likely to get extinguished by electron attachment and do not produce a conductive channel to the bubble wall. A build up of avalanches is needed to create a conductive channel passing the current to the bubble wall. Once the avalanches build up sufficiently to result in a discharge current to the wall, the reverse pulse also appears at the end of the voltage pulse (Figure 5.1.3 b).

Table 5.1.1 A sample data analysis table for oxygen bubbles. The table contains information on charge transfer, charged particle generation, and the resulting density estimates.

Analysis of current oscillograms for Oxygen bubbles															
Needle polarity	Applied Voltage, kV	Duration of first peak, ns	First peak max, A	First peak charge, nC	electron number, Ne	Small peaks net charge, nC	First wide current peak max, A	Duration first wide peak, ns	Charge first wide peak, nC	electron number, Ne	Reverse current peak max, A	Duration reverse current peak, ns	Reverse current peak charge, nC	Total net current, A	**electron density, cm-3**
positive	12	10	8.4	37.89	2.4E+11	25.00	4	170	334.7	2.1E+12	-4	160	317.9	-0.254	4.E+14
positive	14	10	9.6	42.82	2.7E+11	76.00	9.1	100	579.9	3.6E+12	-5.1	170	303.7	0.5906	7.E+14
positive	16	10	12.2	60.11	3.8E+11	110.00	9.5	120	565.5	3.5E+12	-4.7	160	406	0.388	7.E+14
positive	16	10	13.4	63.54	4.0E+11	68.00	8.6	116	519	3.2E+12	-4.6	184	415.5	0.2451	6.E+14
positive	16	10	10.82	59.94	3.7E+11	64.00	9.09	128	566	3.5E+12	-4.5	160	409.9	0.2316	7.E+14
positive	18	10	14.3	37.9	2.4E+11	60.00	19.7	62	790.9	4.9E+12	-5.3	155	478.4	0.5777	1.E+15
negative	16	10	9.5	69	4.3E+11		8.1	140	544	3.4E+12	-8.9	250	590	0.1168	7.E+14

The time period between the individual avalanches and the discharge current decreases as the voltage increases. Once the over voltage is sufficiently high to insure that ionization outnumbers attachment from the start, the discharge current is able to build up almost immediately. At 18 kV only a few short pulses are evident followed by an intense current build up (Figure 5.1.3e). A conductive plasma channel then carries the charge to the bubble wall.

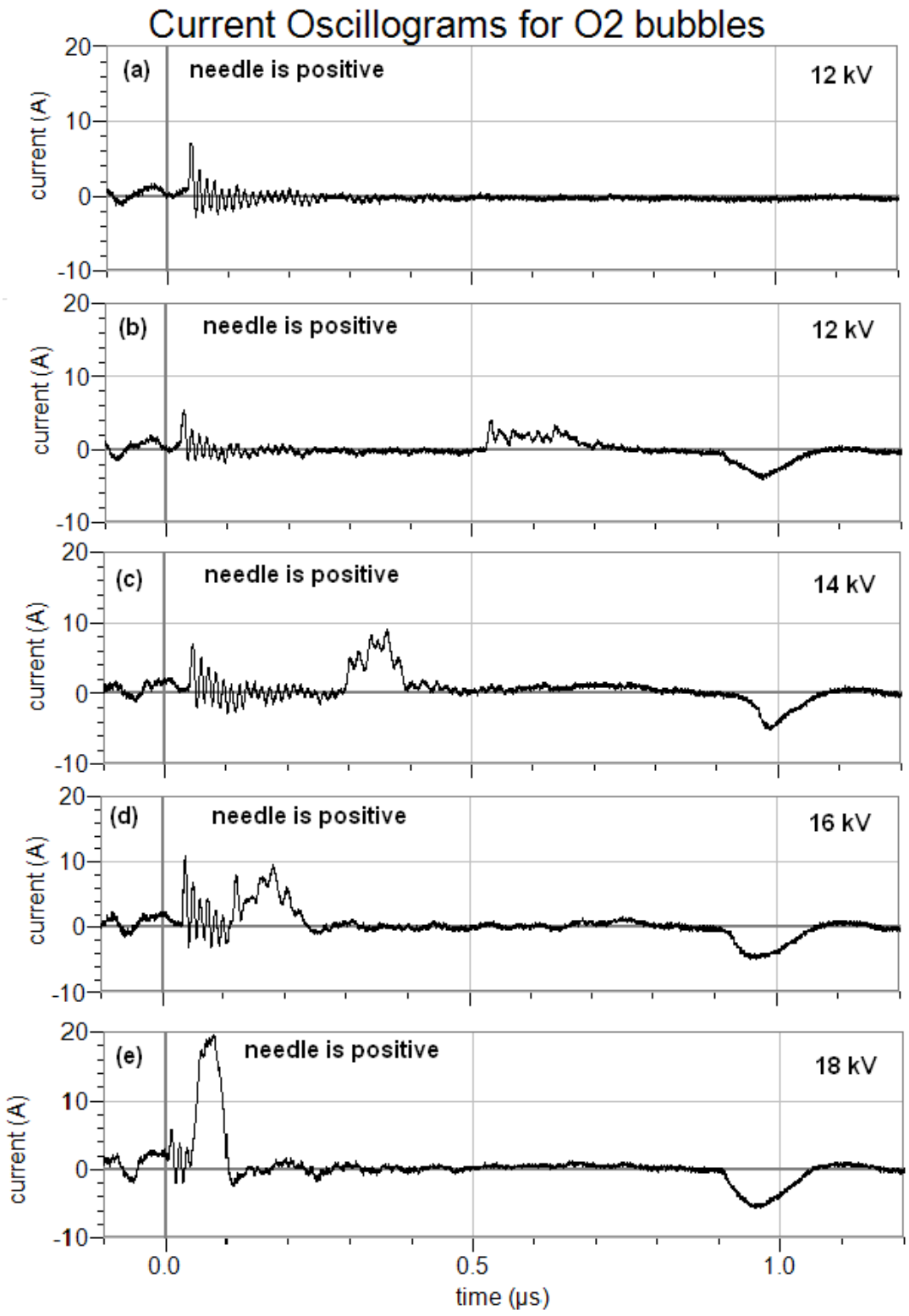

Figure 5.1.3 Current oscillograms for the discharge in oxygen bubbles at various voltages.

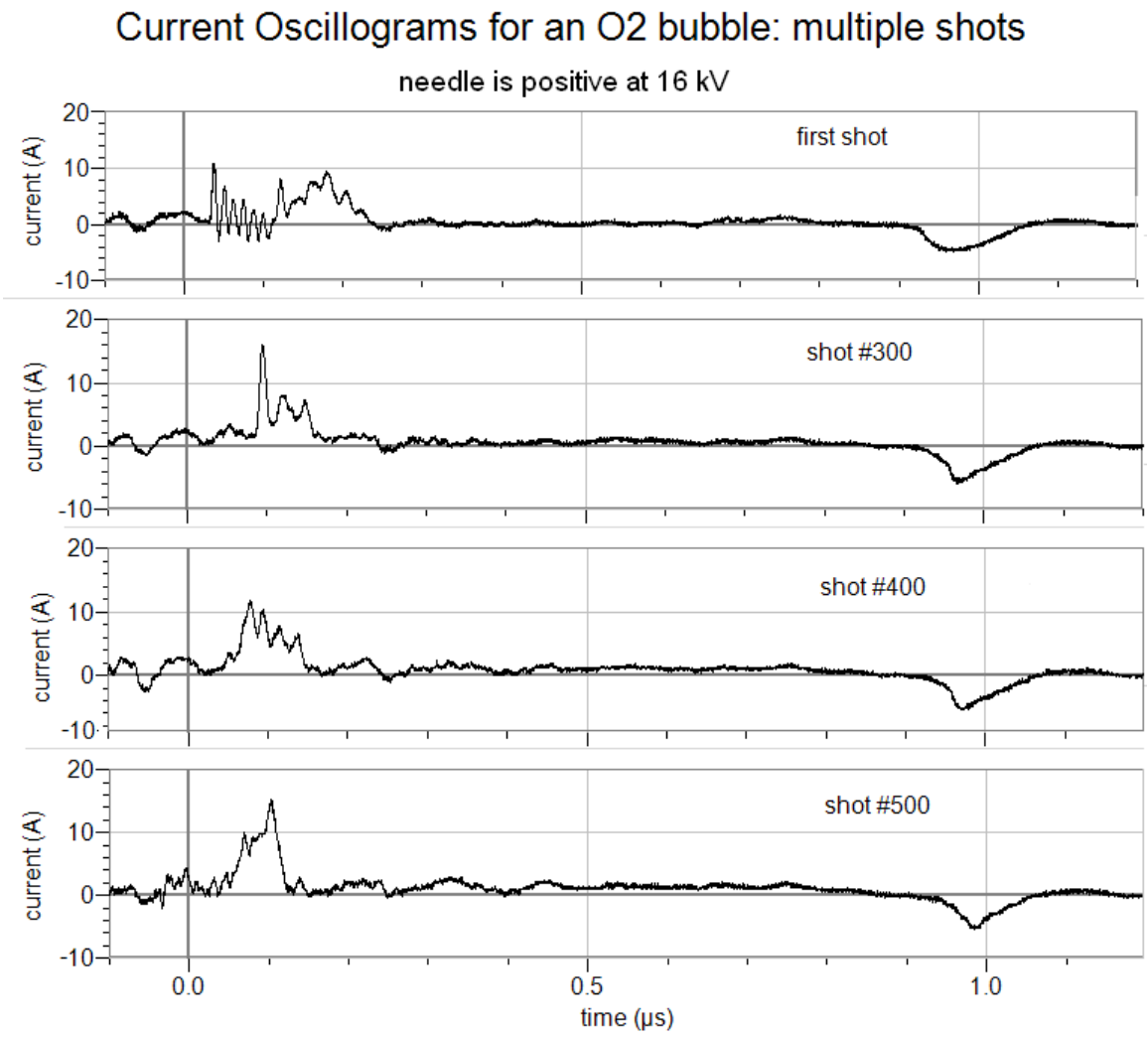

Figure 5.1.4. Current oscillograms for the discharge in oxygen bubbles for various numbers of repeated shots.

The next experiment involved repeated voltage pulses applied to the same bubble. The results are shown in Figure 5.1.4. These oscillograms are taken for pulses applied at a rate of 1 Hz. The graphs show that the individual short pulses disappear almost entirely by at least shot #300. For the later shots, the discharge current starts without delay. This is similar to the effect observed in Ar bubbles.

Through all these experiments the pulse corresponding to the discharge current lasts longer in air and oxygen than it does in Ar. The current pulse in Ar increases in

duration with the repeated application of voltage pulses. This is attributed to the increase in the concentration of electronegative species. The longer current pulse duration for air and oxygen support this hypothesis, as the two are progressively more electronegative.

The negative polarity of the needle leads to a higher starting voltage in oxygen. The sharp pulses are not present prior to the longer discharge current, but the overall current is lower. The current does not start until the voltage is high enough to build up the charge sufficiently to create the conducting channel. This is consistent with the slower negative streamer formation. Higher fields and longer times are needed for the negative polarity of the sharp electrode. Further discussion of the mechanism takes place in a later section of this work.

Air represents an intermediate species here as it is primarily N_2, but has more O_2, etc. than an Ar bubble. The oscillograms for air are not affected significantly by the repeated application of voltage pulses. The Table 5.1.2 shows some of the analysis results for air bubbles.

The current values and the charge estimates give the electron density in the same range ($\sim 10^{14}$) for all three situations, argon, air, and oxygen.

Detailed analysis of the electrical characteristics of the discharge reveals information on the parameters of the discharge and gives a glimpse of the possible mechanisms of the discharge formation and propagation. To put together a detailed description of the discharge processes the electrical information must be combined with the imaging and spectroscopic analysis.

Table 5.1.2 Data analysis for air bubbles

Analysis of current oscillograms for Air bubbles										
Needle polarity	Applied Voltage, kV	First wide current max, A	Duration of first peak, ns	Charge, nC	electron number, Ne	Reverse current peak, A	Reverse current duration, ns	Reverse peak charge, nC	Total net current, A	**electron density, cm-3**
negative	12	4.00	100	356	2.2E+12	2.80	200	260	0.16	4.E+14
negative	16	9.50	140	538	3.4E+12	8.90	200	580	0.14	7.E+14
negative	16	9.60	102	271	1.7E+12	1.60	150	124	0.23	3.E+14
negative	18	17.80	100	423	2.6E+12	7.40	200	740	0.67	5.E+14
positive	16	15.90	100	523.7	3.3E+12	4.1	150	214.7	1.33	7.E+14

In conclusion,

- The discharge in oxygen and air start at a higher voltage than the discharge in Ar bubbles.
- The discharge in oxygen and air bubbles start at a higher voltage for the negative than for the positive polarity of the needle.
- In oxygen, individual electron avalanches are visible prior to the initiation of the discharge current.
- Reverse current corresponding to the current build up on the bubble wall is not present without the presence of the discharge current. Individual electron avalanches do not produce the conductive channel needed to carry the discharge current.
- Increasing the applied voltage reduces the transition time from the individual avalanches to a discharge channel.

References:

1. S. Ihara, M. Miichi, S. Satoh, and C. Yamabe, IEEE Intl Pulsed Power Conf.5451, (1999) 1291.
2. P. Lukes, A.T. Appleton, B. Locke, IEEE Trans. Ind. Appl., **40** (2004) 60-67
3. P. Lukes, B. Locke, Ind. Eng. Chem. Res., **44** (2005) 2921-2930
4. C. Yamabe, F. Takeshita, T. Miichi, N. Hayashi, S. Ihara, Plasma, Process. Polym**, 2** (2005) 246-251
5. R. Zhang, L.M. Wang, C. Zhang, Y. Nie, Y. Wu, Z. Guan, IEEE TRANSACTIONS ON PLASMA SCIENCE, VOL. 34, NO. 3, JUNE 2006
6. V. I. Grinevich, Theoretical Foundations of Chemical Engineering, Vol. 38, No. 1, 2004, pp. 56–60.
7. S. Gershman, O. Mozgina, A. Belkind, K. Becker, and E. Kunhardt, Contrib. Plasma Phys. **46**, No. 1-2, 1 . 7 (2007)
8. Yu. Raizer, Gas Discharge Physics, Springer-Verlag, New York, (1997)
9. K. H. Becker, U. Kogelschatz, K. H. Schoenbach, R. J. Barker, Non-Equilibrium Air
10. A.Fridman, L. Kennedy, Plasma Physics and Engineering, Taylor & Francis, (2004)

5.2. Discharge Investigation Using Emission Spectroscopy

The optical emission from a discharge in an oxygen bubble is investigated in the 300 – 340 nm, 600 – 700 nm, and 750 – 850 nm regions. The spectra are recorded for both the positive and negative polarity of the needle electrode. The spectra are shown in Figure 5.2.1. An attempt was made to introduce a small percentage of Ar into the bubble in addition to oxygen in order to evaluate the electron temperature. Ar emission was not detected up to 10% concentration. These experiments were abandoned since introducing more than trace amounts of Ar affects the discharge processes. It is concluded that using trace inert gas spectroscopy is not possible with the current set of equipment. OH band emission as well as nitrogen molecular band emission are present in some of the situations and are used to determine the rotational and vibrational temperatures of the discharge in oxygen bubbles, using the same methodology as for the study of Ar. The overview of the spectra and the results for the rotational and vibrational temperatures are presented below.

5.2.1. **An Overview of the Emission Spectrum**

The prominent features of the spectra of the discharge in oxygen bubbles include the emission lines of atomic hydrogen and oxygen, and the molecular bands of theOH radical, N_2, some O_2 and other molecules. The presence of reactive species (H, O, OH, etc.) is important for the practical applications of this discharge. The variability of the amount of collected light and the bubble itself make it difficult to compare line or band intensities from one experiment to another. To overcome the low intensity of light

collected in each CCD channel, the light is accumulated from fifty or a hundred shots. This strategy also averages the emission over fifty or one hundred individual discharges, allowing general tendencies to remain in spite of individual variations.

The spectra from the oxygen discharge generally show lower intensities for atomic hydrogen lines than the spectra for discharge in Ar bubbles, indicating lower concentration of atomic hydrogen. This is due to the reactions between the atomic hydrogen and oxygen that are more frequent in oxygen gas. Two atomic oxygen lines are very strong, the 777 nm and the 844 nm lines corresponding to $O(3p^5P \rightarrow 3s^5S)$ and $O(3p^3P \rightarrow 3s^3S)$ transitions. Two different mechanisms are responsible for these line emissions.[1,2] Dissociative excitation

$$O_2 + e \rightarrow O^* + O + e$$

is mostly responsible for the emission of the 777 nm line and direct impact excitation of atomic oxygen

$$O + e \rightarrow O^* + e$$

is the primary pathway resulting in the 844 nm line emission. The study of the relative intensities of these two lines can provide insight into the O/O_2 ratio in the gas, provided the same de-excitation mechanisms. Such a study may be desirable in the future. A brief look at the spectra presented here shows a higher intensity of the 777 nm line with respect to the 844 nm when the needle is positive and visa versa when the needle is negative. This seems to indicate a higher concentration of atomic oxygen for a discharge with a sharp electrode at a negative potential. This relationship needs to be confirmed in future studies.

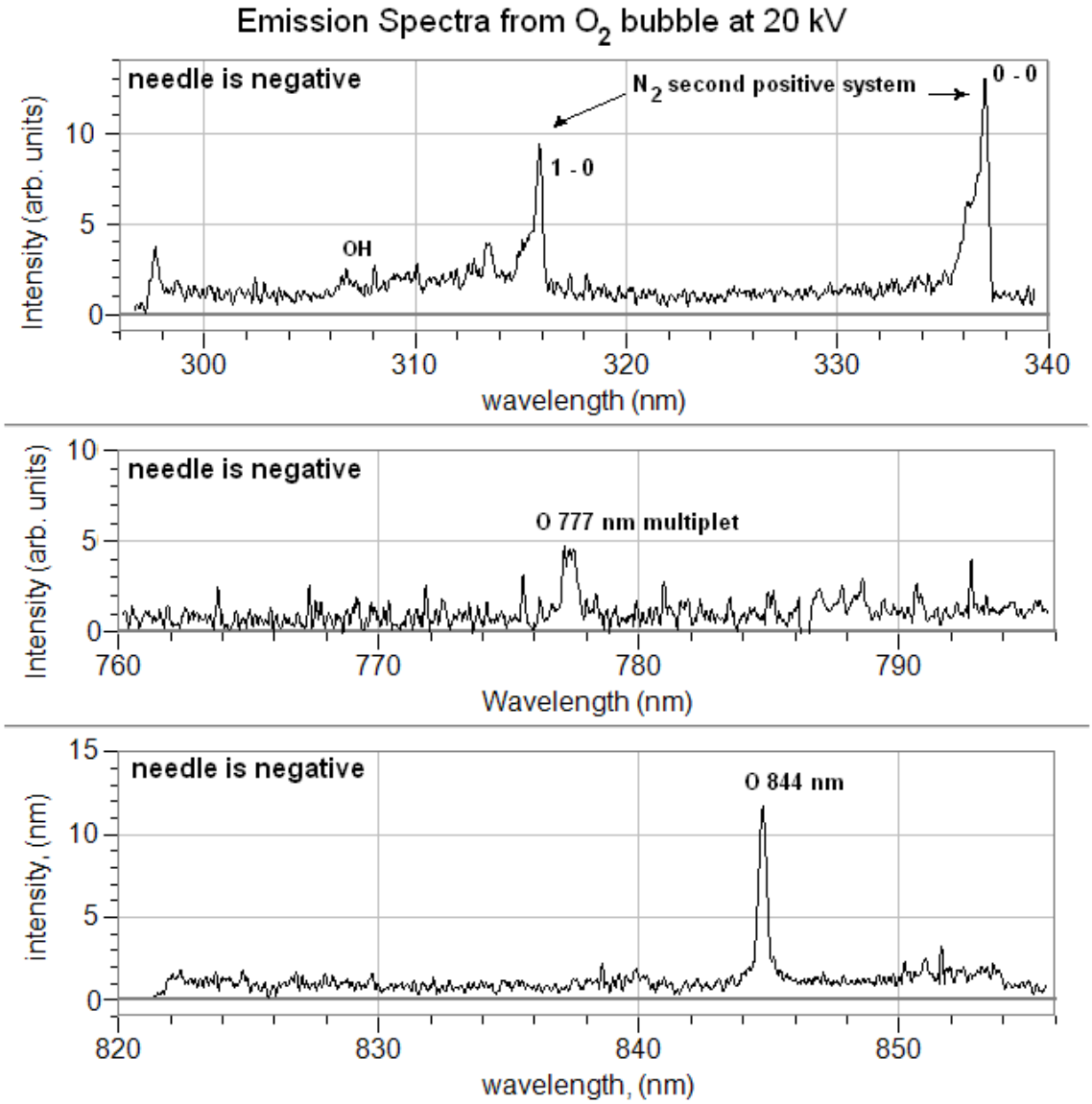

Figure 5.2.1 Graphs show the spectra of optical emission by the discharge in O_2 bubbles at 20 kV in three spectral regions. The needle is kept at a negative potential. The camera is gated to 1200 ns and collects 100 accumulations (100 shots).

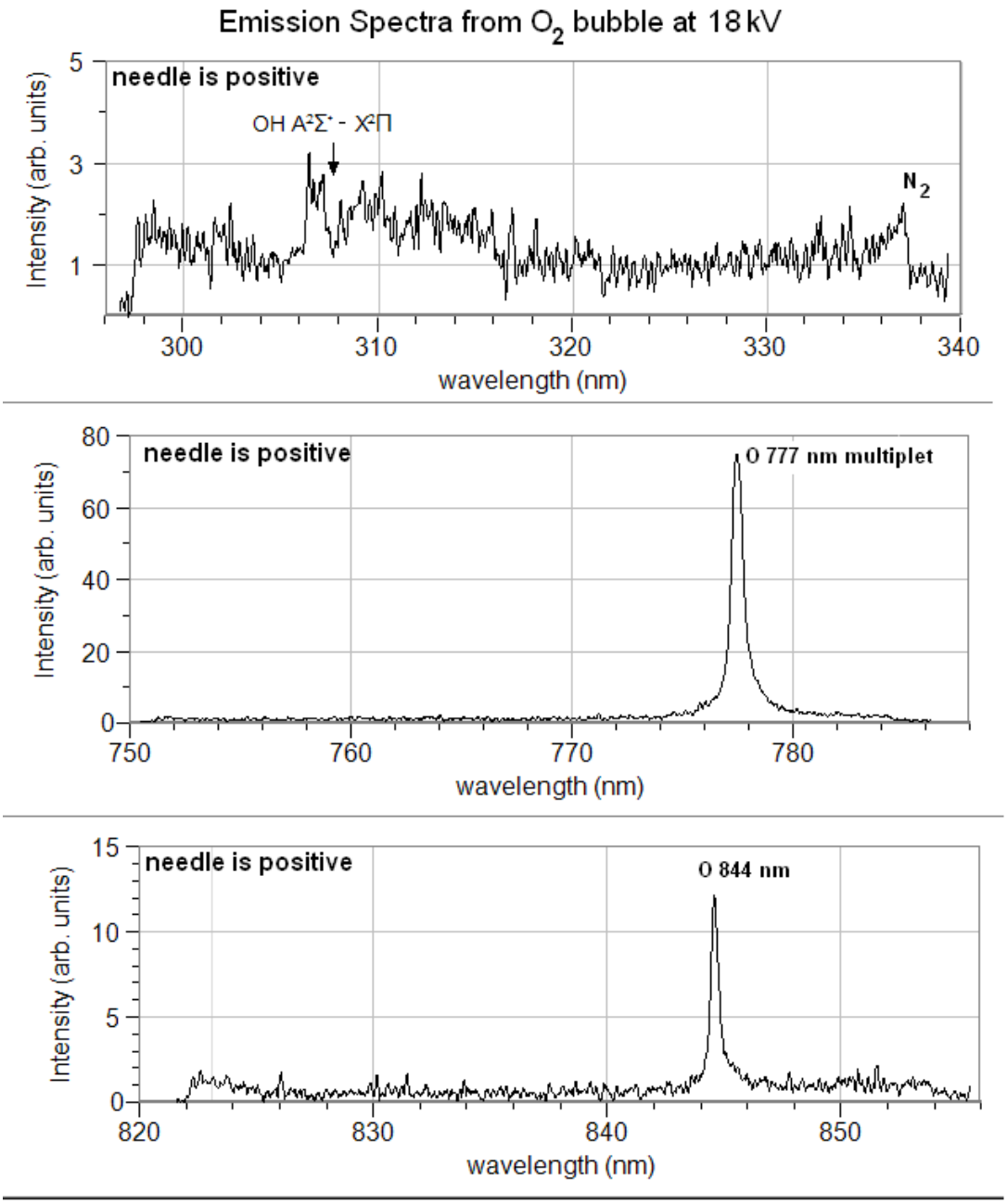

Figure 5.2.2 Graphs show the spectra of optical emission by the discharge in O_2 bubbles at 18 kV in three spectral regions. The needle is kept at a positive potential. The camera is gated to 1200 ns and collects 100 accumulations (100 shots).

Molecular nitrogen is always present in the gas bubbles here because both the stored DI water and the experimental system are open to the atmosphere. The N_2 emission bands have been seen in Ar spectra and appear again in the oxygen spectra as well. These bands

are below the detection level for the discharge in oxygen bubbles if the needle is kept at a positive potential. (Please compare the 290 – 340 nm range for the spectra in Figures 5.2.1 and 5.2.2.) The variations in concentration of N_2 or other initial gas species in the bubbles have been ruled out by changing the polarity of the needle while keeping the same bubble. This is a persistent effect independent of changing other experimental conditions. Excitation threshold for the $C^3\Pi_u$ state of the second positive system investigated here is 11.05 eV.[3, 4] The excitation into this state appears to be less probable under the investigated conditions for a positive polarity of the needle electrode.

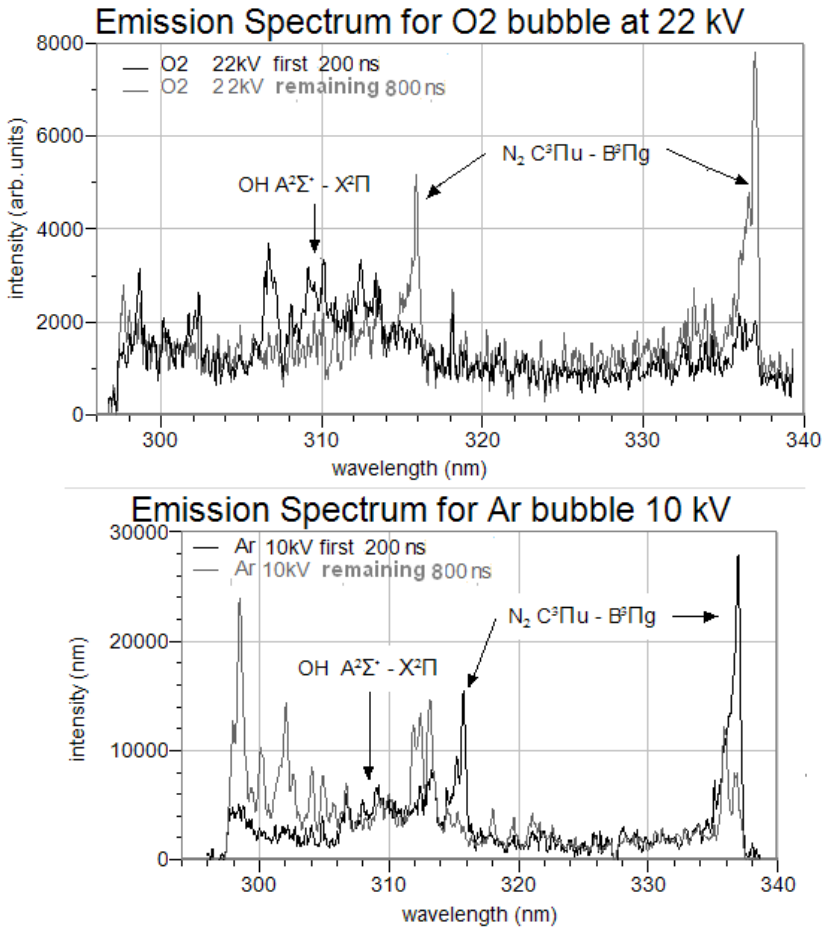

Figure 5.2.3. The figure shows emission spectra for oxygen (above) and argon (below) bubbles. Each graph presents two spectra for comparison, one taken during the first 200 ns of the discharge and the second taken during the following 800 ns of the voltage pulse.

The same effect is observed when spectra are taken at different times during the applied voltage pulse. The upper graph in Figure 5.2.3 shows two spectra for an O_2 bubble with the needle at a negative potential. The spectrum shown in grey is taken with the camera gated to the first 200 ns of the discharge and is clearly dominated by the second positive band system of N_2. The black line shows the spectrum taken with the camera gated for 800 ns with a 200 ns delay from the start of the discharge. Gating for this time period avoids the formation and initial stages of the discharge. The nitrogen band system is indistinguishable in the spectrum corresponding to the later time. The same effect is observed for the Ar spectra. The spectra taken during the first 200 ns display strong N_2 bands; these bands are missing from the spectra taken during the later time in the discharge process.

In summary, the following general features have been observed in the spectra from the discharge in oxygen bubbles in water:

- The following active species are present: H, OH, O.
- Concentrations of H seem lower than in the discharge in Ar bubbles.
- The intensity ratio of the 777 nm to the 844 nm line appears to change with the changing polarity of the needle electrode.
- The N_2 molecular band emission is prominent when the needle is at the negative potential and diminishes when the needle is positive.
- The N_2 molecular band emission is prominent during the first 200 ns of the discharge (negative needle) and diminishes at a later time during the discharge.

5.2.2. **Vibrational Temperature Using N_2 0-0 Emission Band**

The methodology for determining the vibrational excitation temperature has been described in detail in Section 4.4.2.2. The same method is used to determine the vibrational excitation temperature for the discharge in oxygen bubbles with negative potential on the needle electrode. The 315.9 nm system is used although sometimes only two of the heads 315.93 nm and 313.6 nm can be distinguished clearly. In those cases the ratio of the two lines has been used to find the Boltzmann factor. Regression lines were fitted when three or more heads were identified and used. Attempts to identify all the low intensity interfering bands have not been successful. The spectra with sufficiently high intensity bands in the 300 – 340 nm region correspond to the discharges at 20 and 22 kV. The vibrational excitation temperatures resulting from the analysis of the 315.9 nm N_2 band system are given in Tables 5.2.1. and 5.2.2. The first set of calculations is performed using the data from the first 200 ns of the discharge. The average resulting temperature is in the range of 0.8 – 1.0 eV with a margin of error of about 0.2 eV.

Table 5.2.1 Vibrational temperatures calculated using the N_2 second positive system 0-0 bands emission taken during the first 200 ns of the discharge. The error estimate is +/- 2000 K (~0.2 eV).

needle is negative

Vibrational Temperatures, first 200 ns			
Applied Voltage, kV	time	Tvib, eV	Tvib, K
20	first 200 ns	1	11000
22	first 200 ns	0.86	10000

The second set of calculations uses the spectra averaged over the duration of the entire voltage pulse (1200 ns exposure). Since there is no significant contribution to the spectrum from the N2 emission bands during the intermediate time of 800 ns (after a 200 ns delay), most of the recorded emission is due to the light emitted during the first 200 ns and also during the last reverse discharge event. As expected, results are close to those for the first 200 ns. The temperature is in the range of 7000 – 9000 K for the applied voltage of 20 kV and 9000 – 12000 K for the applied voltage of 22 kV. These results seem to show a marked increase in temperature (without an overlap in the data) with the increase in applied voltage. Since the data are only for two values of applied voltage, more measurements are needed to confirm this tendency. The lower error (+/-0.11 eV) for these measurements is due to greater measured intensity and higher signal-to-background ratio.

Table 5.2.2 Vibrational temperatures calculated using the N_2 second positive system 0-0 bands emission for different applied voltages. The needle polarity is negative and the camera exposure time is 1200 ns.

Vibrational temperature using N2 emission bands		
Applied Voltage, kV	Tvib, eV	Tvib, K
20	0.72	8000
20	0.66	7700
20	0.79	9000
Ave	**0.72**	**8400**
error	**0.06**	**700**
22	0.85	9900
22	0.83	9700
22	1.03	12000
Ave	**0.90**	**10000**
error	**0.11**	**1000**

needle is negative

In conclusion, the vibrational excitation temperature for the discharge in O_2 bubbles in water has been determined using the N_2 second positive emission band system. The temperature is in the range of 0.7 – 1.0 eV (+/- 0.11eV) and is higher for 22 kV than for 20 kV applied voltage. The needle is always at a negative potential in all these experiments.

5.2.3. Rotational temperature

5.2.3.1. Rotational Temperature Using OH emission

The OH 306.4 nm $A^2\Sigma^+ - X^2\Pi$ system is present in all spectra from the discharge in O_2 bubbles. The use of this system to determine the rotational temperature of the discharge has been discussed in detail in Section 4.4.2.3. Following the same procedure, three regions are distinguished in the spectrum, 306.3 nm – 307.3 nm, 307.6 nm – 308.8 nm, and the region ahead of 308.9 nm. The global maxima of the first two regions are found and the ratio of the maximum intensity of the second region to that of the first R_2/R_1 is used to estimate rotational temperature.[5] Rotational temperature has been calculated for both the positive and negative polarity of the voltage applied to the needle electrode. For the negative needle, the spectra have been analyzed for applied voltages of 18, 20, and 22 kV, for different time periods during the discharge, and for repeated trials under the same conditions. For positive potential on the needle the spectra have been analyzed for 20 and 22 kV of applied voltage. The discharge under these conditions is too dim for time-resolved measurements. Table 5.2.3 lists the results for negative needle and various applied voltages. The values for R_2/R_1 are listed together with the temperature

estimates from the graph from Pellerin.[5] The error listed in the table is for the R_2/R_1 ratio estimate. Reading the temperature values from the graph combined with the R_2/R_1 error, results in an estimated error of +/-200 K. There does not appear to be any significant change with voltage increase from 18 to 20 kV, but there is a sudden increase for the 22 kV applied voltage.

Table 5.2.3 Rotational temperature results for the discharge in an O_2 bubble for different applied voltages. The needle polarity is negative, and the camera is gated for the entire 1200 ns of the applied voltage pulse.

Rotational temperature using OH emission; exposure time 1200 ns					
Applied Voltage, kV	**R1**	**R2**	**R2/R1**	**Trot, K**	**Trot, eV**
18	1350	1200	0.89		
18	1600	1540	0.96		
18	1400	1100	0.79		
Ave			**0.88**	**1500**	**0.14**
Std. dev.			**0.09**		
20	2000	1900	0.95		
20	4000	4200	1.05		
20	2700	2550	0.94		
Ave			**0.98**	**1300**	**0.12**
Std. dev.			**0.06**		
22	5570	3646	0.65		
22	6700	4100	0.61		
22	6980	4600	0.66		
Ave			**0.64**	**2000**	**0.18**
Std. dev.			**0.03**		

needle is negative

Only the discharges at 20 and 22 kV of applied voltage are bright enough for the 200 ns exposure time. The spectra at these two applied voltages have been analyzed for the first 200 ns and for the remaining 800 ns of the discharge and the results are given in Table 5.2.4. The data are consistent with the results listed above within the experimental

error. Although the differences in the temperature values in Table 5.2.4 are not significant, there does appear to be a tendency of rotational temperature to increase at the later times in the discharge process and also with the applied voltages. Once again, further investigation is needed to confirm these tendencies. These temperatures also appear to be in the same range as those determined for the discharge in Ar bubbles (1500 – 2000 K).

Table 5.2.4 Rotational temperature given in this table is determined using the OH 306.4 nm $A^2\Sigma^+$ - $X^2\Pi$ system. The spectra is recorded with the camera gated for the fist 200 ns of the discharge and for the remaining 800 ns. The number of accumulations is 100.

needle is negative

Rotational Temperatures at different times			
Applied Voltage, kV	time	Trot, eV	Trot, K
20	first 200 ns	0.11	1300
20	remaining 800 ns	0.13	1500
22	first 200 ns	0.12	1400
22	remaining 800 ns	0.15	1700

For a positive potential on the needle electrode the rotational temperature is determined for the applied voltages of 16 and 18 kV. Lower voltages do not produce a bright enough discharge and higher voltages are not technically possible in the current set-up. The temperatures are determined to be 1600 and 1700 K (+/- 200 K as before) for the 16 and 18 kV respectively. Results are listed in Table 5.2.5.

To summarize, rotational temperatures determined by the analysis of the OH vibrational band are in the range of 1300 – 2000 K and appear to increase at the later

times in the discharge. The dependence on voltage is weak and should be investigated further.

Table 5.2.5 Rotational temperature from the OH band spectrum for the positive voltages of 16 and 18 kV applied to the needle.

Rotational temperature using OH emission; exposure time 1200 ns; needle is positive					
Applied Voltage, kV	**R1**	**R2**	**R2/R1**	**Trot, K**	**Trot, eV**
16	3670	3200	0.87		
16	3800	3500	0.92		
16	3400	2553	0.75		
Ave			**0.85**	**1600**	**0.15**
Std. dev.			**0.09**		
18	2962	2465	0.83		
18	2939	2424	0.82		
18	4066	2717	0.67		
Ave			**0.78**	**1700**	**0.15**
Std. dev.			**0.09**		

5.2.3.1. Rotational Temperature Using N_2 emission bands

The method of fitting an N_2 emission band with a simulated spectrum calculated with temperature as the optimization parameter has been described in Section 4.4.2.3.1. The same method is now used to determine the rotational temperature of the discharge in O_2 bubbles. The 0 – 0 band from the N_2 second positive system (C^3P_u – B^3P_g) with the peak at 337.13 nm is chosen again. (See the spectra in Figures 5.2.1 and 5.2.3). The modeling program used here has been provided by Dr. Kevin Martus, William Paterson University, Wayne, NJ. A sample fit showing the theoretical and the experimental spectrum is found in Figure 5.2.4. This method is applied to conditions with the negative voltage on the needle, since nitrogen molecular bands are not distinguishable in the

spectra at positive polarity. The results for the applied voltages of 18, 20, and 22 kV are shown in Table 5.2.6. The error estimate for these measurements is in the range of 50 – 80 K or about 8%.

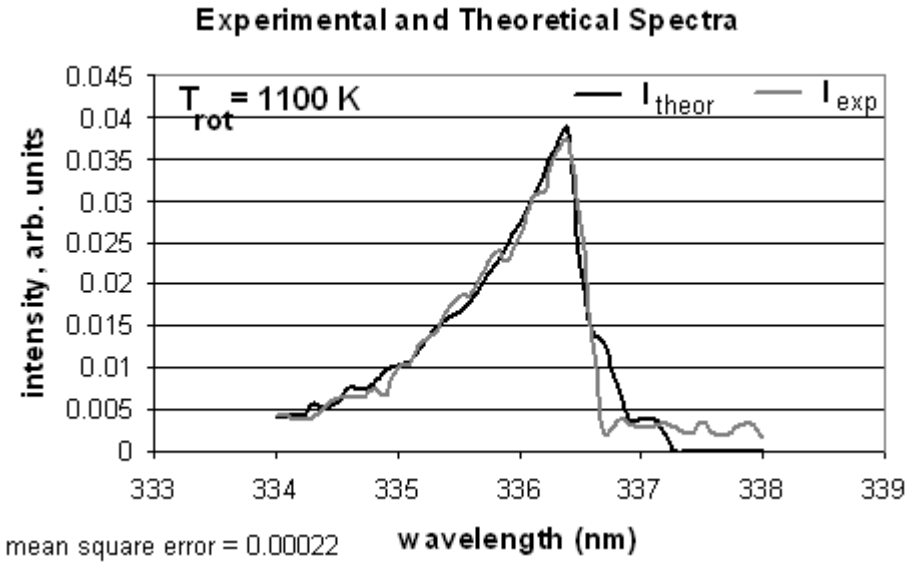

Figure 5.2.4 Experimental and simulated spectra showing the fit used to determine the rotational temperature for a discharge in an O_2 bubble. The spectra are normalized to the maximum.

The temperature determined using the N_2 simulated spectrum is still lower than the temperature determined using the OH emission band, but the agreement between the two methods is much better. The temperature values show a considerable overlap with the values determined using the OH band emission with the exception of the 2000 K value obtained with the OH spectrum analysis. The two methods seem to agree better than they do for Ar.

In conclusion, the rotational temperature determined by simulating the emission spectrum of the 0-0 band of the second positive system of N_2 falls in the range of 950 –

1500 K. The temperature seems to demonstrate a slight tendency to increase with voltage, but this tendency must be investigated further.

Table 5.2.6 The rotational temperature of a discharge in oxygen bubbles determined using the 0-0 band emission spectrum of the nitrogen molecule. The error estimates shown in the table include the accuracy of the fit.

(a)

Rotational Temperature using N2 0-0 band		
Applied Voltage, kV	Trot, K	Trot, eV
18	1300	0.11
18	1400	0.12
Ave	**1350**	**0.12**
error	**100**	**0.01**
20	1000	0.09
20	950	0.08
20	1000	0.09
Ave	**980**	**0.08**
error	**80**	**0.01**
22	1500	0.13
22	1000	0.09
22	1500	0.13
Ave	**1300**	**0.11**
error	**100**	**0.01**

(b)

Rotational Temperature, first 200 ns using N2 0-0 band			
Applied Voltage, kV	time	Trot, eV	Trot, K
20	first 200 ns	0.08	900
22	first 200 ns	0.09	1000

needle is negative

Bibliography:

1. R. E. Walkup, K. L. Saenger, G. S. Selwyn, J. Chem. Phys., **84** (1986) 2668-74
2. N. Krstulovic, I. Labazan, S. Milosevic, U. Cvelbar, A. Vesel, and M. Mozetic, J. Phys.D: Appl. Phys. **39** (2006) 3799-3804
3. G. Herzberg, Molecular Spectra and Molecular Structure, Vol. 1 (Spectra of Diatomic Molecules), Van Nostrand-Reinhold, New York, (1950).
4. K. H. Becker, U. Kogelschatz, K.H. Schoenbach, R. J. Barker, Non-Equilibrium Air Plasmas at Atmospheric Pressure, IoP Publishing, Bristol (2005)
5. S. Pellerin, J. M. Cormier, F. Richard, K. Musiol, J. Chapelle, J. Phys. D. Appl. Phys.29, (1996),726-739

5.3 Imaging of the Discharge in Oxygen and Air bubbles

A detailed investigation of the discharge in air bubbles is conducted using the same techniques as for Ar bubbles. The images do not contribute much new information except for one very significant detail. Figure 5.3.1 shows the first few images of a discharge in the Ar bubble in the top row and that for an air bubble in the bottom row. The discharge in the air bubbles seems to propagate slower than the discharge in Ar bubble. Detailed measurements of the distances traveled would require extensive statistical analysis due to the random changes from one discharge (one frame) to another. In addition, a higher power objective lens would be helpful to provide better image resolution than at present.

The images of the discharge in oxygen bubbles clearly show that the discharge has a tendency to reach the bubble wall via a shorter path and propagate further along the bubble wall (Figure 5.3.2). Some branching is also visible, although care should be taken not to confuse the actual image and its reflection off the water surface.

Summarizing, the images of the discharge in oxygen bubbles show that the discharge tends to propagate to the bubble wall along the shortest possible path and propagate along the wall that is along the water surface. The images confirm the slower rate of development of the discharges in air and oxygen with a negative needle electrode than the discharge under the same conditions in Ar.

Figure 5.3.1 The figure shows a sequence of images of the discharge in an air bubble and in Ar bubble taken with 5 ns exposure and a 5 ns time step.

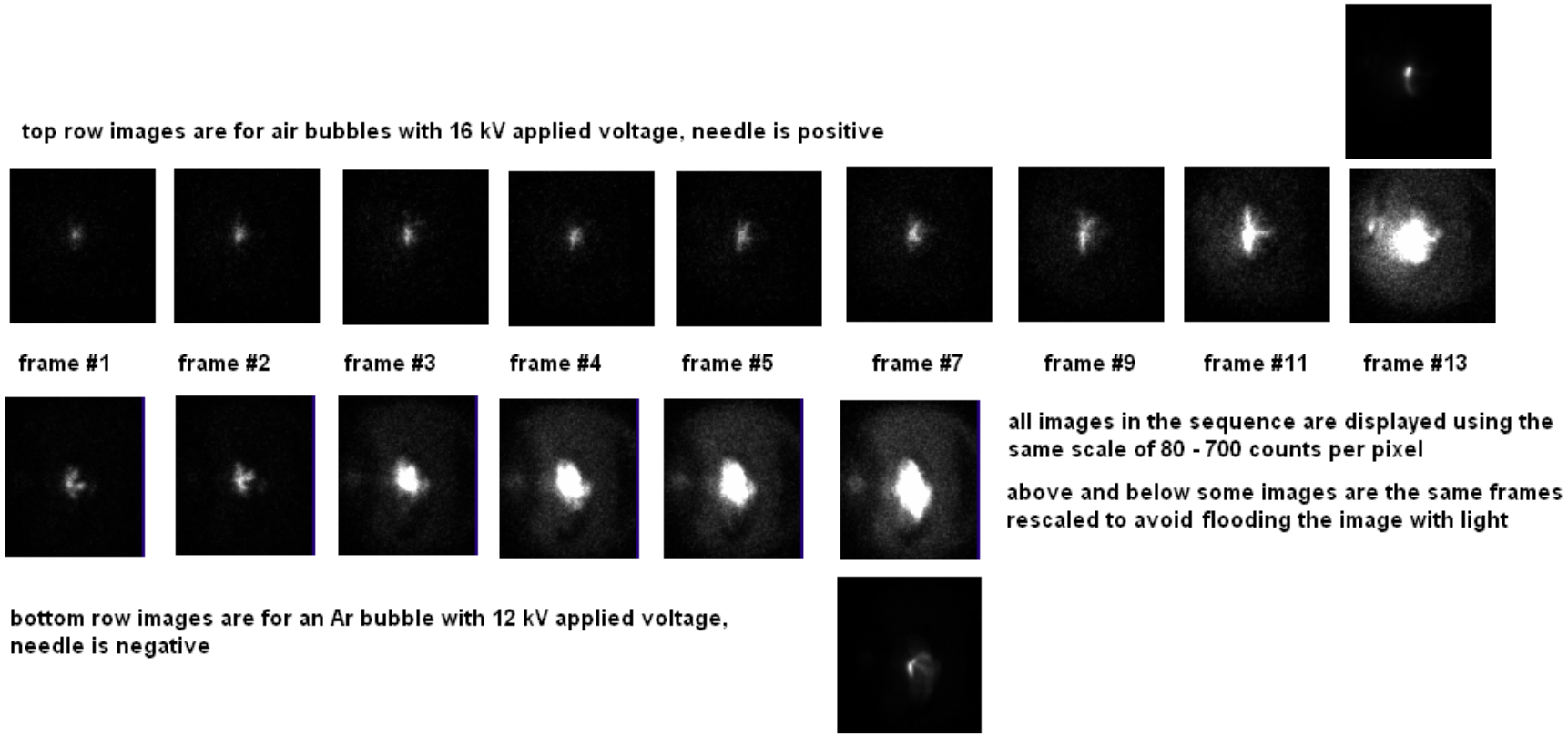

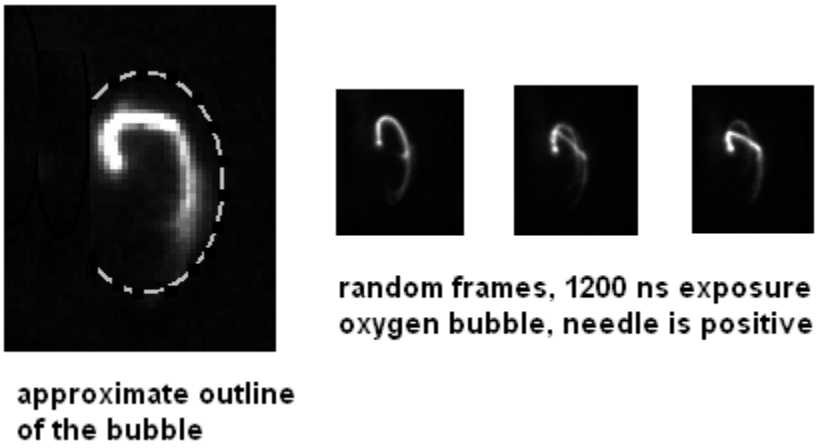

Figure 5.3.2 Time averaged images of the discharges in an oxygen bubble.

5.4. Discharge in O_2 Bubbles: Discussion

The discharges in oxygen and air bubbles have been investigated briefly. The geometry of the bubble-water-electrodes configuration is the same as for Ar bubbles. The needle electrode serves as the cathode in some of the experiments and as the anode in others. Some of the properties of the discharge in oxygen and air bubbles have been summarized in Table 5.4.1 along side the characteristics of the discharge in Ar bubbles for comparison.

Table 5.4.1 Discharge regimes and characteristics for the discharges in Ar, oxygen, and air bubbles. The discharges in air and oxygen bubbles are produced with a positive and negative needle electrode. The data listed here have been obtained for ~8 mm diameter bubbles with applied voltage in the range of 8 – 20 kV (up to 22 kV for negative polarity and oxygen bubbles)

Discharge conditions and parameters:	Discharge in Ar bubble	Discharge in O_2 bubble	Discharge in air bubble
Gas	Ar	O_2	air
Pressure	1 atm	1 atm	1 atm
Distance	~ 5 mm	~ 5 mm	~ 5 mm
pd	300 – 400 Torr*cm	300 – 400 Torr*cm	300 – 400 Torr*cm
Filament radius	~0.1 – 0.5 mm	~0.1 – 0.5 mm	~0.1 – 0.5 mm
Peak current	25 – 60 A	5 – 20 A	5 – 15 A
Peak current density	~ 500 – 1000 A/cm^2	~ 100 – 400 A/cm^2	~ 100 – 300 A/cm^2
Charge transferred	0.5 – 1.0 μC/first pulse	0.3 – 0.8 μC/first wide pulse	0.2 – 0.5 μC/first pulse
Current pulse duration	~50 ns (first pulse)	~100 – 150 ns	~100 ns
Electron density	~10^{14} – 10^{15} cm^{-3}	~10^{14} cm^{-3}	~10^{14} – 10^{15} cm^{-3}
Electron temperature	~ 7000 – 9000 K 0.6 – 0.8 eV		
Vibrational temperature	~ 8000 – 9000 K ~ 0.7 – 0.8 eV	~8000 – 11000 K ~0.7 – 1 eV	
Rotational temperature	1000 – 1300 K ~ 0.1 eV	~1100 - 1700 K ~0.1 – 0.15 eV	
Additional notes		~10 ns long, ~50nC, 8 – 10 A peaks precede the main current peak	

The peak current is lower for oxygen and air than for Ar and the duration of the current peaks is longer. The lower current values but longer durations result in similar total transferred charge and comparable electron density estimates for all three gas compositions. Vibrational and rotational excitation temperatures are slightly higher for oxygen than Ar. The images show the discharge starting at the needle and propagating toward the bubble wall. The discharge in oxygen bubbles tends to find the shortest way to the bubble wall and proceed along the wall.

Most of the observed differences in the discharge evolution and parameters between the three gas compositions may be attributed to the presence of electronegative gases. All three situations have water vapor as one of the gasses in the bubble which accounts for the presence of H, OH, and some oxygen, but the amounts of oxygen vary greatly from argon to air to oxygen gas. The electron affinities of some of the electronegative species are listed in Table 5.4.2. In the discharge, the electron generating processes, such as electron impact ionization and electron detachment processes compete with electron attachment. This slows the initial formation stages of the discharge and results in plasma that contains a sizeable concentration of negative ions. The estimated electron density is still consistent with a streamer discharge, but the condition for the transition to streamer (4.5.1) has to be modified to include the attachment processes represented by the attachment coefficient η:

$$N_e = \int_{x_1}^{x_2} [\alpha(E) - \eta(E)]\, dx \approx 3 \cdot 10^8 cm^{-3} \qquad (5.4.1)$$

Several avalanches are initiated and extinguished before the build up in electron density becomes high enough for the transition of the streamer. This is observed in the current traces

Table 5.4.2. Electron affinity for various common atomic and molecular species [1].

Atom, molecule, or radical	Electron affinity, eV
OH	1.8
O	1.5
O_2	0.44
O_3	2.0
NO_2	3.1
HO_2	3.0

Table 5.4.3 Examples of some relevant ionization and attachment processes that occur in discharges in Ar, oxygen, air.

Ionization	Attachment
$e + Ar \rightarrow Ar^+ + e + e$	$e + O_2 \rightarrow (O_2^-)^* \rightarrow O_2^-$
$e + N_2 \rightarrow N_2^+ + e + e$	$e + OH \rightarrow OH^-$
$e + O_2 \rightarrow O_2^+ + e + e$	$e + O \rightarrow O^-$
$e + H_2O \rightarrow H_2O^+ + e + e$	$e + O_2 \rightarrow (O_2^-)^* \rightarrow O^- + O$
$e + H_2 \rightarrow H_2^+ + e + e$	
$e + O \rightarrow O^+ + e + e$	
$e + OH \rightarrow OH^+ + e$	

as preliminary sharp peaks. These are the result of avalanches that develop and extinguish without reaching the surface of the water. After a series of these preliminary avalanches, the space charge build up becomes sufficient to form a longer current pulse carrying substantially (~x10) more charge and reaches the bubble surface. Imaging of air bubbles confirms the correlation between the development of the current and the spatial progression of the discharge.

Imaging of oxygen bubbles showed the tendency of the discharge in those bubbles to propagate along the wall of the bubble. Unlike the streamer in Ar that simply spreads somewhat upon reaching the water, the discharge in oxygen travels along the bubble wall for some time and then stops propagating. The propagation terminates prior to the decrease in the applied voltage. Charge deposition on the water surface occurs in air and oxygen as it does in Ar, as evidenced by the reverse discharge at the end of the pulse.

Spectroscopic measurements of the rotational and vibrational excitation temperature of the discharge in oxygen bubbles give slightly higher values to these two parameters than in Ar bubbles. This indicates a higher transfer of energy to the gas. The need to overcome electron attachment leads to higher starting voltages and hence higher operating voltages. This means higher energy input into the discharge. This energy does not go entirely to increasing the electron energy but instead gets transferred to other species through collisions. In oxygen and air there is a much higher rate of collisions with molecules leading to various forms of excitation and to different reactions. These processes are important for application purposes.

The imaging study shows that in oxygen bubbles the needle continues to glow during the discharge before the formation of the streamer, during its glow, and after the streamer is extinguished. This again indicates two regions in the discharge, the streamer channel and the needle region. The Ar discharge study showed that these first stages may be dominated by high energy beam electrons, resulting in disproportionately high rates of excitation of higher energy states (See the discussion in Section 4.5). The electron energy during the later time of the discharge, when the emission comes mostly from the plasma channel, is too low for any significant excitation of the 11.05 eV molecular

electronic state of N_2. It appears, from the similarity of the nitrogen band behavior, that the change in discharge conditions with the change in the polarity of the needle also leads to the decrease in the concentration of fast electrons in the discharge.

This variation in electron energy is also confirmed by the changes in the intensity of the atomic oxygen lines 777 nm and 844 nm. The 844 nm line has been shown[1, 2] to be excited primarily by direct impact excitation of atomic oxygen

$$O + e \rightarrow O^* + e,$$

and dissociative excitation

$$O_2 + e \rightarrow O^* + O + e$$

is mostly responsible for the emission of the 777 nm line. The 844 nm line nm has higher excitation energy and therefore can be expected to be of lower intensity during later times in the discharge or in the discharge of positive polarity.

The discharge with the needle at a positive potential has very similar spectroscopic features to the later stages of the discharge with a negative needle. That is, the gas rotational and vibrational temperatures are somewhat higher, but the electron energy (as expressed in the changes in relative line intensities) is missing the fast beam electrons. This may be attributed to the effective removal of very fast electrons by the positive needle.

The following main observations can be made from the investigation of the discharge in air and oxygen bubbles:

- Individual electron avalanches form and get extinguished prior to the formation of a discharge channel.

- The discharge channel passes the current and deposits the charge on the wall of the bubble. The streamer takes a very short path to the water surface and continues to propagate along the wall. This propagation is self-terminating.
- Rotational and vibrational excitation temperatures have been determined to be 1100 - 1700 K and 8000 – 11000 K, respectively. The gas rotational and vibrational temperatures are in the same range and only slightly higher than in Ar (1000 – 1300 K for rotational and 8000 – 9000 K vibrational temperatures).
- The discharge with the needle at a negative potential appears to have very fast electrons in the needle region and the discharge with the needle at a positive potential does not. This is supported by spectroscopic evidence.
- The spectra are rich in molecular bands and atomic line features indicating a great variety of excitations and reactions, and the production of many interesting species.

References:

1. Yu. Raizer, Gas Discharge Physics, Springer-Verlag, New York, (1997)
2. A.Fridman, L. Kennedy, Plasma Physics and Engineering, Taylor & Francis, (2004)
3. M. Lieberman, A. Lichtenberg, Principles of Plasma Discharges and Materials Processing, John Wiley & Sons, Inc., New York, (1994)
4. K. H. Becker, U. Kogelschatz, K. H. Schoenbach, R. J. Barker, Non-Equilibrium Air Plasmas at Atmospheric Pressure, Institute of Physics Publishing, Philadelphia, 2005
5. Fridman, A. Chirokov, A. Gutsol, , J. Phys. D. Appl. Phys. 38 (2005) R1-R24

6. Summary

The focus of this work was on the determination of the characteristics of the discharge in a gas bubble in water and inferring the main processes that take place in this system. The study includes a detailed experimental investigations of the discharge in Ar bubbles and a brief look at the discharge in O_2 bubbles. A variety of methods: electrical, spectroscopic, and imaging are combined to put together a phenomenological picture of the discharge in a single bubble surrounding a needle in water. Given the complexity of the system under consideration each method separately is inadequate, but taken together, combined experimental evidence from all the different approaches illuminates many interesting features of this discharge process.

A 1 μs long voltage pulse is applied between the needle and disk electrodes submerged in water. A gas bubble a few millimeters in radius surrounds the tip of the needle. Electrical, optical, spectroscopic, and imaging measurements are taken during the time the voltage pulse is applied.

Imaging, electrical characteristics, and time-resolved optical emission data point to a fast streamer propagation mechanism and formation of a plasma channel in the bubble. The rich variety of processes taking place in a bubble during one voltage pulse is summarized in Figure 6.1. The diagram of all the processes is set against the background of typical voltage, current, and PMT oscillograms given here only for reference and orientation purposes.

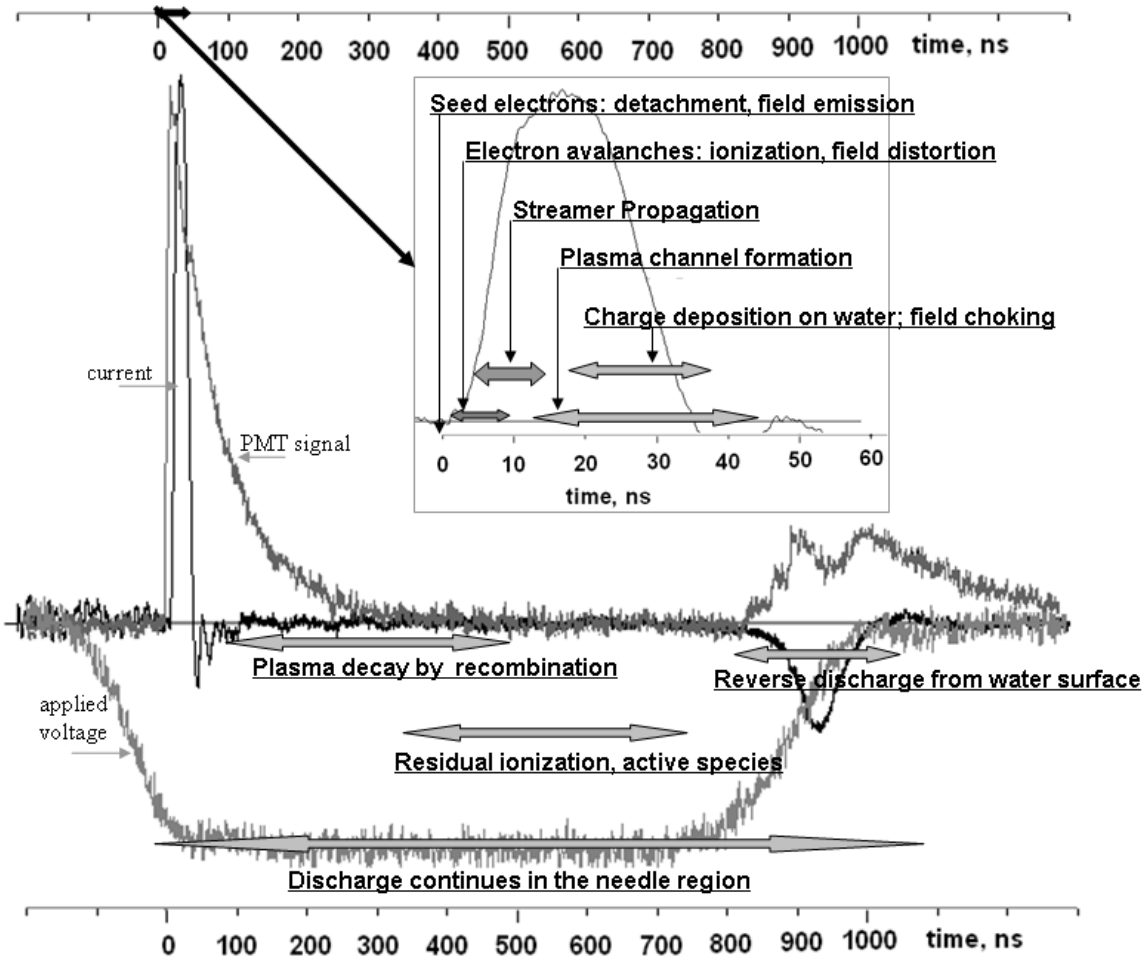

Figure 6.1 The descriptions of various discharge processes are given here against the backdrop of voltage, current, and PMT oscillograms to help set the time scale and for orientation purposes only.

1. Spectroscopic methods based on line intensity ratios and Boltzmann plots of line intensities of Ar and Ar^+, and examination of molecular emission bands from N_2 and OH, provide evidence of both fast beam-like electrons and slow thermalized electrons $T_e \sim 0.6 – 0.8$ eV.

2. Data from PMT measurements illuminate the collisional nature of the plasma (as expected at 1 atm) and the existence of the plasma in the bubble for several hundred nanoseconds longer than the current pulse.

3. Spectroscopic studies of rotational-vibrational bands of OH and N_2 give vibrational and rotational excitation temperature of the discharge of ~0.9 eV and 0.1 eV, respectively.

4. Imaging and electrical evidence show that the discharge charge is deposited on the bubble wall and water serves as a dielectric barrier for the field strength and time scales of this experiment. The charge is deposited on the water surface and spreads over an area a few times greater than the width of the discharge channel. The resulting electric field cancels out the applied field in the plasma channel and extinguishes the plasma in the channel. The data show a reverse discharge process when the applied voltage begins to drop.

5. Comparing the electrical and imaging information for consecutive pulses applied at a frequency of 1 Hz show that each discharge proceeds as an entirely new unique process. The discharges share the general characteristics described here. The bubble has no memory of the previous process except for an increase in water vapor content and some long-lived chemical species, such as O, O_3, O_2, H produced by the discharge process.

6. The differences between the discharges in Ar, air, and O_2 are due to the varying amounts of electronegative gas present in the bubble. Electrical and imaging evidence show that the discharge processes are slowed when the electronegative gas concentration increases. The discharge in oxygen tends to reach the wall via the shortest path and to proceed along the wall of the bubble.

7. The application of the same spectroscopic methods as in Ar bubbles reveals rotational and vibrational excitation temperatures have been determined to be 0.1 – 0.15

eV and 0.7 – 1.0 eV, respectively. These temperatures are in the same range and only slightly higher than in Ar.

8. The discharge conditions in this study fill a gap in well studied situations. The discharge distance of a few millimeters is longer than the short gaps(~10 – 100 μm with pd < 10 Torr·cm) and much shorter than the long gaps (meters long with pd > 1000 Torr·cm), resulting in an intermediate pd value of ~300 – 500 Torr·cm. The time and shape of the voltage pulse make it rather unique, longer than the short pulses 800 ns versus ~100 ns or less. The pulses are unidirectional as opposed to the conventional dielectric barrier discharges. The pulses are applied at 1 Hz repetition rate as opposed to the kilohertz range for dielectric barrier or plasma plume discharges. The voltage pulses are applied infrequently enough to allow the study of individual discharge processes. These conditions make the experimental evidence presented here valuable for the advancement of modeling and the theoretical understanding of the discharge in bubbles in water.

Appendices

Decay Rates calculations for optical emission from the discharge in Ar bubbles for band-pass filters with median frequencies of 750, 760, and 810 nm

Ar bubble, Filter, +/- 5 nm	Voltage, kV	Trial	Charge transferred by discharge, $x10^{-8}$ As	Decay after first peak, ns
750	8	A	4.645	63.32
750	8	B	4.128	60.58
750	8	C	4.04	64.68
750	**8**	**ave**	**4.271**	**62.86**
750	**8**	**32 ave**		**54.06**
750	10	A	5.541	46.82
750	10	B	5.2	56.55
750	10	C	4.464	38.47
750	10	D	4.27	46.04
750	10	E	4.301	42.54
750	10	F	4.386	47.33
750	**10**	**ave**	**4.69**	**46.29**
750	**10**	**32 ave**		**58.28**
750	12	A	6.041	58.637
750	12	B	6.368	47.169
750	12	C	6.59	55.339
750	12	D	6.61	53.705
750	12	E	6.228	39.997
750	**12**	**ave**	**6.37**	**50.97**
750	**12**	**32 ave**		**59.99**
750	14	A	8.61	72.2
750	14	B	6.769	77.52
750	14	C	7.11	56.36
750	14	D	7.716	64.11
750	14	E	6.951	70.06
750	**14**	**ave**	**7.43**	**68.05**
750	**14**	**32 ave**		**83.34**
750	16	A	7.995	70.65
750	16	B	7.74	98.49
750	16	C	7.049	72.54
750	**16**	**ave**	**7.59**	**80.56**
750	**16**	**ave**		**91.06**

Data table for the Boltzmann Plot for various voltages and times during discharge

Data table: ArII spectral lines and information for use in finding the excitation temperature																	
Wavelength, nm	322.1625	328.17	324.3688	319.423	322.5974	324.98	318.1038	321.2519	316.97	330.7	320.4321	329.36	335.0924	320.7586	320.5	325.9662	329.14
Energy Ek	23.072	23.08386	23.0839	23.10484	23.10484	23.12	23.121	23.121	23.17	23.5505	23.632	23.632	24.828	25.358	25.367	25.428	25.4425
Aik x108	0.0186	0.4684	1.177	0.07296	0.01797	0.7049	0.3773	0.05225	0.461	1.563	0.1414	0.7022	0.9449	0.00355	0.00802	0.01147	0.02383
gk	6	2	2	4	4	4	4	4	6	2	4	4	6	2	6	6	4
10 kV all 121006 50_3a - 2000	4000	3800	2400	6500	5100	2100	6300	6000	3300	3700	3400	3000	7100	6000	3400	3000	4200
10 kV all 50 121006 -2000	7200	4700	4000	9000	7700	4700	14000	10000	6500	7000	6900	5000	12000	12000	7000	4300	5400
13 kV all 50 121206 -1500	1500	1900	600	1600	1500	1000	1600	2100	800	1400	800	1300	4700	1500	1100	1300	1800
14 kV all 50 121006 -2000	5200	3000	3300	7100	5300	3100	7700	5200	5000	4500	2600	3200	8000	7300	3800	3300	5000
16 kV all 50 5a 121006 - 2000	11000	5000	6300	17000	12000	6000	20000	12000	8000	8000	7000	6100	10000	15000	8000	7500	6200
18 kV all 50 6a1 121006 - 2000	6600	4300	4900	7700	8000	4500	10000	8000	5000	6500	3300	4300	9000	7800	3800	5100	4300
10 kV first 50c1 121006 - 2000	900	1300	1300	800	1100	900	4400	1100	880	850	1100	400	4400	600	700	1000	1400
10 kV first 50a1 121006 - 1500	1700	2000	2000	2000	2400	2100	2100	2800	2500	1900	1500	1500	5900	2000	2000	2400	2600
10 kV first 50a1 121006 - 2000	1200	1500	1600	1400	1900	1600	1600	2300	2000	1600	1400	1500	5400	1500	1500	1900	2200
14 kV first 50 4a 121006 - 1500	1400	2000	1700	1500	1500	1500	1600	1700	1700	1300	1300	1000	3600	2000	1400	1800	2000
16 kV first 50 5c1 121006 - 2000	1400	2100	1200	1700	1700	1500	1800	1900	1500	1500	1500	1400	4800	1600	1600	2000	2000
18 kV first 50 5c1 121006 - 1500	1200	1400	1000	1300	1500	1000	1100	1800	1300	1300	800	1200	3600	1300	1000	1500	2000

Bibliography

M. Sato, T. Ohgiyama, and .S. Clements, (1996) *IEEE Trans. Ind. Appl*. **32**(1), pp. 106.
B. Sun, M. Sato, J.S. Clements, (1997) J. Electrostatics, **39** (3), pp. 189.
S. Ihara, M. Miichi, S. Satoh, and C. Yamabe, (1999) IEEE Intl Pulsed Power Conf. 5451, pp. 1291.
H. Akiyama, (2000) IEEE Trans. Diel. Electr. Insul., **7**, pp. 646.
A. M. Anpilov, E. M. Barkhudarov, Yu. B. Bark, (2001) *J. Phys. D: Appl. Phys.*, **34**, pp. 993–999
A. Abou-Ghazala, S. Katsuki, K. H. Schoenbach, F.C. Dobbs, and K.R. Moreira, (2002) *IEEE Trans. Plasma Sci.,* **30**, pp. 1449.
P. Lukes, A.T. Appleton, B. Locke, (2004) *IEEE Trans. Ind. Appl.*, **40** (1), pp. 60-67
P. Lukes, B. Locke, (2005) *Ind. Eng. Chem. Res.*, **44**, pp. 2921-2930
P. Sunka, V. Babicky, M. Clupek, P. Lukes, M. Simek, J. Schmidt, M. Cernak, (1999) *Plasma Sources Sci.Technol.*, **8**, pp. 258-265
Y. Wen, H. Liu, W. Liu, X. Jiang, (2005), *Plasma Chem, Process.*, **5**, pp. 137–146
B. Sun, M. Sato, J. Clemens, (1999) *J. Phys. D: Appl. Phys*., **32**, pp. 1908–1915T.
M. Kurahashi, S. Katsura, A. Mizuno, (1997), *Journal of Electrostatics*, **42**, No. 1, pp. 93-105
T. Miichi, S. Ihara, S. Satoh, C. Yamabe, (2000) *Vacuum*, **59**, pp. 236-243
T. Miichi, N. Hayashi, S. Ihara, S. Satoh and C. Yamabe, *Ozone : science & engineering*, (2002), **24**, No. 6, pp. 471-477
C. Yamabe, F. Takeshita, T. Miichi, N. Hayashi, S. Ihara, (2005) *Plasma, Process. Polym,* **2**, pp. 246-251
A. Anpilov *et al* (2001) *J. Phys. D: Appl. Phys.* **34** 993-999
A.M. Anpilov , E.M. Barkhudarov , N. Christofi , V.A. Kop'ev , I.A. Kossyi , M.I. Taktakishvili and Y. Zadiraka, *Letters in Applied Microbiology*, **35,** Issue 1, (2002), pp. 90 – 94
Akishev, Y.; Grushin, M.; Karalnik, V.; Monich, A.; Petryakov, A.; Trushkin, N., (2008), Plasma Science, IEEE Transactions on, **36**, Issue 4, pp. 1142 – 1143
Mozgina, O.; Gershman, S.; Belkind, A.; Becker, K.; Christodoulatos, C. Plasma Science, 2006. ICOPS 2006. IEEE Conference Record - Abstracts. The 33rd IEEE International Conference on, (2006), pp. 217 – 217
O. Mozgina,, Pulsed Electrical Discharges in Bubbled Water for Environmental Applications, Ph.D. Thesis (2008) Stevens Institute of Technology.
S. Gershman, O. Mozgina, A. Belkind, K. Becker, E. Kunhardt, Contributions to Plasma Physics, **47**, Issue 1-2 , (2007), pp.19 - 25
Y. Kim, M. Junga, S. Oh, J. Han, (2005), Thin Solid Films, 475, 91– 96
Th. Welzel, Th. Dunger, St. Welzel, H. Kupfer, F. Richter, (2005), Surface & Coatings Technology, pp. 1-4
K. Kozlov, H-E Wagner, R. Brandenburg, P. Michel, J. (2001), Phys. D: Appl. Phys., **34**, 3164-3176
K. Kozlov, R. Brandenburg, H-E Wagner, A. Morozov, P. Michel, J. (2005), Phys. D: Appl. Phys., **38**, 518-529

N. Jidenko, M. Petit, J. P. Borra, (2006), **J. Phys. D: Appl. Phys.** Vol. 39, pp. 281–293
R. Hippler, S. Pfau, M. Schmidt, K. H. Schoenbach, (2001), *Low Temperature Plasma Physics*, Wiley_VCH, Berlin
H. Raether, (1964), *Electron Avalanche and Breakdown in Gases* (London: Butterworths)
Ralchenko, Yu., Kramida, A.E., Reader, J., and NIST ASD Team (2008). *NIST Atomic Spectra Database* (version 3.1.5), [Online]. Available: http://physics.nist.gov/asd3 [2008, August 15]. National Institute of Standards and Technology, Gaithersburg, MD.
J. R. Gillis, A. Goldman, G. Stark, C. P. Rinsland *Journal of Quantitative Spectroscopy and Radiative Transfer*, **68, Issue 2**, (2001), Pages **225**-230
G. Herzberg, Molecular Spectra and Molecular Structure, Vol. 1 (Spectra of Diatomic Molecules), Van Nostrand-Reinhold, New York, (1950).
R. Pearse, A. Gaydon, The Identification of Molecular Spectra, Chapman and Hall Ltd., London, (1976)
H. R. Griem, Principles of Plasma Spectroscopy, Cambridge University Press, (1997)
V. M. Donnelly, J. Phys. D : Appl. Phys. **37**,(2004)
A. Bogaerts, R. Gijbeis, J. Vicek, J. Appl. Phys., Vol. 84, No. 1, 121-136, (1998)
F J Gordillo-V´azquez, M Camero, C. G´omez-Aleixandre, Plasma Sources Sci. Technol. **15** (2006) 42–51
M. Cornett, M. George, B. Fries, H. Walde, L. Casson, Society of Vacuum Coaters, 45th Annual Technical Conference Proceedings (2002)
M. V. Malysheva, V. M. Donnelly, J. Vac. Sci. Technol. A **15**, No.3, (1997), 550 - 558
M. Hayashi, "Bibliography of Electron and Photon Cross Sections with Atoms and Molecules Published in the 20th Century - Argon", National Institute For Fusion Science, Report No. NIFS-DATA-72, Jan. 2003.
G. Raju, IEEE Transactions on Dielectrics and Electrical Insulation Vol. **11**, No. 4, 649-674 (2004)
N. Sadeghia, D. W. Setser, A. Francis, U. Czarnetzki, and H. F. Do¨bele, J. Chem., Phys., Vol. **115**, No. 7 (2001) 3144-3154
M. Brown, B.Ganguly, A. Garscadden, Plasma Sources Sci. Technol. **11** (2002) 190–194
R. Hippler, H. Kersten, M. Schmidt, K.H. Schoenbach, Eds., Low Temperature Plasmas, Fundamentals, Technologies, Techniques, Vol. 1 und Vol. 2, Wiley-VCH: Berlin (2008)
Z. Jelenak, Z. Velikic, J. Bozin, Z. Petrovic, and B. Jelenkovic, Phys. Rev. E, **47**, No. 5, (1993), 3566-3573
A. Lafthus, P. Krupenie, J. Phys. Chem. Ref Data, Vol. **6**, No. 1. (1977).
N. Masoud, K. Martus, M. Figus, K. Becker, Contrib. Plasma Phys. **45**, No 1, 32-39 (2005)
S. Pellerin, J. M. Cormier, F. Richard, K. Musiol, J. Chapelle, J. Phys. D. Appl. Phys.**29,** (1996),726-739
C.O. Laux, T. G. Spence, C.H. Kruger, R.N. Zare, Plasma Sources Sci. Technol.**12** (2003) 125-138
S. A. Moshkalyov, P. G. Steen, S. Gomez, W. G. Graham, Appl. Phys. Lett. Vol. **75**, No.3 (1999) 328-330
Yu. Raizer, Gas Discharge Physics, Springer-Verlag, New York, (1997)
A.Fridman, L. Kennedy, Plasma Physics and Engineering, Taylor & Francis, (2004)
B. Eliasson, M. Hirth, U. Kogelschatz, J. Phys. D. Appl. Phys. 20(1987) 1421-1437

A. Bogaerts, R. Gijbeis, J. Vicek, J. Appl. Phys. Vol. 84, No. 1 (1998) 121-136
K. Kano, M. Suzuki, H. Akatsuka, Plasma Sources Sci. Technol. 9 (2000) 314-322
A. Fridman, A. Chirokov, A. Gutsol, , J. Phys. D. Appl. Phys. 38 (2005
S. Ihara, M. Miichi, S. Satoh, and C. Yamabe, IEEE Intl Pulsed Power Conf.5451, (1999) 1291.
P. Lukes, A.T. Appleton, B. Locke, IEEE Trans. Ind. Appl., **40** (2004) 60-67
P. Lukes, B. Locke, Ind. Eng. Chem. Res., **44** (2005) 2921-2930
C. Yamabe, F. Takeshita, T. Miichi, N. Hayashi, S. Ihara, Plasma, Process. Polym**, 2** (2005) 246-251
R. Zhang, L.M. Wang, C. Zhang, Y. Nie, Y. Wu, Z. Guan, IEEE TRANSACTIONS ON PLASMA SCIENCE, VOL. 34, NO. 3, JUNE 2006
V. I. Grinevich, Theoretical Foundations of Chemical Engineering, Vol. 38, No. 1, 2004, pp. 56–60.
S. Gershman, O. Mozgina, A. Belkind, K. Becker, and E. Kunhardt, Contrib. Plasma Phys. **46**, No. 1-2, 1 . 7 (2007)
Yu. Raizer, Gas Discharge Physics, Springer-Verlag, New York, (1997)
R. E. Walkup, K. L. Saenger, G. S. Selwyn, J. Chem. Phys., **84** (1986) 2668-74
N. Krstulovic, I. Labazan, S. Milosevic, U. Cvelbar, A. Vesel, and M. Mozetic, J. Phys.D: Appl. Phys. **39** (2006) 3799-3804
G. Herzberg, Molecular Spectra and Molecular Structure, Vol. 1 (Spectra of Diatomic Molecules), Van Nostrand-Reinhold, New York, (1950).
S. Pellerin, J. M. Cormier, F. Richard, K. Musiol, J. Chapelle, J. Phys. D. Appl. Phys.29, (1996),726-739
A.Fridman, L. Kennedy, Plasma Physics and Engineering, Taylor & Francis, (2004)
M. Lieberman, A. Lichtenberg, Principles of Plasma Discharges and Materials Processing, John Wiley & Sons, Inc., New York, (1994)

Curriculum Vita

Dates:	Education:
1/1998-present	**Candidate for PhD** in Physics Rutgers University, NJ
1975-1980	**MS** in Physics and Teaching, Latvian State University, Riga, Latvia.
	Professional Experience:
9/1997- present	**Teacher of Science** Watchung Hills Regional High School, Warren, NJ
9/2003-10/2008	**Research Associate** Physics Department, Stevens Institute of Technology, Hoboken, NJ.
7/2000-2005	**Master Teacher** Princeton Plasma Physics Laboratory, Princeton, NJ
1/1989-9/2002	**Adjunct Instructor** Department of Physics and Astronomy, Rutgers University, NJ
9/1996-6/1997	**Teacher of Science** South Plainfield High School, South Plainfield, NJ
8/1992-8/1996	**Teacher of Science** Hightstown High School, Hightstown, NJ
7/1989-5/1993	**Adjunct Instructor** Middlesex County College, Edison, NJ
7/1990-6/1992	**Teacher of Science** Solomon Schechter Day School, West Orange, NJ
9/1988-6/1989	**Adjunct Instructor** Department of Mathematics, Jersey City College, Jersey City, NJ.
7/1985-7/1986	**Research Assistant** Department of Physics and Astronomy Rutgers University, NJ
9/1982-6/1985	**Assistant Professor** Department of Physics, Earlham College, Richmond, Indiana
1/1982-12/1982	**Assistant Director** of Science Laboratories Indiana University, Richmond, Indiana
9/1977-2/1981	**Research Assistant** Institute of Solid State Physics, Latvian State University, Riga, Latvia
Publications:	S. Gershman, O. Mozgina, A. Belkind, K. Becker, and E. Kunhardt, Contrib. Plasma Phys. **46**, No. 1-2, 1 . 7 (2007) A. Belkind, S. Gershman, O. Mozgina, C. Christodoulatos, K. Becker, 28th ICPIG, July 15-20, 2007, Prague, Czech Republic K. Karpi´nska, A. Malinowski, M. Z. Cieplak, S. Guha, S. Gershman, G. Kotliar, T. Sko´skiewicz, W. Plesiewicz, M. Berkowski, and P. Lindenfeld, Phys. Rev. Lett. **77**, 3033 (1996) IR Spectra of Irradiated Sulfate-Ion in the Alkali Halide Matrix, Publication of the Latvian Academy of Sciences, 12 (1980)